

Programmable Multistable Mechanisms: Design, modeling, characterization and applications

THÈSE N° 9055 (2018)

PRÉSENTÉE LE 14 DÉCEMBRE 2018

À LA FACULTÉ DES SCIENCES ET TECHNIQUES DE L'INGÉNIEUR
CHAIRE PATEK PHILIPPE EN CONCEPTION MICROMÉCANIQUE ET HORLOGÈRE
PROGRAMME DOCTORAL EN MICROSYSTÈMES ET MICROÉLECTRONIQUE

ÉCOLE POLYTECHNIQUE FÉDÉRALE DE LAUSANNE

POUR L'OBTENTION DU GRADE DE DOCTEUR ÈS SCIENCES

PAR

Mohamed Gamal Abdelrahman Ahmed ZANATY

acceptée sur proposition du jury:

Prof. L. G. Villanueva Torrijo, président du jury
Prof. S. N. Henein, Dr I. Vardi, directeurs de thèse
Dr I. Kjelberg, rapporteur
Prof. L. Rubbert, rapporteur
Prof. P. Reis, rapporteur



ÉCOLE POLYTECHNIQUE
FÉDÉRALE DE LAUSANNE

Suisse
2018

In the memory of my father . . .

Abstract

Multistable Mechanisms are mechanical devices having more than one stable state. Since these mechanisms can maintain different deformations with zero force, they are advantageous for low power environments such as wristwatches and medical devices.

In this thesis, I introduce *programmable multistable mechanisms (PMMs)*, a new family of multistable mechanisms where the number, position, and stiffness of stable states can be controlled by programming inputs modifying the boundary conditions. PMMs can be synthesized by combining bistable mechanisms. This method was used to produce the *T-mechanism*, a PMM consisting of two double parallelogram mechanisms (DPMs) connected orthogonally where each DPM consists of two parallel beams connected centrally by a rigid block and axially loaded by programming input.

An analytical model based on Euler-Bernoulli beam theory was derived to describe qualitatively the stability behavior of the T-mechanism. The model approximates the mechanism's stiffness by a sixth order polynomial from which the reaction force and strain energy expressions can be estimated. These explicit formulas provide analytical expressions for the number, position, and stiffness of stable and unstable states as functions of the programming inputs. The qualitative stability behavior was represented by the *programming diagram*, *bifurcation diagrams* and *stiffness maps* relating the number, position and stiffness of stable states with the programming inputs. In addition, I showed that PMMs have zero stiffness regions functioning as constant-force multistable mechanisms. Numerical simulations validated these results.

Experimental measurements were conducted on the T-mechanism prototype manufactured using electro-discharge machining. An experimental setup was built to measure the reaction force of the mechanism for different programming inputs. I verified the possible configurations of the T-mechanism including monostability bistability, tristability, quadrastability, constant force monostability, constant force bistability, zero force monostability, zero force bistability, and zero force tristability, validating my analytical and numerical models.

Compared to classical multistable mechanisms which are displaced between their stable states by imposing a direct displacement, PMMs can be displaced by modifying mechanism strain energy. This property increases the repeatability of the mechanism as the released energy is independent of the driving parameters, which can be advantageous for mechanical watches and medical devices.

Accurate timekeepers require oscillators having repeatable period independent of their energy source. However, the balance wheel spiral spring oscillator used in all mechanical watches,

suffers from *isochronism defect*, i.e., its oscillation period depends on its amplitude. I addressed this problem by introducing novel detached constant force escapements for mechanical wristwatches based on PMMs.

In the medical domain, I applied PMMs to construct a retinal vein cannulation needle for the treatment of *retinal vein occlusion (RVO)*, an eye condition in which retinal veins are blocked reducing the amount of oxygen delivered to the retina thereby causing vision loss. One treatment for RVO is drug injection into the retinal vein. However, this is difficult as the vein is fragile with a diameter below 100. Moreover, the puncturing force is not perceptible by surgeons. I used PMMs to construct needles producing sufficient repeatable puncturing energy with a predefined stroke independent of the operator input. Numerical simulations were used to model and dimension our proposed tool and satisfy the strict requirements of ophthalmologic operations. In a joint work, the tool was manufactured using 3D femto-laser printing of glass. An experimental setup was built to characterize the tool's mechanical behavior and to verify my computations. The tool was successfully applied to cannulate retinal veins of pig eyes.

Keywords: Multistable Mechanisms – Compliant Mechanisms – Stability programming – Nonlinear Stiffness – Horological Escapements – Retinal Vein Cannulation – Surgical Devices.

Résumé

Les mécanismes multistable sont des mécanismes ayant plus d'un état stable. Puisque ces mécanismes peuvent maintenir plusieurs déformations avec force zéro, ils sont avantageux pour des environnements de basse puissance comme l'horlogerie et les outils médicaux.

Dans cette thèse, j'introduis des mécanismes multistables programmables (PMMs), une nouvelle famille de mécanismes multistables où le nombre, la position et la rigidité des états stables peuvent être contrôlés par des paramètres de programmations qui modifient les conditions aux limites. Les PMMs peuvent être synthétisés en combinant des mécanismes bistables. Cette méthode a été utilisée pour produire le mécanisme en T, un PMM consistant de deux parallélogrammes doubles (DPM) liés de manière orthogonale, où chaque DPM est composé de deux poutres parallèles connectées à leur centre par un bloc rigide et armées de manière axiale par un paramètre de programmation.

Un modèle analytique basé sur la théorie des poutres d'Euler-Bernoulli a été développée pour décrire le comportement qualitatif du mécanisme en T. Ce modèle donne une approximation de la rigidité du mécanisme en terme d'un polynôme de degré six, dont la force de réaction et l'énergie de déformation peuvent être estimées. Ces formules explicites donnent des formules analytiques pour le nombre, la position et la rigidité des états stables et instables en terme des paramètres de programmation. Le comportement qualitatif de la stabilité a été représenté par le diagramme de programmation, les diagrammes de bifurcation et les cartes de rigidité décrivant le nombre, la position et la rigidité des états stables en termes des paramètres de programmation. Des simulations numériques ont validé ces résultats.

Des mesures expérimentales ont été faites sur un prototype du mécanisme en T construit en utilisant l'électro-érosion. Un banc expérimental a été construit pour mesurer la force de réaction pour différentes valeurs des paramètres de programmation. J'ai vérifié les configurations possible du mécanisme en T, y compris la monostabilité, bistabilité, tristabilité et quadrastabilité, la monostabilité à force constante, la bistabilité à force constante, la monostabilité à force zéro, la bistabilité à force zéro et la tristabilité à force zéro, ce qui a validé les modèles analytiques et numériques.

Comparé aux mécanismes multistables classiques qui se déplacent entre leur états stables en imposant un déplacement direct, les PMMs sont déplacés en modifiant leur énergie de déformation. Cette propriété augmente la répétabilité puisque l'énergie libérée est indépendante des paramètres d'entrée, ce qui peut être avantageux pour les montres mécaniques et les outils médicaux.

Les gardes-temps précis nécessitent des oscillateurs ayant une période répétable indépendante de leur source d'énergie. En revanche, le balancier-spiral, l'oscillateur utilisé dans toutes les montres mécaniques, a un défaut d'isochronisme, c'est-à-dire, sa période varie en fonction de son amplitude. J'ai confronté ce problème en inventant des nouveaux échappements détachés à force constante pour montres-bracelet et basé sur des PMMs.

Dans le domaine médical, j'ai appliqué les PMMs pour construire une aiguille de canulation pour veines rétiniennes, une technique pour traiter l'occlusion de veines rétiniennes (RVO), une maladie où les veines rétiniennes sont bloquées causant une perte de vue. Le traitement consiste d'une injection de médicament directement dans la veine. Ceci est très difficile puisque la veine est fragile et son diamètre est inférieur à 100. De plus, la force de ponction n'est pas perceptible par les chirurgiens. J'ai utilisé des PMMs pour construire des aiguilles capables de produire suffisamment d'énergie de ponction, répétable et avec une course prédéfinie indépendante de la force appliquée par le chirurgien. Des simulations numériques ont été utilisées pour modéliser et dimensionner notre outil et de satisfaire les conditions très strictes de la chirurgie ophtalmologique. L'outil a été fabriqué par une équipe en utilisant la technique d'impression 3D par femto-laser. Un banc expérimental a été construit pour caractériser le comportement mécanique et pour valider mes calculs. L'outil a été appliqué avec succès à la canulation de veines rétiniennes de cochons.

Mots-clés : Mécanismes multistables – guidages flexibles – programmation de stabilité – rigidité non-linéaire – échappements horlogers – canulation de veines rétiniennes – outils médicaux.



Acknowledgments

I would like to thank my supervisors Simon Henein and Ilan Vardi. I am very grateful for their time, effort, guidance and support. I appreciate all the help provided by my EPFL colleagues and industrial partners as well as my family and friends.

A part of the research described in this thesis was funded by the Swiss commission of science and technology (CTI), re-branded as Innosuisse.

Neuchâtel, 10 November 2018

M. Z.

Contents

Abstract (English/Français)	i
Acknowledgments	v
List of figures	xi
List of tables	xvii
1 Goals and Plan of the Thesis	1
1.1 Introduction and thesis motivation	1
1.2 Thesis objectives	1
1.3 Thesis structure	2
2 State of the Art	5
2.1 Stability	5
2.1.1 The theory of stability	5
2.1.2 Stability of compliant mechanisms	7
2.2 Multistable mechanisms	7
2.2.1 Examples of bistable mechanisms	7
2.3 Selected applications	11
3 Stability Programming	13
3.1 Introduction	13
3.2 Programmable multistable mechanisms (PMMs)	14
3.2.1 Conventional multistable mechanisms	14
3.2.2 Definitions	14
3.2.3 Multistability programming	15
3.3 Synthesis	16
3.3.1 General method	16
3.3.2 Basic example	17
3.3.3 T-connection versus serial and parallel connections	18
3.4 T-mechanism	18
3.4.1 Operation of the mechanism	19
3.4.2 Dimensions of the mechanism	21
3.5 Analytical model	24
	vii

Contents

3.5.1	Zero load stiffness and zero stiffness load	25
3.5.2	Axial shortening	25
3.5.3	Axial loads	26
3.5.4	Secant stiffness	27
3.5.5	Reaction force	27
3.5.6	Strain energy	28
3.5.7	Normalization	28
3.5.8	Reduction to cubic polynomial	29
3.5.9	Roots of a cubic polynomial	30
3.5.10	Evaluation of DOS	30
3.6	Qualitative stability behavior	31
3.6.1	Computation of DOS of the T-mechanism	31
3.6.2	Equilibrium and zero stiffness diagrams	36
3.6.3	Stiffness diagrams	39
3.6.4	Special cases	41
3.6.5	DOS sensitivity	44
3.7	Numerical validation	44
3.8	Applications	46
3.9	Conclusion	46
4	Experimental Characterization	47
4.1	Introduction	47
4.2	Programmable multistable T-mechanism	47
4.3	Analytical model	50
4.4	Numerical simulations	54
4.5	Fabrication	55
4.6	Experimental setup	55
4.7	Results and discussion	56
4.7.1	Monostable region	56
4.7.2	Bistable region	56
4.7.3	Tristable region	58
4.7.4	Quadrastable region	58
4.7.5	Summary	61
4.7.6	Programming diagram	62
4.7.7	Equilibrium positions	64
4.7.8	Zero stiffness positions	68
4.8	Conclusion	70
5	Application I: Detached Snap Escapement	71
5.1	Introduction	71
5.2	State of the art	73
5.2.1	Constant force escapements	73
5.2.2	Swiss lever escapement	77

5.3	Description of the invention	78
5.3.1	Snap escapement	78
5.3.2	Snap mechanism	79
5.3.3	Master and slave anchors	81
5.3.4	Operation of the snap escapement	82
5.3.5	Security	90
5.3.6	Self-starting	90
5.4	Demonstrator	91
5.5	Conclusion	94
6	Application II: Retinal Vein Cannulation	95
6.1	Introduction	95
6.1.1	Retinal vein cannulation (RVC)	96
6.1.2	Challenges of RVC	97
6.2	Safe puncture optimized tool for RVC	99
6.2.1	Utilization protocol	99
6.2.2	Theoretical design	100
6.2.3	Tool design	104
6.3	Dimensioning	106
6.4	Fabrication	107
6.5	Characterization	109
6.5.1	Experimental measurements	109
6.5.2	Results and discussion	110
6.5.3	Pig eye testing	113
6.6	Conclusion and perspectives	113
7	Contributions and Perspectives	115
7.1	Contributions	115
7.2	Perspectives	115
	Bibliography	126
	Curriculum Vitae	127

List of Figures

2.1	(a) Pendulum, (b) inverted pendulum.	5
2.2	Time response of the pendulum and phase diagram when its initial position is at (a,b) $\alpha = 0$, (c,d) $\alpha = \pi$	6
2.3	Hair clips and bottle lids as examples of bistable mechanisms	7
2.4	Strain energy, reaction force and tangential stiffness of a bistable mechanism where s_1, s_2 are stable positions, u is unstable position and ζ_1, ζ_2 correspond to zero stiffness positions.	8
2.5	Axially loaded bistable beam, (a) no axial load, (b) stable state of the beam, (c) unstable state of the beam, (d) second stable state of the beam.	9
2.6	Curved bistable beam mechanisms (a) cosine-shaped beam, (b) V-shaped beam.	9
2.7	A slider crank bistable mechanisms, (a) first stable state, (b) unstable state, (c) second stable state.	10
3.1	Block diagram representation of a 3-DOP PMM programmed to be (a) monostable, (b) bistable.	16
3.2	Synthesis of PMMs.	17
3.3	Block diagram representation of (a) PBM, (b) 2-DOP T-combination.	17
3.4	Double parallelogram mechanism and its strain energy when programmed to be (a) monostable, (b) bistable.	18
3.5	(a) DPM connection blocks, (b) 2-DOP T-combination of DPMs.	18
3.6	Stable states of the 2-DOP T-mechanism programmed to be (a) monostable, (b) bistable, (c) tristable, (d) quadrastable.	19
3.7	Block diagram representation, example mechanism and DOS diagram of (a) T-connection, (b) serial connection, (c) parallel connection.	20
3.8	(a) Constructed T-mechanism, (b) top view, (c) main components.	22
3.9	Range of DOS for admissible η_1, η_2 for (a) $\alpha_2 = 0.5$, (b) $\alpha_2 = 1$, (c) $\alpha_2 = 1.5$	23
3.10	Strain energy of the T-mechanism programmed to be (a) monostable at $\hat{p}_1 = 0, \hat{p}_2 = 0$, (b) bistable at $\hat{p}_1 = 0, \hat{p}_2 = 0.12$, (c) tristable at $\hat{p}_1 = 0.0175, \hat{p}_2 = 0$, (d) quadrastable at $\hat{p}_1 = 0.12, \hat{p}_2 = 0.0175$	32
3.11	(a) Sign of the discriminant Δ_Φ , (b) number of sign alternations n_σ , (c) DOS.	33
3.12	Sign of (a) β_0 , (b) β_1 , (c) β_2 , (d) β_3	34
3.13	(a) Sign and zeros of β_0 , (b) DOS with boundaries.	35

3.14	Equilibrium and zero stiffness diagrams for the fixed values shown in (a): (b) $\hat{p}_1 = 0.0$, (c) $\hat{p}_1 = 0.007$, (d) $\hat{p}_1 = 0.012$, (e) $\hat{p}_1 = 0.016$, (f) $\hat{p}_1 = 0.02$	36
3.15	Equilibrium and zero stiffness diagrams for the fixed values shown in (a): (b) $\hat{p}_2 = -0.06$, (c) $\hat{p}_2 = -0.03$, (d) $\hat{p}_2 = 0.025$, (e) $\hat{p}_2 = 0.06$, (f) $\hat{p}_2 = 0.12$	38
3.16	Stiffness and sign of stiffness at equilibrium positions: (a) and (b) for q_0 , (c) and (d) for q_1 , (e) and (f) for q_2 , (g) and (h) for q_3	40
3.17	(a) Selected values of \hat{p}_1, \hat{p}_2 leading to near zero force and near constant force regions: (b) zero force monostable mechanism at $\hat{p}_1 = 0, \hat{p}_2 = 0.052$, (c) constant force monostable mechanism at $\hat{p}_1 = 0.012, \hat{p}_2 = 0$, (d) zero force bistable mechanism at $\hat{p}_1 = 0.017, \hat{p}_2 = -0.045$, (e) constant force bistable mechanism at $\hat{p}_1 = 0.007, \hat{p}_2 = 0.092$, (f) zero force tristable mechanism at $\hat{p}_1 = 0.017, \hat{p}_2 = 0.12$	43
3.18	FEM rendering of T-mechanism deformation.	44
3.19	(a) Values of \hat{p}_1, \hat{p}_2 for FEM simulation with T-mechanism programmed to be (b) monostable at $\hat{p}_1 = 0, \hat{p}_2 = 0$, (c) bistable at $\hat{p}_1 = 0, \hat{p}_2 = 0.12$, (d) tristable at $\hat{p}_1 = 0.0175, \hat{p}_2 = 0$, (e) quadrastable at $\hat{p}_1 = 0.0175, \hat{p}_2 = 0.012$, (f) percent difference between analytical and numerical models.	45
4.1	2-DOP T-combined double parallelogram mechanisms composed of (a) distributed stiffness blades, (b) lumped stiffness rectangular hinges.	48
4.2	(a) T-shaped mechanism, (b) key dimensions, (c) forces and displacements.	49
4.3	Equivalent rigid body diagram of the T-mechanism.	50
4.4	(a) T-shaped mechanism monolithically manufactured by EDM, (b) schematic representation of the measurement setup, (c) realization of the measurement setup.	53
4.5	Stable state q_0 of the mechanism programmed in monostable region based on FEM (left) and experiment (right).	56
4.6	The reaction force of the mechanism when programmed as monostable for $p_1 = 0.0[mm]$ and $p_2 = 0.0[mm]$	57
4.7	Stable states, q_1^\pm and unstable state, q_0 of the mechanism programmed in bistable region I based on FEM (top) and experiment (bottom).	57
4.8	The reaction force of the mechanism programmed as bistable in region I for $p_1 = -0.15[mm]$, $p_2 = 1.1[mm]$	58
4.9	Stable states, q_3^\pm and unstable state, q_0 of the mechanism programmed in bistable region II based on FEM (top) and experiment (bottom).	59
4.10	The reaction force of the mechanism programmed as bistable in region II for $p_1 = 0.39[mm]$, $p_2 = -0.9[mm]$	59
4.11	Stable states, q_0, q_3^\pm and unstable states, q_2^\pm of the mechanism programmed in tristable region based on FEM (top) and experiment (bottom).	60
4.12	The reaction force of the mechanism programmed as tristable for $p_1 = 0.37[mm]$, $p_2 = 0.0[mm]$	60
4.13	Stable states, q_1^\pm, q_3^\pm , and unstable states, q_0, q_2^\pm of the mechanism programmed in quadrastable region based on FEM (top) and experiment (bottom).	61

4.14	The reaction force of the mechanism programmed as quadrastable for $p_1 = 0.36[mm]$, $p_2 = 2.8[mm]$. The inset illustrates the reaction force upon switching between second and third stable states.	62
4.15	Programming diagram of the T-mechanism in which stability boundaries p_1^{cr} , p_2^a , p_2^b , p_2^c are experimentally verified.	63
4.16	(a) Selected p_1 values of the calculated equilibrium position diagrams as p_2 varies from $-4[mm]$ to $4[mm]$. Equilibrium positions diagram at (b) $p_1 = -0.1[mm]$, (c) $p_1 = 0.35[mm]$ verified both numerically and experimentally.	64
4.17	(a) Selected p_2 values of the calculated equilibrium position diagrams as p_1 varies from $-0.2[mm]$ to $0.5[mm]$. Equilibrium positions diagram at (b) $p_2 = -1[mm]$, (c) $p_2 = 0[mm]$, (d) $p_2 = 1[mm]$, (e) $p_2 = 3[mm]$ verified numerically and experimentally.	67
4.18	(a) Sign of the discriminant of the force polynomial, (b) number of sign changes of the coefficient, (c) number of stable states, (d) sign of the discriminant of the stiffness polynomial, (e) number of zero stiffness states.	68
4.19	Reaction force of the T-mechanism based on analytical, numerical and experimental measurements for (a) ZFMM at $p_1 = 0.09[mm]$, $p_2 = 1.6[mm]$, (b) CFMM at $p_1 = 0.24[mm]$, $p_2 = 0.0[mm]$, (c) ZFBM at $p_1 = 0.39[mm]$, $p_2 = -0.7[mm]$, (d) CFBM at $p_1 = 0.14[mm]$, $p_2 = 2[mm]$, (e) ZFTM at $p_1 = 0.35[mm]$, $p_2 = 2.65[mm]$, (f) selected points highlighted along the zero stiffness boundaries.	69
5.1	Components of mechanical watch.	72
5.2	Main spring fully wound (left) and fully unwound (right).	73
5.3	Variation of the torque of the barrel spring with respect to the winding angle.	73
5.4	Comparison of the impulse action between variable force escapements and constant force escapements.	74
5.5	Comparison between the unlocking actions of attached escapements and detached escapements.	75
5.6	Girard - Perregaux constant force escapement.	76
5.7	Ulysse Nardin constant force escapement.	76
5.8	Bottom view of the Swiss lever escapement.	77
5.9	Snap escapement.	78
5.10	Snap mechanism and its strain energy when programmed as (a) symmetric bistable, (b) asymmetric bistable, (c) zero force monostable, (d) monostable. The ball represents the position of the lever.	80
5.11	Equivalent snap mechanism integrated within our presented escapement.	80
5.12	Snap mechanism as it switches between its stable states.	81
5.13	Master(2) and slave(4) anchors of the snap escapement.	82
5.14	Step 1	82
5.15	Step 2.	83
5.16	Step 3.	83
5.17	Step 4.	84

List of Figures

5.18 Step 5.	85
5.19 Step 6.	85
5.20 Step 7.	86
5.21 Step 8.	86
5.22 Step 9.	87
5.23 Step 10.	87
5.24 Step 11.	88
5.25 Step 12.	89
5.26 Step 13.	89
5.27 Step 14.	90
5.28 A demonstrator of the snap escapement.	91
5.29 Snap bistable mechanism - two stable states, red lever for programming and blue lever is the output.	91
5.30 Top view of snap escapement - high speed camera	92
5.31 Unlocking of the master anchor	92
5.32 Impulse of the oscillator	92
5.33 Unlocking of the escape wheel	93
5.34 Locking of the slave anchor	93
5.35 Spring reload	93
5.36 A summary of possible energy curves for constant force escapements and classification of the state of art escapements. Blue ovals are escapements which were studied during the thesis and the green oval gives the energy curve for the escapement presented in this chapter. Escapement on the right side of the figure from top to bottom are Girard-Perregaux escapement, Ulysse Nardin escapement and Nivarox escapement.	94
6.1 Vein over puncturing: F_a and F_r represents the applied and resistance force and α is the puncturing angle.	96
6.2 Retinal vein cannulation, (a) needle in contact with the vein, (b) needle punctures the vein, (c) injection is made, (d) needle retracts from the vein.	98
6.3 (a) Our tool, (b) graphical representation, (c) micro-converter mechanism, (d) puncture mechanism.	100
6.4 Stable states of the mechanism for $p_1 = 10[\mu m]$, puncturing occurs on switching from (a) pre-puncturing state to (b) post-puncturing state.	101
6.5 Strain energy of displacement driven bistable mechanism as function of its position x	102
6.6 Strain energy of displacement driven bistable mechanism where the mechanism position is denoted by the ball at (a) stable state s_1 , (b) unstable state u with no overload $x_u = 0$, (c) overload $x_u > 0$, (d) overload after surpassing s_2	103

6.7	Strain energy of programmable bistable mechanism for different values of p_1 , p_2 (a) $p_1 < p_1^{cr}$, (b) $p_1 > p_1^{cr}$, $p_2 = 0$, (c) $p_1 > p_1^{cr}$, $0 < p_2 < p_2^s$, (d) $p_1 > p_1^{cr}$, $p_2 = p_2^s$, (e) $p_1 > p_1^{cr}$, $p_2 = p_2^r$, (f) $p_1 > p_1^{cr}$, $p_2 > p_2^r$, (g) $p_1 > p_1^{cr}$, $-p_2^s < p_2 < 0$, (h) $p_1 > p_1^{cr}$, $p_2^s < p_2 < 0$, (i) $p_1 > p_1^{cr}$, $p_2 = -p_2^r$, (j) $p_1 > p_1^{cr}$, $p_2 < -p_2^r$	104
6.8	Mechanism deformation for (a) initial state, (b) pre-puncturing state, (c) unstable state, (d) post-puncturing state.	106
6.9	The puncture mechanism illustrating its main components and the programming inputs, p_1 , p_2	107
6.10	A 3D cross pivot for beam anchoring.	107
6.11	The needle tip with an integrated fluidic channel for drug injection.	108
6.12	3D rendering of the deformation of the puncture mechanism based on FEM simulations.	108
6.13	(a) Experimental setup, (b) Driving micro-metric screws and force sensor, (c) Interface between the sensor and the needle tip, (d) The puncture mechanism under microscope.	109
6.14	Strain energy of the puncture mechanism for $p_1 = 15[\mu m]$ on switching from pre-puncturing state s_1 to post-puncturing state s_2 based on FEM simulations.	110
6.15	Programming diagram giving the relation between the number of stable states and programming inputs.	111
6.16	The angular position of the needle tip as function of p_2 at $p_1 = 15[\mu m]$ based on numerical and experimental measurements.	111
6.17	The angular stroke of the needle tip versus p_1 based on numerical and experimental measurements.	112
6.18	The maximum force during energy release in quasi-static mode versus p_1 based on numerical and experimental measurements.	112
6.19	(a) Pig eye cannulation setup, (b) puncture mechanism in contact with the retinal vein.	113

List of Tables

3.1	Evaluation of DOS	31
4.1	DOS of the T-mechanism as a function of the programming inputs, p_1, p_2	49
4.2	Dimensions of the T-mechanism	54
4.3	Effect of the programming inputs on stiffness magnitude of the existing equilibrium states.	63
5.1	Components of the Snap Escapement.	79

1 Goals and Plan of the Thesis

1.1 Introduction and thesis motivation

The subject of this thesis is the stability analysis of compliant mechanisms, i.e., mechanical structures having at least one elastic element. Compliant elements are characterized by their stiffness relating force and deformation.

In the theory of stability, the stiffness of a mechanism at its equilibrium positions determines its stability behavior. Therefore, it is possible to control the stability response of a mechanism by tuning its stiffness. This motivated us to ask the following questions.

- To what extent can we modify the stability behavior of a compliant mechanism? Is it possible to precisely change the number, position, stiffness and stability of equilibrium states of mechanical structures?
- Is it possible to find a generic model which approximates the stiffness of programmable multi-stable structures? If yes, is this model sufficient to understand the qualitative stability behavior of the mechanism?
- What are the miniaturization limits of programmable multistable structures?
- How can programmable multistable structures be applied advantageously to horological devices and ophthalmology surgical tools?

1.2 Thesis objectives

The main objectives of this thesis are

1. Introduction of *programmable multistable mechanisms* whose stability behavior is modified by tuning stiffness. We call this process *stability programming*.

2. Applying programmable multistable mechanisms to mechanical watches and surgical tools.

These objectives will be achieved with the following steps.

1. *Present different design of programmable multistable mechanisms and establish a theoretical understanding of the concept of stability programming.* Analytical and numerical models will be used to model the stability behavior of these mechanisms for different boundary conditions. As case study, the T-mechanism is selected for further investigation.
2. *Verify experimentally the operation of the T-mechanism as a demonstrator of stability programming and validate our analytical computations.* A prototype of the T-mechanism is manufactured using electro-discharge machining and experimental setup is built to measure the reaction force of the mechanism for different programming inputs.
3. *Demonstrate the usefulness of the programmable multistable mechanisms to real life applications.* We developed a new surgical tool based on stability programming to be utilized for the treatment of retinal vein occlusion. Our medical device is manufactured out of glass using 3D femtolaser printing. The mechanical stability behavior is characterized using both numerical and experimental tools. The developed tool is used for the cannulation of pig eyes.
4. *Apply stability programming to mechanical watches.* A novel escapement is described, based on a programmable multistable mechanism is introduced where both the oscillator unlocking energy and oscillator energy impulse are repeatable. A demonstrator is built to verify the escapement operation.

1.3 Thesis structure

The thesis starts with a brief discussion of the notation of stability and the stability criteria of mechanical systems in Chapter 2. Then, a review of the current multistable mechanisms is given and the different techniques to tune the stability behavior are discussed.

In Chapter 3, the concept of stability programming is introduced. Different synthesis techniques are given. A case study of programmable multistable mechanisms (PMMs) is selected, the T-mechanism. A complete analytical model of the T-mechanism is derived from which the strain energy is represented as a polynomial whose coefficients are functions of the programming inputs. The effect of the programming inputs on the mechanism behavior is studied. Numerical simulations are provided to verify our concept.

In Chapter 4, the design of our experimental setup is given. A prototype of the T-mechanism was manufactured and characterized. The experimental results are provided and compared with the analytical and numerical calculations.

In Chapter 5, I integrated PMMs within the lever escapement to enable both repeatable unlocking energy and energy impulse of the oscillator. A complete descriptive analysis of the operation of the escapement is given which was verified by building a physical demonstrator.

In Chapter 6, I introduce the application of PMMs as medical devices to the treatment of the retinal vein occlusion. The advantages of PMMs compared to conventional multistable mechanisms are given on which the needle is designed. The proposed device was manufactured using 3D femto-laser printing out of glass. The stability behavior of the mechanism was characterized using both numerical analysis and experimental measurements. Clinical tests on pig eyes are described.

In Chapter 7, the thesis contributions are summarized along with potential applications of programmable multistable mechanisms.

2 State of the Art

In this chapter, we present a brief introduction to the theory of stability and its application to mechanical structures in Section 2.1. After that, we give a review over the recent work on multistable mechanisms and their applications in Section 2.2.

2.1 Stability

2.1.1 The theory of stability

Historically, physicists would like to find exact analytic solutions to differential equations arising from dynamical problems. By the end of the 19th century, it became clear that this was not always possible and they turned to the investigation of qualitative behavior such as the stability of *dynamical systems* [1].

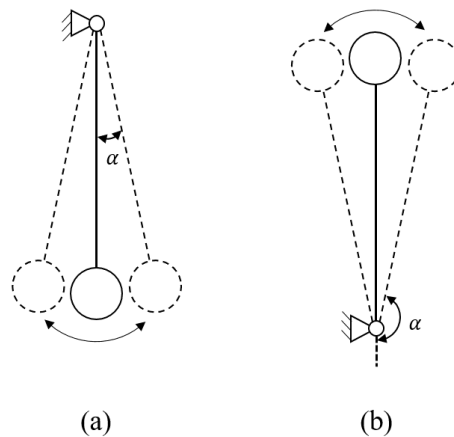


Figure 2.1 – (a) Pendulum, (b) inverted pendulum.

A common example illustrating the stability behavior of mechanical systems is the pendulum, shown in Figure 2.1(a) [2]. It consists of a mass connected to a frictionless pivot by a massless

rigid rod such that the mass swings freely under constant gravity.

The pendulum has an *equilibrium state* at $\alpha = 0$, meaning that the pendulum maintains this state unless perturbations are introduced. This is a *stable state* in the sense that placing the pendulum at small initial α , the pendulum oscillates around $\alpha = 0$, and this qualitative behavior persists when the pendulum is slightly perturbed. Moreover, when damping exists, oscillations decrease with α approaching zero.

The inverted pendulum occurs at the equilibrium state $\alpha = \pi$, as illustrated in Figure 2.1(b). This is an *unstable state* in the sense that for any initial value α close to π , the pendulum will diverge away from this state.

Figure 2.2 illustrates the qualitative behavior of the damped pendulum around its equilibrium states, where the phase diagrams show the dynamics of α and $\dot{\alpha} = \frac{d\alpha}{dt}$, as time t increases.

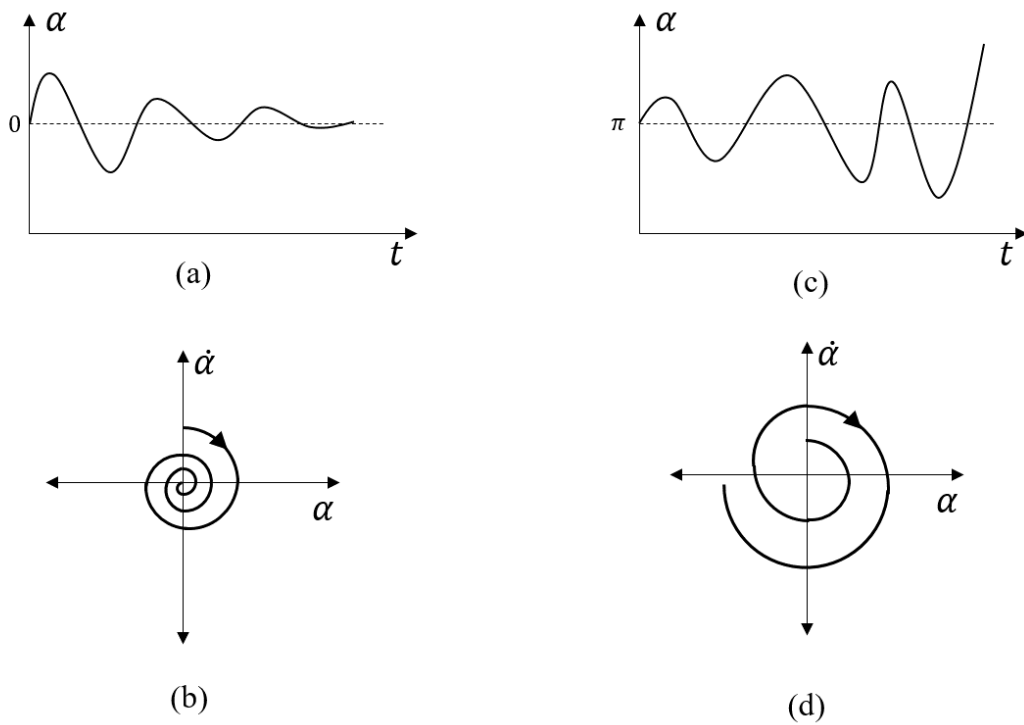


Figure 2.2 – Time response of the pendulum and phase diagram when its initial position is at (a,b) $\alpha = 0$, (c,d) $\alpha = \pi$.

2.1.2 Stability of compliant mechanisms

This thesis concerns stability of *compliant mechanisms*, i.e., mechanical devices consists of elastic elements. *Stiffness* is the ratio between imposed force and its resulting displacement. The stability behavior of compliant mechanisms can be characterized by their stiffness, from which the reaction force and strain energy can be deduced.

The stability of a compliant mechanism at an equilibrium state depends on the sign of the stiffness. If the stiffness is positive, the mechanism is stable. If the stiffness is negative, the mechanism is unstable. This defines the main criteria used for the qualitative analysis of the stability behavior of the mechanisms studied in this thesis. Since we mainly focus on compliant mechanisms with highly nonlinear stiffness, we use the *tangential stiffness*, defined as the first derivative of the mechanism reaction force with respect to its displacement to study the mechanism stability behavior [3].

2.2 Multistable mechanisms

Mechanisms can be designed to have highly nonlinear stiffness such that multiple stable states can exist. These mechanisms are called *multistable mechanisms* [4]. Common examples of multistable mechanisms are hair clips and bottle lids given in Figure 2.3. Figure 2.4 gives the strain energy, reaction force and stiffness of a bistable mechanism, where s_1 , s_2 correspond to the stable positions occurring at energy minima positions and u corresponds to the position of unstable state at the energy maximum.



Figure 2.3 – Hair clips and bottle lids as examples of bistable mechanisms

2.2.1 Examples of bistable mechanisms

Several multistable mechanisms were introduced in literature. Buckled beams are the most common example of bistable mechanisms. Buckling is a mechanical phenomenon occurring to slender beams when their axial load exceeds a critical value, known as buckling load [5]. Once this load is exceeded, the beam moves laterally and becomes bistable as illustrated in Figure 2.5.

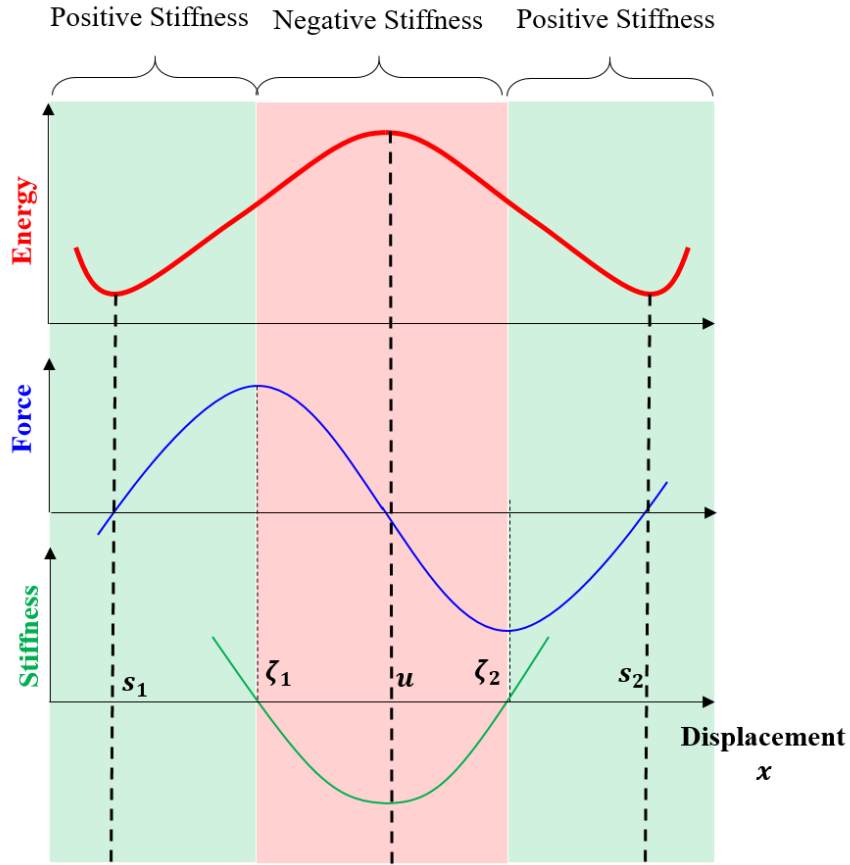


Figure 2.4 – Strain energy, reaction force and tangential stiffness of a bistable mechanism where s_1, s_2 are stable positions, u is unstable position and ζ_1, ζ_2 correspond to zero stiffness positions.

Saif [6] studied the stability behavior of axially loaded beam bistable mechanisms, when the axial load exceeds the critical load. Dehon [7] used a centrally pinned axially pre-stressed beam as a rotary bistable mechanism for constant force escapements in mechanical watches. Porter [8] studied the axial compressed S-shaped bistable beams for energy harvesting. One limitation of the buckled bistable beams is the need for two actuation sources, one for axial pre-stressing and the second one for lateral displacement.

Curved beams can function as bistable mechanisms requiring only one driving source. Qui presented the cosine-shaped bistable beams in Refs. [9, 10], see Figure 2.6. Also, Park [11] studied the behavior of cosine curved beams under electrostatic actuation. Wu [12] gave the conditions of bistability for the V-shaped beams. Kyrlov [13, 14] proposed the arc-shaped beams as bistable mechanisms under electrostatic actuation. Salinas [15] presented three points Bezier shaped beam as a bistable mechanism based on FEM simulations. Zhao [16] studied the effect of modifying the anchoring angle of curved beams on their stability behavior.

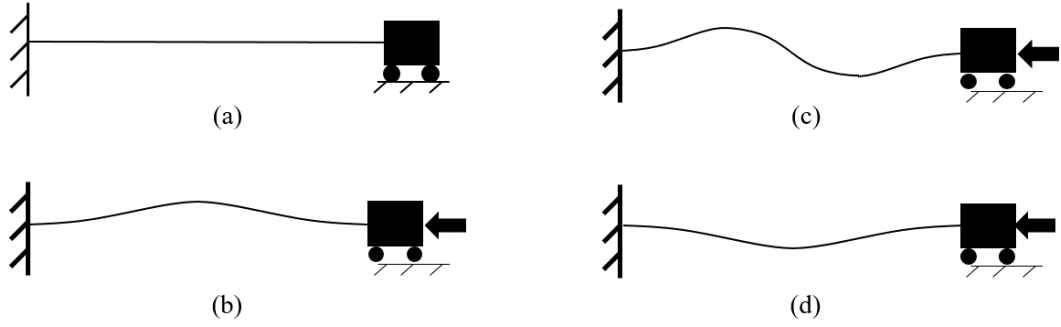


Figure 2.5 – Axially loaded bistable beam, (a) no axial load, (b) stable state of the beam, (c) unstable state of the beam, (d) second stable state of the beam.

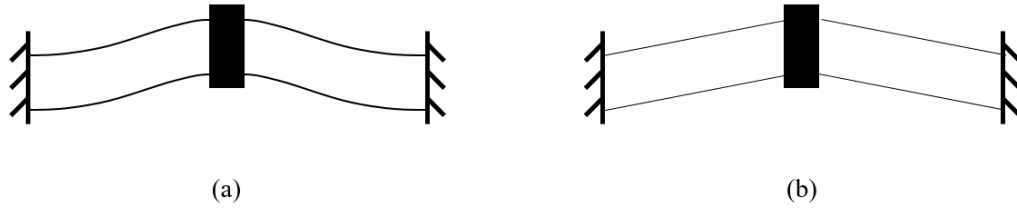


Figure 2.6 – Curved bistable beam mechanisms (a) cosine-shaped beam, (b) V-shaped beam.

Buckled bistable beams are easy to fabricate. However, their kinematic behavior and energy storage are strongly coupled. Moreover, they have small stroke. This motivated Sonmez [17] to introduce a long stroke bistable mechanism combining both buckled pinned pinned beams and cantilevers.

As well, Jensen [18, 19] introduced a new family of bistable mechanisms based on the slider crank and four bar mechanisms where the kinematics and the energy can be independently controlled. He gave the conditions for multistability of slider crank (Figure 2.7), double slider and four bar mechanisms.

On the microscale, Jensen introduced the Young's mechanism using pin joints for anchoring the mechanism to the wafer [20]. Using these pin joints, a linear translational motion mechanism was introduced by Gomm [21]. To avoid the high friction of these joints, Parkison [22] proposed flexible beams for the mechanism anchoring, however, this method is based on buckling which is not convenient for long stroke microscale devices.

Tension based joints were presented by Masters [23, 24] to construct long stroke bistable mechanisms. Using these joints, Wilcox [25, 26] extended the library of tension based bistable mechanisms and provided different techniques to micro-fabricate them. Luharuka [27, 28] used the tension based joints for constructing rotational bistable mechanisms.

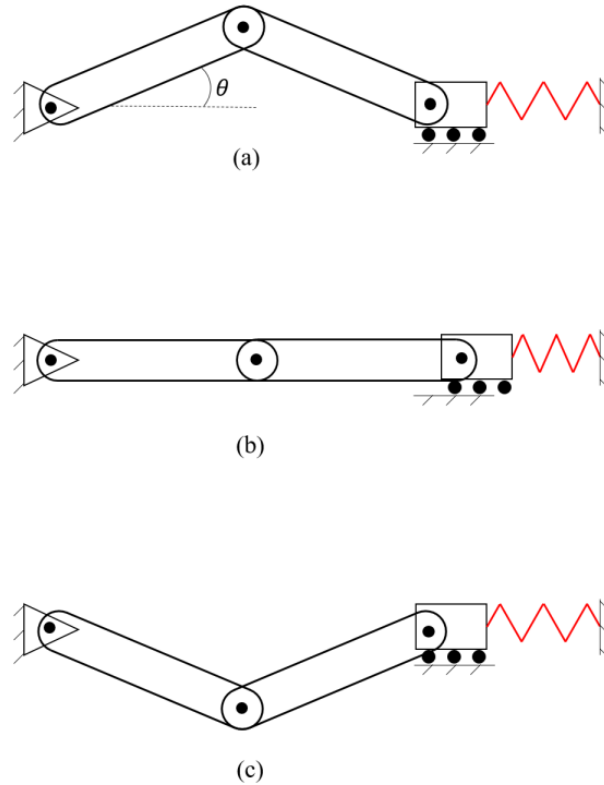


Figure 2.7 – A slider crank bistable mechanisms, (a) first stable state, (b) unstable state, (c) second stable state.

All the aforementioned mechanisms are planar mechanisms, where the actuation input and the mechanism output displacement exist in the same plane. This is not convenient for certain applications such as mirror controllers. Then, out of plane multistable mechanism were presented. An example of out of plane bistable mechanisms was introduced by Matoba [29] based on buckled cantilevers and tension bands. Lusk [30] introduced a spherical out of plane bistable mechanism using a planar Young's bistable mechanism and an out of plane joint. Hanna [31] presented an out of plane bistable mechanism based on topology optimization of origami structures. Foulds [32, 33, 34] presented a subfamily of bistable mechanisms based on rugs and ladder mechanisms. However, these mechanisms imply shocks and have high friction. Using the mismatch of thermal expansion coefficients of different materials, out of plane buckled U-shaped bistable cantilevers were proposed by Goessling [35].

For higher degree of multistability, i.e., number of stable states exceeds two, different combinations of bistable mechanisms were proposed. Oh [36, 37] introduced the theory and gave the conditions for building multistable mechanisms using serial connections of buckled bistable beam mechanisms.

Depending on the low stiffness of tension based bistable mechanism, Chen [38] introduced a tristable mechanism by combining two tension based bistable mechanisms in parallel. Similarly, a tristable mechanism was constructed by parallel combination of two Young's bistable mechanisms as given in [39]. Han built a 2-degree of freedom (DOF) quadrastable mechanism consisting of two frames of curved beams orthogonally connected allowing bistability in two orthogonal directions [40]. Orthogonal combinations of bistable mechanisms can result in multistability. Two initially curved beams orthogonally connected can demonstrate tristability and quadrastability [41, 42]. Gerson [43] introduced a long stroke multistable actuator through serial connection of arc shaped bistable beams.

Using symmetrical four bar mechanism, Pendleton [44] demonstrated tristability behavior. Chen studied the quadrastability conditions of the five bar mechanism [45]. Using Sarrus mechanism, a tristable mechanism was also introduced in [46]. Halverson developed long stroke rotational multistable mechanisms through the optimization of rolling contacts joints with non-uniform cams [47, 48]. Ohsaki gave the conditions for trusses multistability [49]. Hafez presented a 6-DOF multistable stage through combining three bistable beams in parallel [50].

Oberhammer [51] introduced a tristable mechanism based on electrostatic actuation of a three way switch. Through the interaction of inertial, elastic and magnetic forces, Zhao introduced a multistable mechanism in [16].

2.3 Selected applications

Multistable mechanisms are applied to different fields. In this section, we selected few applications.

- **Energy harvesting**

Bistable mechanisms have a broad spectrum due to their high speed on switching between their stable states. This allows their usage as broadband vibration energy harvesters with higher efficiency compared to resonant structures which are efficient only at a single frequency [52]. Four bar mechanisms [53] and pre-stressed S-shaped beams [8] were studied for vibrational energy harvester. As well, the V-shaped beams were optimized for energy harvesting as presented in [54].

- **Radio frequency switches**

Multistable mechanisms can maintain different deformations at zero force. This can be advantageous to low power radio frequency (RF) devices. Therefore, Baker [55], Nordquist [56], Michael [57] and Oberhammer [51] used multistable mechanisms as RF switches. Charlot [58] built a random access memory based on nano-wire bistable mechanisms.

- **Medical devices**

Statically balanced mechanisms have near to zero stiffness. They can be constructed using bistable mechanisms [59]. Statically balanced mechanisms can be employed as grippers as demonstrated by Hoetmer [60, 61] and Lassooij [62]. They can be utilized as artificial limbs [63, 64] as proposed by Wisse [65] and Chen [66].

- **Watchmaking**

Bistable mechanisms are used as part of constant force escapements for mechanical watches. Dehon used the double pinned bistable beam for Girard-Perregaux escapement [7]. Also, another escapement based on bistable beams was presented by Nivarox S.A. [67].

In chapter 5, a complete review of the application of bistable mechanisms to the watch-making field is given.

- **Miscellaneous**

Bistable mechanisms can be used for the automotive industry as accelerometers and trunk lids [68]. Also, they can be utilized as shock absorbers illustrated in [69].

In the dynamic mode, bistable mechanisms can be used as mass sensors through the detection of their transition frequency given by the Duffing effect [70]. Compared to the resonant sensors, mass sensing through resonant bistable mechanisms is easily detected in viscous medium.

In all the aforementioned mechanisms, the stability behavior is fixed depending on the dimensions and the material of the mechanisms. However, in certain applications such as energy harvesting and smart metamaterials, it is needed to modify the stability behavior as a function of the surrounding environment, e.g., driving signal amplitude or frequency. This in turns motivated us to present *programmable multistable mechanisms*, a new family of multistable mechanisms where the stability behavior can be modified. This is the main topic discussed in Chapters 3 - 7.

3 Stability Programming *

3.1 Introduction

Compliant mechanisms perform a function by their elastic deformation via *actuation inputs*. Their qualitative behavior can be characterized by their stable states where strain energy is minimal and *multistable mechanisms* are those having more than one stable state, the number of the stable states is called *degree of stability* (DOS). Conventional multistable mechanisms have a fixed DOS. In this thesis, we examine a family of multistable mechanisms, *programmable multistable mechanisms* (PMM), where *programming inputs* can modify their DOS.

Section 3.2 gives an overview of PMMs. In Section 3.3, we introduce a method for synthesizing PMMs which we use to build the main mechanism of this thesis, the T-mechanism, as described in Section 3.4. Section 3.5 gives an analytical derivation of the reaction force of this mechanism as a polynomial of the actuation input. This expression allows us to characterize the stability behavior of the T-mechanism based on the zeros of the reaction force polynomial and its discriminant.

Section 3.6 provides a complete description of the stability behavior of the T-mechanism in terms of its programming inputs. This consists of the *programming diagram* illustrating DOS as function of programming inputs and *equilibrium and zero stiffness diagrams*, where one programming input is varied and the other is fixed.

Finally, Section 3.7 gives numerical validation of our analytical results using the finite element method.

*The content of this chapter has been published as Mohamed Zanaty, Ilan Vardi, and Simon Henein, "Programmable multistable mechanisms: Synthesis and modeling." *Journal of Mechanical Design* 140, no. 4 (2018): 042301.

3.2 Programmable multistable mechanisms (PMMs)

3.2.1 Conventional multistable mechanisms

Conventional multistable mechanisms are those having fixed stability behavior. They have application to energy harvesting [71, 72], radio frequency switches [51] and medical instrumentation [73].

Examples are orthogonal beam mechanisms [42, 41], serial multistable mechanisms [37], tristable four bar mechanisms [37, 74], five bar tristable mechanisms [45], Sarrus multistable mechanisms [46], double Young tristable mechanism [39] and rolling contact multistable mechanisms based on non-uniform cams [48]. Multistable mechanisms utilizing the nonlinear interaction between electrostatic and electromagnetic forces were developed in [51, 16].

Synthesis of multistable mechanisms has been done by parallel and serial connection of bistable mechanisms [37, 39]. A classification of multistable mechanisms based on their kinematics and their strain energy was presented in [75].

3.2.2 Definitions

The stability behavior of multistable mechanisms can be characterized in terms of reaction force which is related to the strain energy and stiffness. We give formal definitions to make these concepts as precise as possible.

1. Our mechanisms have 1-DOF, an *actuation input* x , assumed to be a linear displacement.
2. $E(x)$ is the *strain energy*, the energy stored in the mechanism due to its elastic deformation.
3. *Reaction force* is the component of mechanism restoring force along the direction of its displacement x and is given by

$$F = \frac{dE}{dx}. \quad (3.1)$$

Note that according to our definition, reaction force is a scalar.

4. *Secant stiffness* is defined by

$$k_s = \frac{F}{x}. \quad (3.2)$$

5. *Tangential stiffness* is defined by

$$k_t = \frac{dF}{dx}. \quad (3.3)$$

Remark. Secant stiffness is used for the derivation of reaction force in Section 3.5 and tangential stiffness is for the evaluation of zero stiffness positions in Section 3.6. The difference between the two stiffness is explained in [76, p. 162].

6. *Equilibrium positions* are values of the actuation input at which the reaction force is zero. In the generic case, an equilibrium position is *stable* when its tangential stiffness is positive and *unstable* when it is negative. This thesis only deals with this generic case, see [1] for details.
7. *Degree of stability* (DOS) is the number of distinct stable states of a multistable mechanism (not considered with multiplicity).
8. We call a 1-DOS mechanism *monostable*, a 2-DOS mechanism *bistable*, a 3-DOS mechanism *tristable* and a 4-DOS mechanism *quadrastable*.

3.2.3 Multistability programming

Programmable multistable mechanisms are $(N + 1)$ -DOF mechanisms with one actuation input and N *programming inputs*, where N is the *degree of programming* (DOP).

The stability behavior of these mechanisms with respect to their actuation input can be modified on varying the programming inputs.

Figure 3.1 gives a block diagram representation of a 3-DOP multistable mechanism and illustrates the effect of the programming inputs on its strain energy. The mechanism can be programmed to be monostable or bistable. Programming inputs can be directly imposed or controlled via an electric current, magnetic field or pressure.

The best previously known programmable bistable mechanism is the axially loaded beam in which axial load switches monostability to bistability [6, 77], this thesis generalizes this concept. Previous work has also considered electrically modified axial load [78], so the results of this thesis are not limited to mechanical programming.

A special PMM exhibiting monostability up to quadrastability was applied to ocean wave energy harvesting [72] and bistable Miura origami mechanisms were connected serially to produce PMM's [79]. These papers do not provide an analysis of the effect of the programming inputs on DOS, position of equilibrium states, zero stiffness states and the stiffness of stable states as is done in our work.

The main results of this work are:

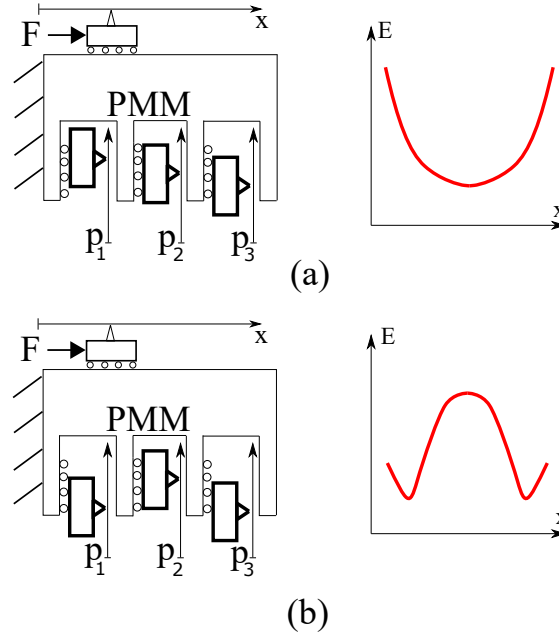


Figure 3.1 – Block diagram representation of a 3-DOP PMM programmed to be (a) monostable, (b) bistable.

1. Generic methods for synthesizing PMM's.
2. Definition of parameters characterizing PMM's.
3. An explicit analytical modeling of 2-DOP T-connected PMM's.
4. Analytical estimate of PMM constant force regimes.

3.3 Synthesis

3.3.1 General method

PMMs can be synthesized by combining programmable bistable mechanisms (PBM) to obtain a $DOS \geq 2$. This method consists of two steps as illustrated in Figure 3.2: the first step is *bistability programming* where PBMs are constructed, the second step is combining these PBMs. This method can be simply applied for any bistable mechanisms from literature.

Bistability programming refers to the process of introducing a programming input to a monostable mechanism to produce a PBM. We then combine these PBMs.

The 2-DOP T-combination is the connection where the base of one PBM is connected to the actuation block of the other such the actuation directions are orthogonal, as illustrated in Figure 3.3.

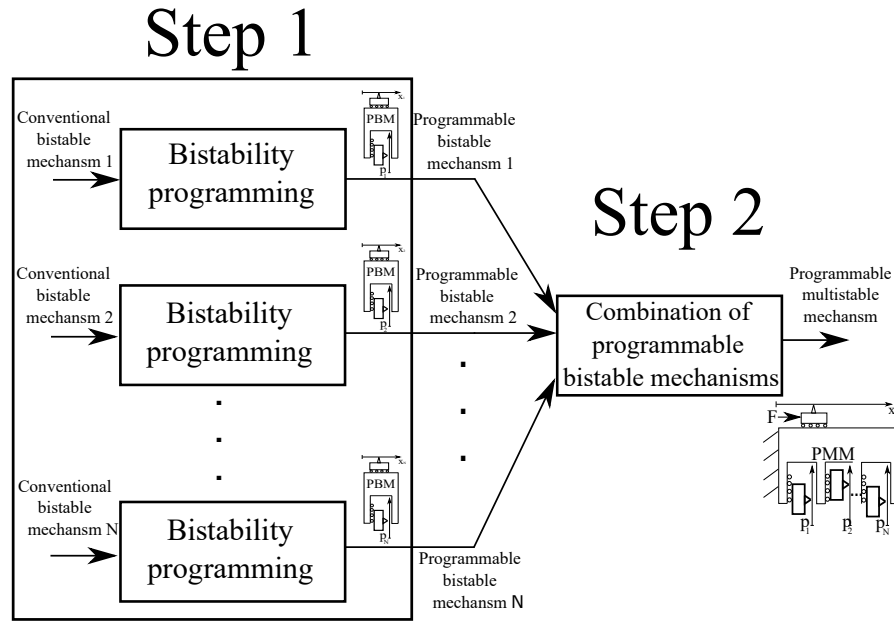


Figure 3.2 – Synthesis of PMMs.

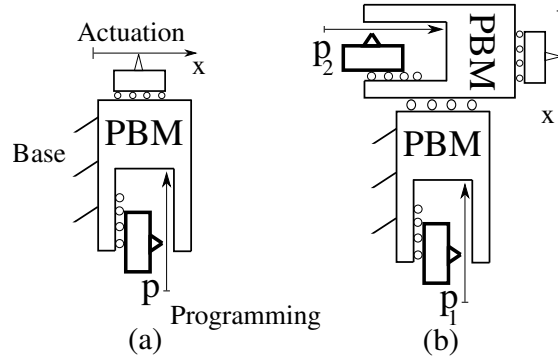


Figure 3.3 – Block diagram representation of (a) PBM, (b) 2-DOP T-combination.

3.3.2 Basic example

A simple example of PBM is the double parallelogram mechanism (DPM) shown in Figures 3.4 and 3.5(a). It consists of two horizontal beams centrally connected by the actuation block where the actuation input x is imposed. The beams are fixed at one extremity and axially guided at the other extremity where the programming input p is applied.

The T-combination of two DPMs is shown in Figure 3.5(b). This mechanism can be programmed to be monostable, bistable, tristable and quadrastable, as shown in Figure 3.6.

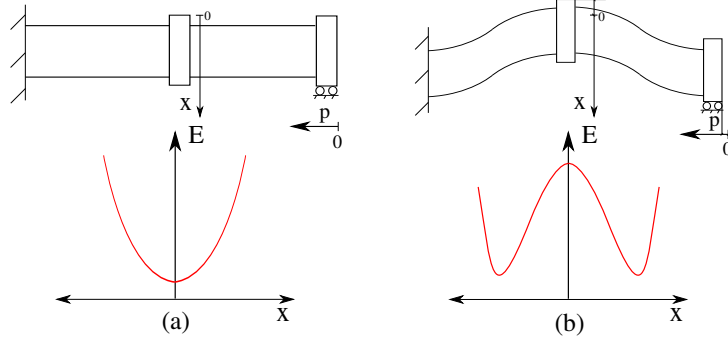


Figure 3.4 – Double parallelogram mechanism and its strain energy when programmed to be (a) monostable, (b) bistable.

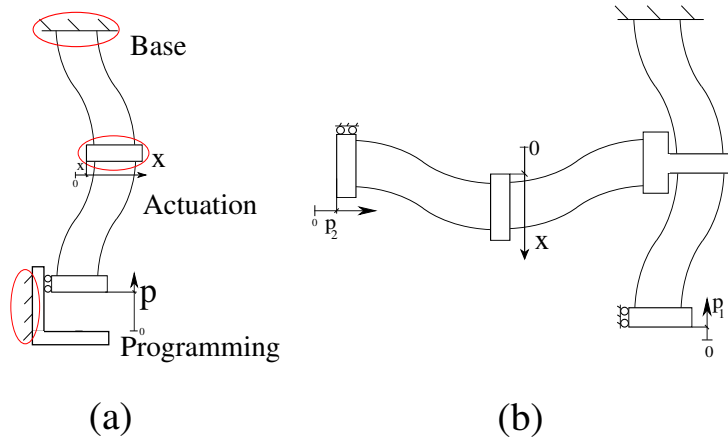


Figure 3.5 – (a) DPM connection blocks, (b) 2-DOP T-combination of DPMs.

3.3.3 T-connection versus serial and parallel connections

Methods for connecting PBM are the T-connection and the well-known serial and parallel connections, see Figure 3.7, the parallel connection is only applicable to tension based bistable mechanisms [39, 38].

This thesis focuses on the T-connection since it has five distinct stability regions whereas the serial and parallel connections only have four. The T-mechanism has drawbacks, the stiffness of bistable module depends on its driving bistable module, see Sections 3.4 and 3.5, so the size of the mechanism increases faster with increasing DOS as compared to serial and parallel configurations.

3.4 T-mechanism

The main focus of this thesis is the *T-mechanism* shown in Figure 3.8 (see Figure 3.18 for a 3-D FEM rendering). It is a refinement of the basic example of Section 3.3.2 where a spring is used to load axially the horizontal DPM.

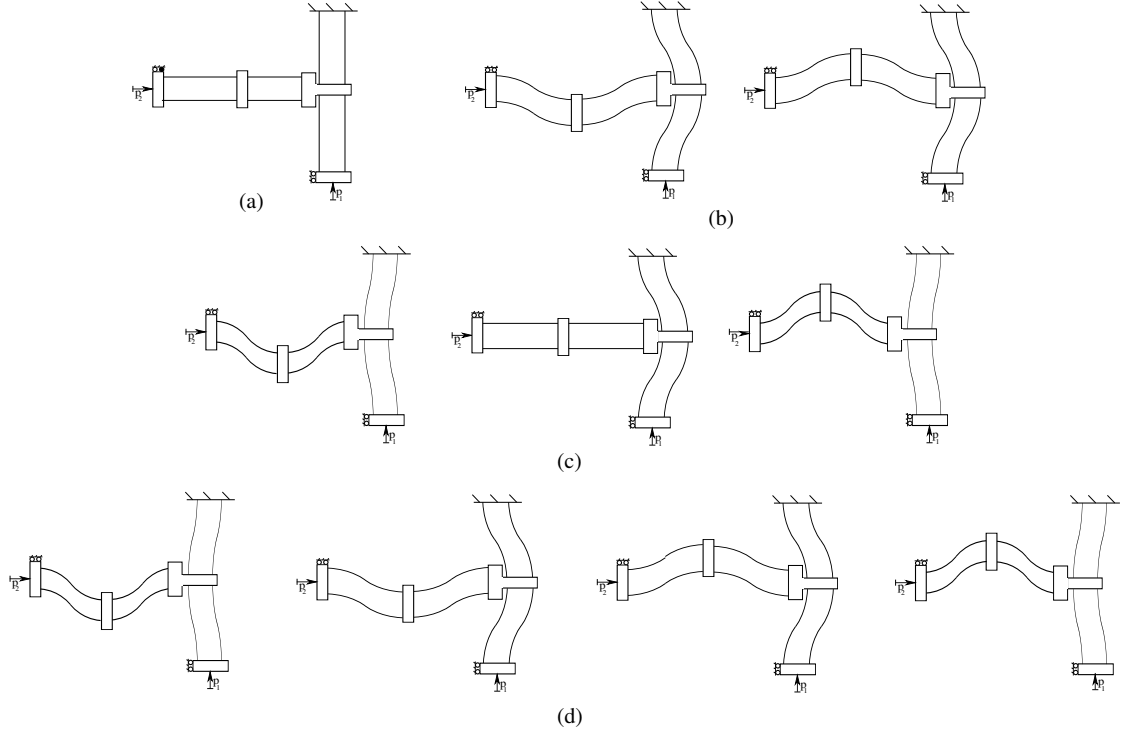


Figure 3.6 – Stable states of the 2-DOP T-mechanism programmed to be (a) monostable, (b) bistable, (c) tristable, (d) quadrastable.

We call the horizontal DPM *module 1*, with beams of length ℓ_1 , width w , thickness t_1 and moment of inertia of the cross-section I_1 and the vertical DPM by *module 2*, with beams of length ℓ_2 , width w , thickness t_2 and moment of inertia of the cross-section I_2 . Module 1 is axially loaded by a parallelogram spring with beams of length ℓ_r , width w , thickness t_r and moment of inertia of the cross-section I_r , as shown in Figure 3.8(c). We call this spring the *programming spring*.

3.4.1 Operation of the mechanism

The T-mechanism of Figure 3.8 has one actuation input x and two programming inputs p_1, p_2 . The actuation block of module 2 is displaced transversely by x . In its axial direction, module 2 is displaced by λ_2 at one extremity and has axial load N_2 . It is axially displaced by p_2 at its other extremity.

Since the two modules are T-combined, module 1 is displaced transversely by λ_2 . In its axial direction, module 1 is displaced by λ_1 under axial load N_1 . The programming spring is loaded transversely by the displacement p_1 which imposes an axial load N_1 on module 1.

Multistability programming of the T-mechanism relies on DPMs buckling imposed by the programming inputs p_1, p_2 .

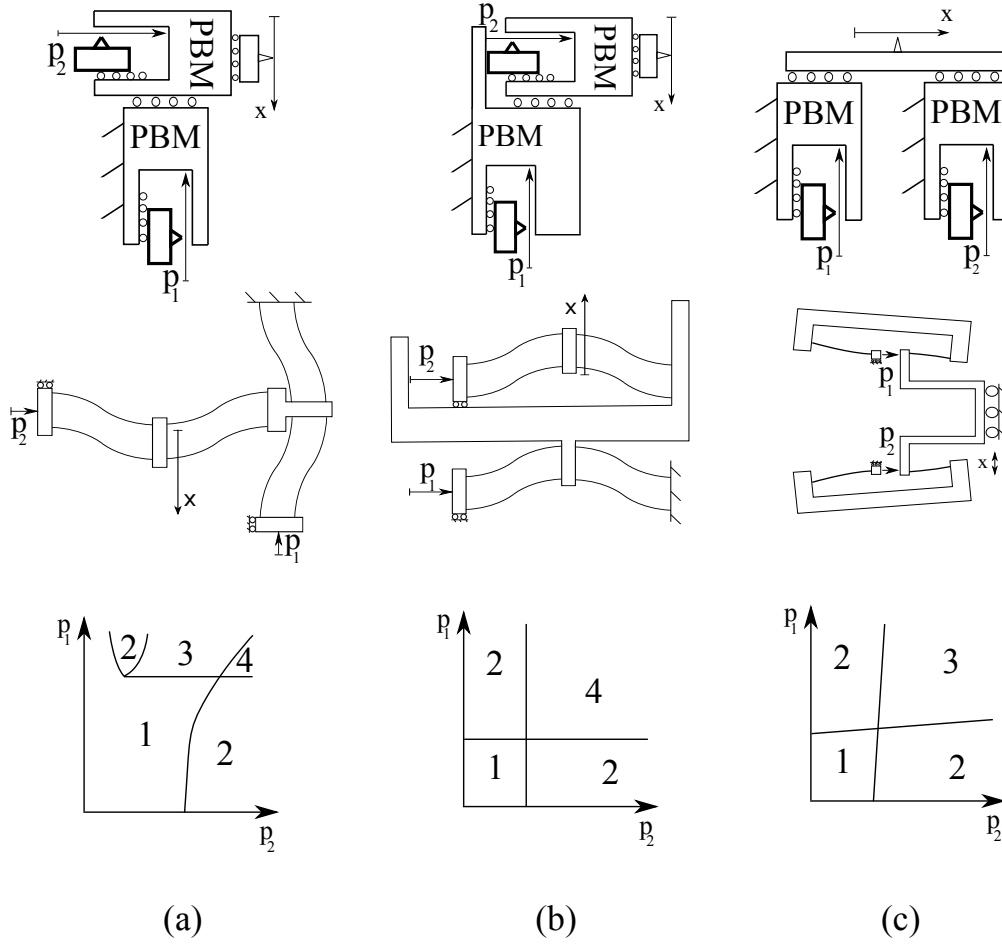


Figure 3.7 – Block diagram representation, example mechanism and DOS diagram of (a) T-connection, (b) serial connection, (c) parallel connection.

- If p_1, p_2 are both smaller than the critical buckling loads p_1^{cr} and p_2^{cr} of modules 1 and 2, respectively, the mechanism is monostable.
- If $p_1 < p_1^{cr}$ and $p_2 > p_2^{cr}$, only module 2 buckles and the mechanism is bistable.
- If $p_1 > p_1^{cr}$, the mechanism can be monostable, bistable, tristable or quadrastable depending on p_2 . There are values p_2^a, p_2^b , with $p_2^a < p_2^b$, such that:
- If $p_2 < p_2^a$, the mechanism is monostable, if $p_2^a < p_2 < p_2^b$, the mechanism is bistable, if $p_2^b < p_2 < p_2^{cr}$, the mechanism is tristable and quadrastable when $p_2 > p_2^{cr}$.

The physical significance of p_2^a and p_2^b is that module 1 is known to buckle when $p_1 > p_1^{cr}$ and has three equilibrium states at $\lambda_2 = \lambda_2^a, \lambda_2^b, \lambda_2^c$, where $\lambda_2^a < \lambda_2^b < \lambda_2^c$ with λ_2^a, λ_2^c stable and λ_2^b unstable, see [80]. Then $p_2^a = \lambda_2^a, p_2^b = \lambda_2^b$, as follows from equation (4.3) at $x = 0$.

Remark. If $p_2^{cr} > p_2^b$, the mechanism can not be tristable or quadrastable. Moreover, p_2^a, p_2^b, p_2^{cr} depend on p_1 .

3.4.2 Dimensions of the mechanism

The relative dimensions of module 1, module 2 and the programming spring determine the values of p_1^{cr} , p_2^a , p_2^b , p_2^{cr} and the possible DOS as it will be discussed in Section 3.6.

We use the following dimensionless parameters to represent the relative dimensions of the T-mechanism

- Stiffness ratio of module 1: $\eta_1 = I_r \ell_1^3 / (I_1 \ell_r^3)$.
- Stiffness ratio of module 2: $\eta_2 = I_1 \ell_2^3 / (I_2 \ell_1^3)$.
- length ratio of module 2: $\alpha_2 = \ell_2 / \ell_1$.

In order to fully illustrate multistability programming we choose η_1, η_2, α_2 where the T-mechanisms can exhibit monostable, bistable, tristable or quadrastable behavior. Figure 3.9 illustrates possible DOS for a range of η_1, η_2 and different values of α_2 . These values satisfy the conditions Euler-Bernoulli theory and we believe that the computations of this thesis hold for the values given in Figure 3.9(b), see [81], we refer to the range of values given in this figure as *admissible* η_1, η_2 .

In the main example of this thesis, we select the physical dimensions $\ell_1 = 12[mm]$, $\ell_2 = 12[mm]$, $\ell_r = 3[mm]$, $t_1 = 100[\mu m]$, $t_2 = 60[\mu m]$, $t_r = 140[\mu m]$, $w = 3[mm]$ with Young's modulus $Y = 210[GPa]$. This gives $\eta_1 = 176$, $\eta_2 = 4.6$, $\alpha_2 = 1$, the point highlighted in Figure 3.9(b).

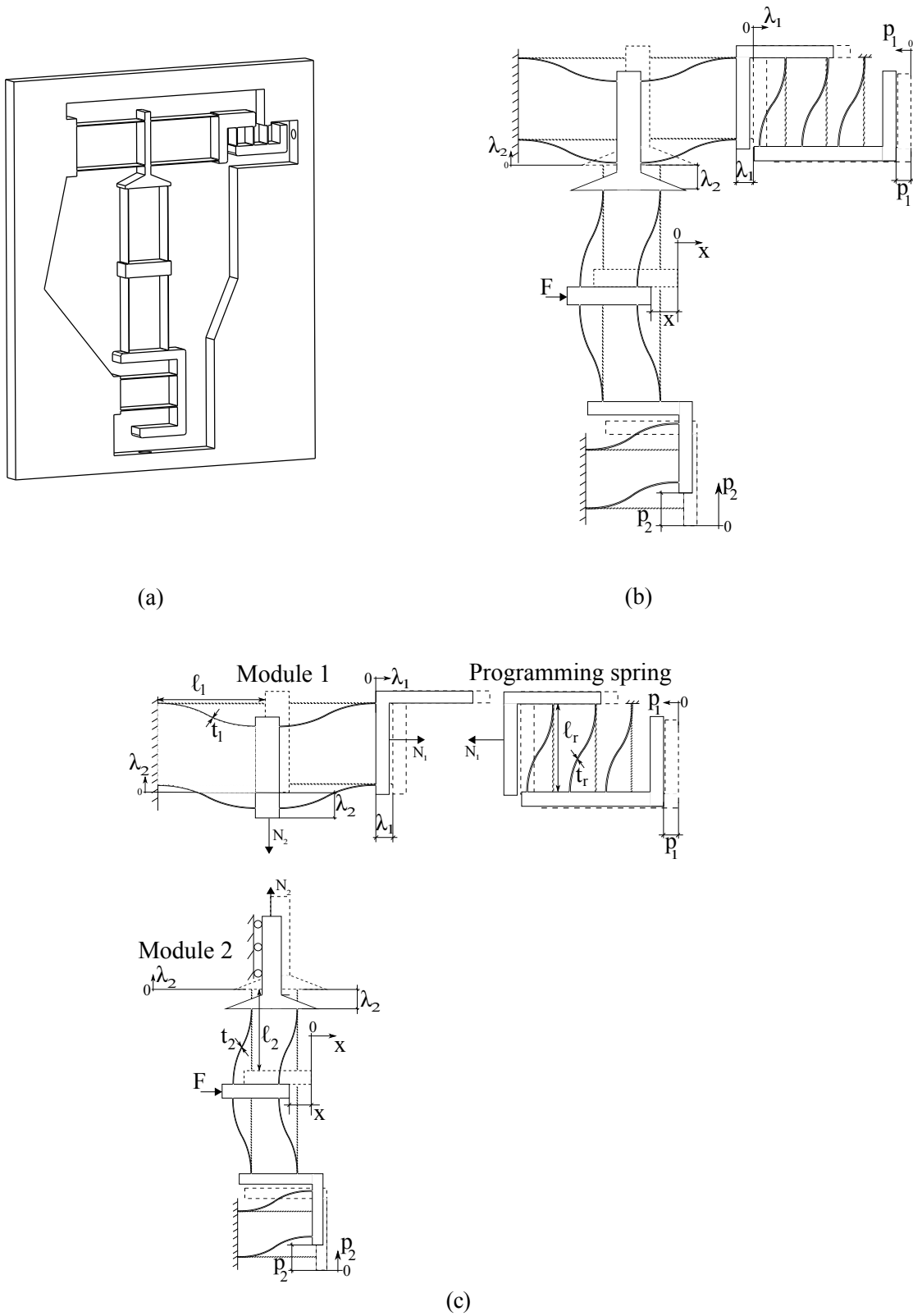


Figure 3.8 – (a) Constructed T-mechanism, (b) top view, (c) main components.

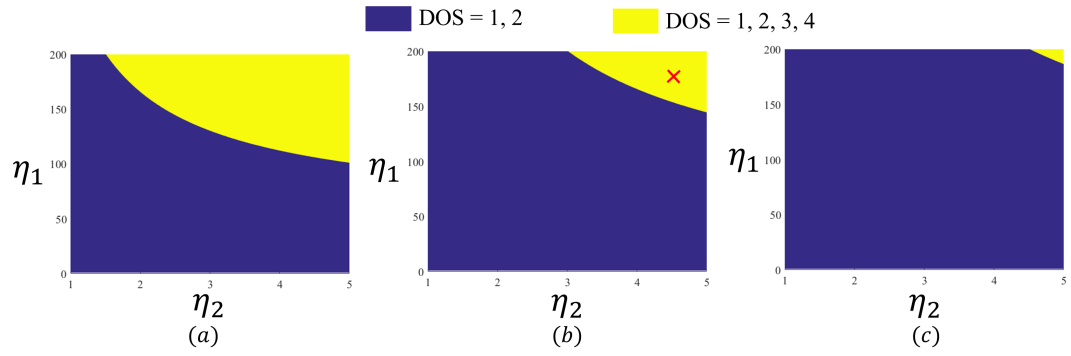


Figure 3.9 – Range of DOS for admissible η_1, η_2 for (a) $\alpha_2 = 0.5$, (b) $\alpha_2 = 1$, (c) $\alpha_2 = 1.5$.

3.5 Analytical model

In this section, we derive the strain energy and the reaction force of the T-mechanism based on Euler-Bernoulli theory [5]. The model is valid under the following assumptions, referring to Figure 3.8,

1. A linear elastic material is used.
2. Beam length is greater than beam thickness so that shear strain can be neglected.
3. Actuation force F is applied to the center of the central block of module 2.
4. Module 2 is connected to the central block of module 1.
5. Axial shortening of module 1 is an order of magnitude less than the axial shortening of module 2, i.e., $\lambda_1 \ll \lambda_2$.
6. The displacement range of mechanism is within its intermediate range [75].
7. Axial load of each beam is inferior to its buckling load with both ends fixed against rotation.

Our analysis consists of the following steps:

1. Compute the zero load stiffness and zero stiffness load of DPMs of the T-mechanism in terms of their dimensions and the material properties.
2. Express the relation between the axial shortening λ_1, λ_2 and the programming inputs p_1, p_2 and the actuation input x .
3. Calculate the axial load N_1 imposed on module 1 as function of p_1, p_2, x .
4. Calculate the secant stiffness $k_s^{p_1}$ of module 1 based on the axial load N_1 in terms of its zero load stiffness and zero stiffness load.
5. Calculate the axial load N_2 applied on module 2 as function of p_1, p_2, x .
6. Calculate the secant stiffness k_s of the T-mechanism, equal to the secant stiffness $k_s^{p_2}$ of module 2.
7. Calculate the reaction force of the T-mechanism using Hooke's law, $F = k_s x$.
8. Calculate the strain energy of the T-mechanism by integrating its reaction force with respect to displacement.
9. Define dimensionless mechanism parameters.

10. Calculate the zero load stiffness and zero stiffness load in terms of dimensionless parameters.
11. Derive dimensionless reaction force and tangential stiffness in terms of dimensionless parameters.
12. Express dimensionless reaction force and tangential stiffness in terms of cubic polynomials.

3.5.1 Zero load stiffness and zero stiffness load

Zero load stiffness is the secant stiffness of the mechanism at zero axial load. The zero load stiffness $k_0^{p_1}$ of module 1 and $k_0^{p_2}$ of module 2 are [76, p. 160]

$$k_0^{p_1} = \frac{48Y I_1}{\ell_1^3}, \quad k_0^{p_2} = \frac{48Y I_2}{\ell_2^3}. \quad (3.4)$$

where Y is Young's modulus of the beams, $I_1 = wt_1^3/12$ and $I_2 = wt_2^3/12$ are the second moment of inertia of the beams of module 1 and module 2, respectively.

Zero stiffness load is the axial load at which the secant stiffness of the mechanism is zero. The zero stiffness loads $N_0^{p_1}$ of module 1 and $N_0^{p_2}$ of module 2 are [76, p. 68]

$$N_0^{p_1} = \frac{2\pi^2 Y I_1}{\ell_1^2}, \quad N_0^{p_2} = \frac{2\pi^2 Y I_2}{\ell_2^2}. \quad (3.5)$$

The secant stiffness k_s^r of the programming spring is well-approximated by [76, p. 208]

$$k_s^r = \frac{24Y I_r}{\ell_r^3}, \quad (3.6)$$

where it is assumed that the axial load has a negligible effect on the stiffness of the programming spring.

3.5.2 Axial shortening

The axial shortening of module 2 is [76, p. 61]

$$\lambda_2 = p_2 - \frac{6x^2}{5\ell_2}. \quad (3.7)$$

Since module 1 and module 2 are T-combined, the axial displacement of module 2 equals the

transverse displacement of module 1, so λ_2 leads to an axial shortening

$$\lambda_1 = \frac{6\lambda_2^2}{5\ell_1} \quad (3.8)$$

of module 1. By direct substitution of equation (3.7) into equation (3.8), the axial shortening of module 1 becomes

$$\lambda_1 = \frac{216}{125\ell_1\ell_2^2}x^4 - \frac{72p_2}{25\ell_1\ell_2}x^2 + \frac{6p_2^2}{5\ell_1}. \quad (3.9)$$

3.5.3 Axial loads

Module 1 imposes an axial load N_2 on module 2 as illustrated in Figure 3.8. From Hooke's law,

$$N_2 = k_s^{p_1} \lambda_2, \quad (3.10)$$

where $k_s^{p_1}$ is the secant transverse stiffness of module 1 which equals [76, p. 69]

$$k_s^{p_1} = k_0^{p_1} \left(1 - \frac{\pi^2 N_1}{10N_0^{p_1}} \right). \quad (3.11)$$

The force N_1 imposed by the programming spring on module 1 depends on p_1 and is calculated using Hooke's law

$$N_1 = k_s^r (p_1 - \lambda_1).$$

By direct substitution from equation (3.9), the axial load on module 1 is

$$N_1 = k_s^r \left(p_1 - \frac{216x^4}{125\ell_1\ell_2^2} + \frac{72p_2x^2}{25\ell_1\ell_2} - \frac{6p_2^2}{5\ell_1} \right). \quad (3.12)$$

By direct substitution from equation (3.12) into equation (3.11), the transverse stiffness of module 1 is

$$\begin{aligned} k_s^{p_1} = & \left(k_0^{p_1} - \frac{\pi^2 k_0^{p_1} k_s^r p_1}{10N_0^{p_1}} + \frac{6\pi^2 k_0^{p_1} k_s^r p_2^2}{50N_0^{p_1} \ell_1} \right) - \frac{72\pi^2 k_0^{p_1} k_s^r p_2}{250\ell_1\ell_2 N_0^{p_1}} x^2 \\ & + \frac{216\pi^2 k_0^{p_1} k_s^r}{1250\ell_1\ell_2^2 N_0^{p_1}} x^4. \end{aligned} \quad (3.13)$$

The axial load N_2 of module 2 is found by direct substitution of equation (3.7), (3.13) into

equation (3.10).

$$\begin{aligned}
 N_2 = & \left(k_0^{p_1} p_2 - \frac{\pi^2 k_0^{p_1} k_s^r p_1 p_2}{10 N_0^{p_1}} + \frac{6\pi^2 k_0^{p_1} k_s^r p_2^3}{50 N_0^{p_1} \ell_1} \right) \\
 & - \left(\frac{6k_0^{p_1}}{5\ell_2} - \frac{6\pi^2 k_0^{p_1} k_s^r p_1}{50 N_0^{p_1} \ell_2} + \frac{108\pi^2 k_0^{p_1} k_s^r p_2^2}{250 N_0^{p_1} \ell_1 \ell_2} \right) x^2 \\
 & + \frac{648\pi^2 k_0^{p_1} k_s^r p_2}{1250 N_0^{p_1} \ell_1 \ell_2^2} x^4 - \frac{1296\pi^2 k_0^{p_1} k_s^r}{6250 N_0^{p_1} \ell_1 \ell_2^3} x^6.
 \end{aligned} \tag{3.14}$$

3.5.4 Secant stiffness

The secant stiffness k_s of the T-mechanism equals the secant stiffness of module 2

$$k_s = k_s^{p_2}. \tag{3.15}$$

The secant stiffness of module 2 depends on its axial load N_2 [76, p. 69]

$$k_s^{p_2} = k_0^{p_2} \left(1 - \frac{\pi^2 N_2}{10 N_0^{p_2}} \right). \tag{3.16}$$

By substitution from equations (3.14), (3.15) into equation (3.16), the secant stiffness of the T-mechanism becomes

$$\begin{aligned}
 k_s^t = & \left(k_0^{p_2} - \frac{\pi^2 k_0^{p_2} k_0^{p_1} p_2}{10 N_0^{p_2}} + \frac{\pi^4 k_0^{p_2} k_0^{p_1} k_s^r p_1 p_2}{100 N_0^{p_2} N_0^{p_1}} - \frac{6\pi^4 k_0^{p_2} k_0^{p_1} k_s^r p_2^3}{500 N_0^{p_2} N_0^{p_1} \ell_1} \right) \\
 & + \left(\frac{6\pi^2 k_0^{p_2} k_0^{p_1}}{50 N_0^{p_2} \ell_2} - \frac{6\pi^4 k_0^{p_2} k_0^{p_1} k_s^r p_1}{500 N_0^{p_2} N_0^{p_1} \ell_2} + \frac{108\pi^4 k_0^{p_2} k_0^{p_1} k_s^r p_2^2}{2500 N_0^{p_2} N_0^{p_1} \ell_1 \ell_2} \right) x^2 \\
 & - \frac{648\pi^4 k_0^{p_2} k_0^{p_1} k_s^r p_2}{12500 N_0^{p_2} N_0^{p_1} \ell_1 \ell_2^2} x^4 + \frac{1296\pi^4 k_0^{p_2} k_0^{p_1} k_s^r}{62500 N_0^{p_2} N_0^{p_1} \ell_1 \ell_2^3} x^6.
 \end{aligned} \tag{3.17}$$

3.5.5 Reaction force

The reaction force of the T-mechanism follows Hooke's law

$$F = k_s x.$$

Direct substitution from equation (3.17) yields

$$\begin{aligned}
 F = & \left(k_0^{p_2} - \frac{\pi^2 k_0^{p_2} k_0^{p_1} p_2}{10 N_0^{p_2}} + \frac{\pi^4 k_0^{p_2} k_0^{p_1} k_s^r p_1 p_2}{100 N_0^{p_2} N_0^{p_1}} - \frac{6\pi^4 k_0^{p_2} k_0^{p_1} k_s^r p_2^3}{500 N_0^{p_2} N_0^{p_1} \ell_1} \right) x \\
 & + \left(\frac{6\pi^2 k_0^{p_2} k_0^{p_1}}{50 N_0^{p_2} \ell_2} - \frac{6\pi^4 k_0^{p_2} k_0^{p_1} k_s^r p_1}{500 N_0^{p_2} N_0^{p_1} \ell_2} + \frac{108\pi^4 k_0^{p_2} k_0^{p_1} k_s^r p_2^2}{2500 N_0^{p_2} N_0^{p_1} \ell_1 \ell_2} \right) x^3 \\
 & - \frac{648\pi^4 k_0^{p_2} k_0^{p_1} k_s^r p_2}{12500 N_0^{p_2} N_0^{p_1} \ell_1 \ell_2^2} x^5 + \frac{1296\pi^4 k_0^{p_2} k_0^{p_1} k_s^r}{62500 N_0^{p_2} N_0^{p_1} \ell_1 \ell_2^3} x^7.
 \end{aligned} \tag{3.18}$$

3.5.6 Strain energy

The strain energy E of the T-shaped mechanism is the integral of its reaction force F with respect to its displacement x , and integrating equation (3.18) gives

$$\begin{aligned}
 E = & \left(\frac{k_0^{p_2}}{2} - \frac{\pi^2 k_0^{p_2} k_0^{p_1} p_2}{20 N_0^{p_2}} + \frac{\pi^4 k_0^{p_2} k_0^{p_1} k_r p_1 p_2}{200 N_0^{p_2} N_0^{p_1}} \right. \\
 & \left. - \frac{3\pi^4 k_0^{p_2} k_0^{p_1} k_r p_2^3}{500 N_0^{p_2} N_0^{p_1} \ell_1} \right) x^2 + \left(\frac{3\pi^2 k_0^{p_2} k_0^{p_1}}{100 N_0^{p_2} \ell_2} - \frac{3\pi^4 k_0^{p_2} k_0^{p_1} k_r p_1}{1000 N_0^{p_2} N_0^{p_1} \ell_2} \right. \\
 & \left. + \frac{27\pi^4 k_0^{p_2} k_0^{p_1} k_r p_2^2}{2500 N_0^{p_2} N_0^{p_1} \ell_1 \ell_2} \right) x^4 - \frac{27\pi^4 k_0^{p_2} k_0^{p_1} k_r p_2}{3125 N_0^{p_2} N_0^{p_1} \ell_1 \ell_2^2} x^6 \\
 & + \frac{81\pi^4 k_0^{p_2} k_0^{p_1} k_r}{31250 N_0^{p_2} N_0^{p_1} \ell_1 \ell_2^3} x^8,
 \end{aligned} \tag{3.19}$$

where the constant of integration is set to zero, since we are only interested in strain energy difference.

3.5.7 Normalization

Normalization enables our analysis to be independent of physical dimensions. We introduce the following dimensionless parameters:

1. actuation input $\hat{x} = x/\ell_2$,
2. programming inputs $\hat{p}_1 = p_1/\ell_1$, $\hat{p}_2 = p_2/\ell_2$,

and dimensionless properties:

1. secant stiffness $\hat{k}_s = k_s \ell_2^3/(Y I_2)$,
2. reaction force $\hat{F} = F \ell_2^2/(Y I_2)$,

3. strain energy $\hat{E} = E\ell_2/(YI)$.

Equations (3.4), (3.5), (3.6), (3.17) give

$$\hat{k}_s = \beta_0 + \beta_1 \hat{x}^2 + \beta_2 \hat{x}^4 + \beta_3 \hat{x}^6, \quad (3.20)$$

where

$$\begin{aligned} \beta_0 &= 48 - \frac{576\eta_2 \hat{p}_2}{5} + \frac{3456\eta_1 \eta_2 \hat{p}_1 \hat{p}_2}{25} - \frac{20736\eta_1 \eta_2 \alpha_2^2 \hat{p}_2^3}{125}, \\ \beta_1 &= \frac{3456\eta_2}{25} - \frac{20736\eta_1 \eta_2 \hat{p}_1}{125} + \frac{36429\eta_1 \eta_2 \alpha_2^2 \hat{p}_2^2}{61}, \\ \beta_2 &= -\frac{7883\eta_1 \eta_2 \alpha_2^2 \hat{p}_2}{11}, \quad \beta_3 = \frac{30672\eta_1 \eta_2 \alpha_2^2}{107}. \end{aligned} \quad (3.21)$$

Equations (3.4), (3.5), (3.6), (3.18) give (normalized Hooke's law)

$$\hat{F} = \beta_0 \hat{x} + \beta_1 \hat{x}^3 + \beta_2 \hat{x}^5 + \beta_3 \hat{x}^7, \quad (3.22)$$

and equations (3.4), (3.5), (3.6), (3.19) give (normalized integration)

$$\hat{E} = \frac{\beta_0}{2} \hat{x}^2 + \frac{\beta_1}{4} \hat{x}^4 + \frac{\beta_2}{6} \hat{x}^6 + \frac{\beta_3}{8} \hat{x}^8. \quad (3.23)$$

3.5.8 Reduction to cubic polynomial

Reaction force

The normalized reaction force can be written in terms of a cubic polynomial

$$\hat{F} = \hat{x} \Phi(\hat{x}^2), \quad (3.24)$$

where

$$\Phi(z) = \beta_0 + \beta_1 z + \beta_2 z^2 + \beta_3 z^3, \quad z = \hat{x}^2. \quad (3.25)$$

The equilibrium points of \hat{F} are

$$q_0 = 0, \quad q_i^\pm = \pm \sqrt{z_i}, \quad i = 1, 2, 3, \quad (3.26)$$

where z_1, z_2, z_3 are the roots of the polynomial $\Phi(z)$. Note that q_i^+, q_i^- make physical sense only if z_i is real and non-negative.

Tangential stiffness

The normalized tangential stiffness is

$$\hat{k}_t = \frac{d\hat{F}}{d\hat{x}},$$

so it can be written

$$\hat{k}_t = \Xi(\hat{x}^2), \quad (3.27)$$

where

$$\Xi(z) = \beta_0 + 3\beta_1 z + 5\beta_2 z^2 + 7\beta_3 z^3, \quad z = x^2. \quad (3.28)$$

The zero stiffness positions ζ_i

$$\zeta_i^\pm = \pm\sqrt{z_i}, \quad i = 1, 2, 3, \quad (3.29)$$

where z_1, z_2, z_3 are the roots of the cubic polynomial $\Xi(z)$. Note that ζ_i^+, ζ_i^- make physical sense only if z_i is real and non-negative.

3.5.9 Roots of a cubic polynomial

The qualitative behavior of the roots of $\Phi(z)$ can be described by its discriminant [82]

$$\Delta_\Phi = 18\beta_3\beta_2\beta_1\beta_0 - 4\beta_2^3\beta_0 + \beta_2^2\beta_1^2 - 4\beta_3\beta_1^3 - 27\beta_3^2\beta_0^2. \quad (3.30)$$

If Δ_Φ is negative, then Φ has one real root, otherwise, it has three real roots. The sign of the real roots can be determined by *Descartes's rule of signs* which states that the number of positive roots of a polynomial is either equal to the number of sign differences between consecutive nonzero coefficients, or is less than it by an even number, and equality holds if all the roots are real [82, 83].

3.5.10 Evaluation of DOS

We use the basic properties of the previous section to compute the DOS, the number of minima of the strain energy E . Since E is an even degree polynomial with $E \rightarrow \infty$ as $\hat{x} \rightarrow \pm\infty$, it is easily

Table 3.1 – Evaluation of DOS

$\sigma(\Delta\Phi)$	n_σ	DOS
-	0	1
+		1
-	1	2
+		2
-	2	1
+		3
-	3	2
+		4

seen that in the generic case

$$\text{DOS} = \frac{n_q + 1}{2}. \quad (3.31)$$

where n_q is the number of equilibrium points. Let n^+ be number of the positive roots of Φ , equation (3.26) shows that $n_q = 2n^+ + 1$, so that

$$\text{DOS} = n^+ + 1. \quad (3.32)$$

We can now use the discriminant and Descarte's rules of signs to evaluate the DOS as shown in Table 3.1, where $\sigma(\Delta\Phi)$ is the sign of discriminant and n_σ is the number of sign changes of the coefficients of Φ .

3.6 Qualitative stability behavior

For fixed programming inputs \hat{p}_1, \hat{p}_2 , the qualitative stability is given by the strain energy, as shown in Figure 3.10 for different programmed DOS. Note that $\hat{x} = 0$ is always an equilibrium state, stable for odd DOS and unstable for even DOS, and the other equilibrium states are symmetric around $\hat{x} = 0$. The rest of this section characterizes qualitative behavior as the programming inputs \hat{p}_1, \hat{p}_2 vary.

Our explicit analytical computations, including the evaluation of DOS, are summarized in Figures 3.11-3.19 and pertain to the specific values $\eta_1 = 176$, $\eta_2 = 4.6$ and $\alpha_2 = 1$, see Section 3.4.2. We believe that the same qualitative behavior holds for all admissible η_1, η_2 and $\alpha_2 = 1$, see [81].

3.6.1 Computation of DOS of the T-mechanism

Our main result is the DOS as function of \hat{p}_1, \hat{p}_2 illustrated in Figure 3.11(c) for $\eta_1 = 176$, $\eta_2 = 4.6$ and $\alpha_2 = 1$.

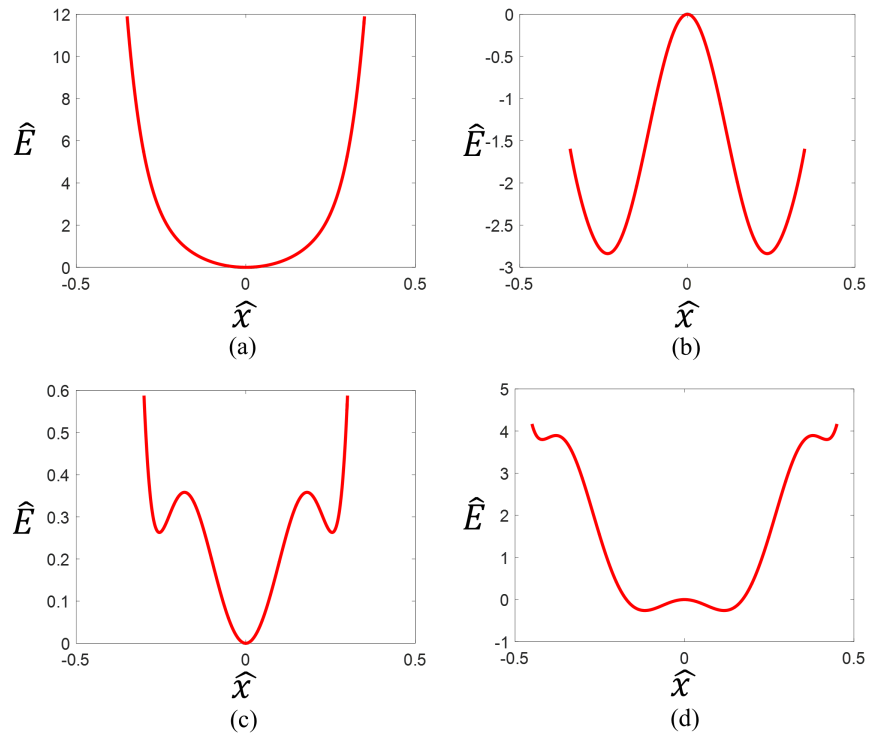


Figure 3.10 – Strain energy of the T-mechanism programmed to be (a) monostable at $\hat{p}_1 = 0, \hat{p}_2 = 0$, (b) bistable at $\hat{p}_1 = 0, \hat{p}_2 = 0.12$, (c) tristable at $\hat{p}_1 = 0.0175, \hat{p}_2 = 0$, (d) quadrastable at $\hat{p}_1 = 0.12, \hat{p}_2 = 0.0175$.

In order to derive this, we begin by considering all admissible η_1 , η_2 and $\alpha_2 = 1$. Although the DOS depends on the polynomial Φ defined in equation (3.25), we will show that it can be largely determined by β_0 , the constant term of Φ . Indeed, β_0 is the tangential stiffness at $x = 0$, the equilibrium state q_0 , and as illustrated in Figure 3.10 going from odd DOS to even DOS or vice-versa is equivalent to a change in the sign of β_0 , so roots of $\beta_0 = 0$ determine a change of DOS. The values of \hat{p}_2 for which β_0 vanishes are \hat{p}_2^a , \hat{p}_2^b , \hat{p}_2^{cr} and correspond to the buckling described in Section 3.4.1. Figure 3.13 is an example of how these values delineate regions with different DOS.

According to Sections 3.5.9 and 3.5.10, the number of real zeros of Φ is determined by the sign of its discriminant

$$\begin{aligned} \Delta_\Phi = & -5111670774.5\eta_1^2\eta_2^2 - 3029140967.2\eta_1\eta_2^4 \\ & + 10904907482.1\eta_1^2\eta_2^4\hat{p}_1 - 13085888978.5\eta_1^3\eta_2^4\hat{p}_1^2 \\ & + 5234355591.4\eta_1^4\eta_2^4\hat{p}_1^3 - 29089\eta_1^2\eta_2^3\hat{p}_2 + 34906.8\eta_1^3\eta_2^3\hat{p}_1\hat{p}_2 \\ & + 62870.5\eta_1^2\eta_2^4\hat{p}_2^2 - 150889.0\eta_1^3\eta_2^4\hat{p}_1\hat{p}_2^2 + 90533.5\eta_1^4\eta_2^4\hat{p}_1^2\hat{p}_2^2 \\ & + 75934.2\eta_1^3\eta_2^3\hat{p}_2^3 - 0.2\eta_1^3\eta_2^4\hat{p}_2^4 + 0.26\eta_1^4\eta_2^4\hat{p}_1\hat{p}_2^4 \\ & - 0.28\eta_1^4\eta_2^4\hat{p}_2^6, \end{aligned} \quad (3.33)$$

where floating point coefficients highlight approximate behavior.

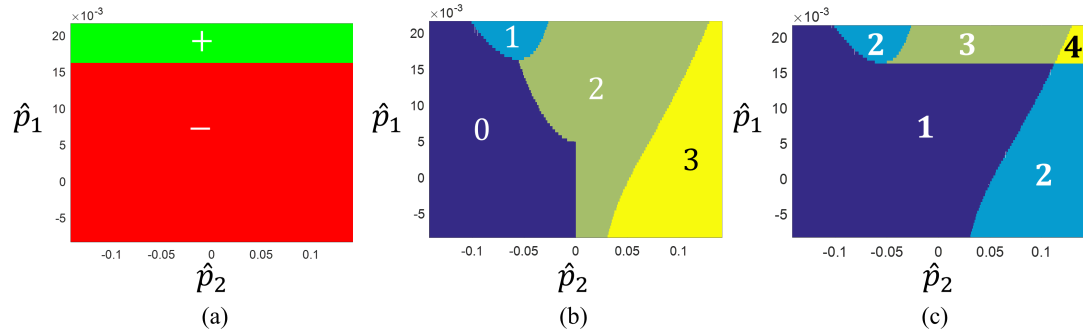


Figure 3.11 – (a) Sign of the discriminant Δ_Φ , (b) number of sign alternations n_σ , (c) DOS.

Equation (3.33) shows that only the terms *not* involving \hat{p}_2 are significant, as illustrated by Figure 3.11(a), where the positive and negative values of Δ are separated by a horizontal line at $\hat{p}_1 = \hat{p}_1^{cr}$.

To compute \hat{p}_1^{cr} , we let Δ_Φ^* be the terms of Δ_Φ not involving \hat{p}_2 and find the value \hat{p}_1^{cr} for which $\Delta_\Phi^*(\hat{p}_1^{cr}) = 0$. Dividing Δ_Φ^* by the leading coefficient of \hat{p}_1^3 gives the normalized discriminant

$$\begin{aligned} \Delta_\Phi^n = & -0.976562\eta_1^2\eta_2^2 - 0.578704\eta_1\eta_2^4 + 2.08333\eta_1^2\eta_2^4\hat{p}_1 \\ & - 2.5\eta_1^3\eta_2^4\hat{p}_1^2 + \eta_1^4\eta_2^4\hat{p}_1^3, \end{aligned} \quad (3.34)$$

where \hat{p}_1^{cr} is a root of this polynomial. We now examine β_0 and note that $\beta_0 = B(\hat{p}_2)$, where

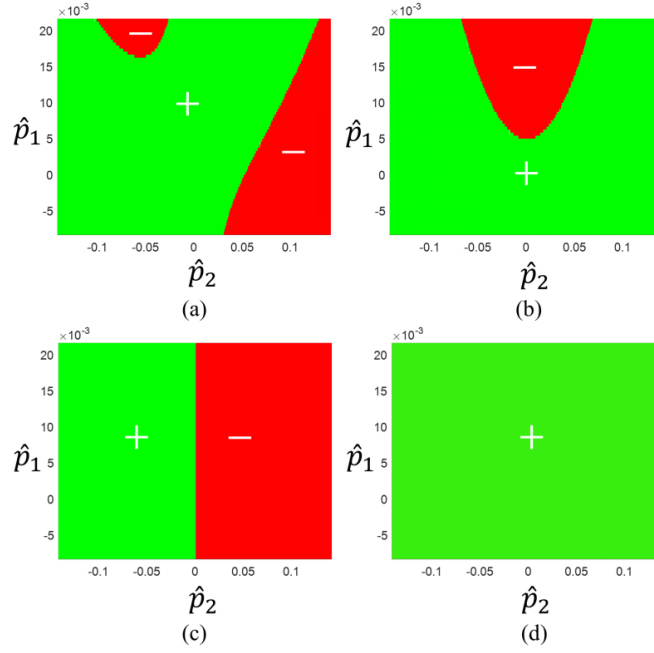


Figure 3.12 – Sign of (a) β_0 , (b) β_1 , (c) β_2 , (d) β_3 .

$B(z)$ is a polynomial with coefficients depending on p_1 . The discriminant of B is

$$\begin{aligned} \Delta_B = & -1711891286.1\eta_1^2\eta_2^2 - 1014454095.4\eta_1\eta_2^4 \\ & + 3652034743.6\eta_1^2\eta_2^4\hat{p}_1 - 4382441692.3\eta_1^3\eta_2^4\hat{p}_1^2 \\ & + 1752976676.9\eta_1^4\eta_2^4\hat{p}_1^3, \end{aligned} \quad (3.35)$$

and dividing by the leading coefficient \hat{p}_1^3 gives the normalized form

$$\begin{aligned} \Delta_B^n = & -0.976563\eta_1^2\eta_2^2 - 0.578704\eta_1\eta_2^4 + 2.08333\eta_1^2\eta_2^4\hat{p}_1 \\ & - 2.5\eta_1^3\eta_2^4\hat{p}_1^2 + \eta_1^4\eta_2^4\hat{p}_1^3. \end{aligned} \quad (3.36)$$

A comparison of Δ_Φ^n and Δ_B^n shows that they only differ in the term $\eta_1^2\eta_2^2$ by one part per million, so for admissible η_1, η_2 and the range of programming values \hat{p}_1, \hat{p}_2 , the two polynomials can be considered equal with $\Delta_\Phi = 2.98598\Delta_B$. It follows that the real root of Δ_B can be identified with \hat{p}_1^{cr} , the root of Δ_Φ . On solving $\Delta_B^n = 0$ using the exact values of β_0 given in (3.21), we get

$$\hat{p}_1^{cr} = \frac{5}{6\eta_1} + \frac{126}{127} \left(\frac{1}{2\eta_1\eta_2} \right)^{2/3}. \quad (3.37)$$

We conclude that for \hat{p}_1 fixed, Φ and β_0 have the same number of real zeros, as \hat{p}_2 varies.

The number of coefficient sign alternations of Φ , as \hat{p}_1, \hat{p}_2 vary, is computed by the signs of $\beta_0, \beta_1, \beta_2, \beta_3$ shown in Figure 3.12 and leads the number of coefficient sign alternations shown in Figure 3.11(b). Numerical inspection for our chosen values of $\eta_1 = 176, \eta_2 = 4.6$ shows that

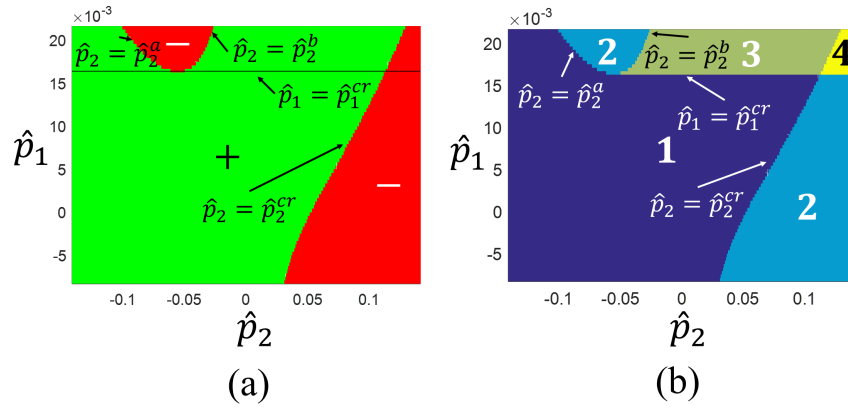


Figure 3.13 – (a) Sign and zeros of β_0 , (b) DOS with boundaries.

the regions having an equal number of sign alternations are essentially determined by the sign of β_0 , so, as expected, the boundaries between such regions correspond to zeros of β_0 as illustrated in Figure 3.13.

3.6.2 Equilibrium and zero stiffness diagrams

An equilibrium and zero stiffness diagram gives the positions of equilibrium and zero stiffness positions as one programming input is fixed and the other varies. Characteristically, these diagrams exhibit *bifurcation*, see [1] for the definition of the different types of bifurcation.

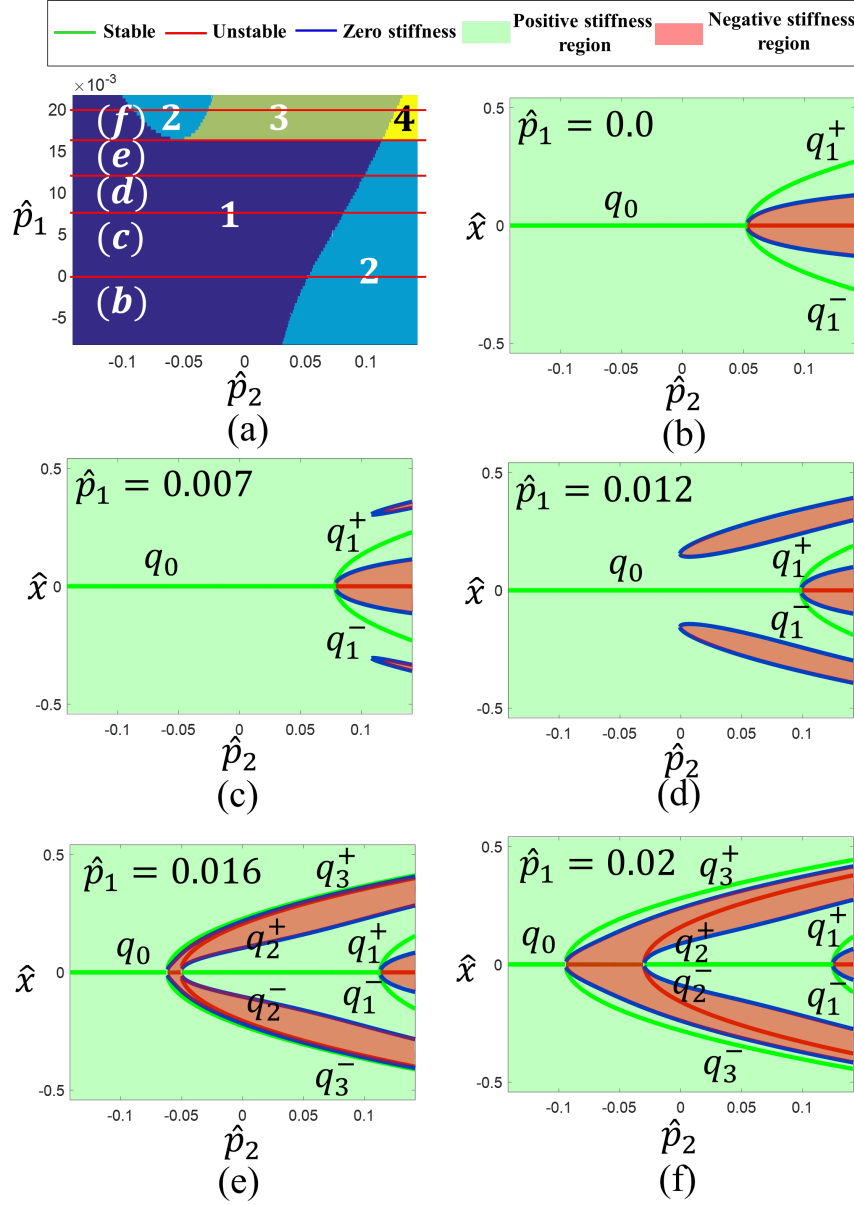


Figure 3.14 – Equilibrium and zero stiffness diagrams for the fixed values shown in (a): (b) $\hat{p}_1 = 0.0$, (c) $\hat{p}_1 = 0.007$, (d) $\hat{p}_1 = 0.012$, (e) $\hat{p}_1 = 0.016$, (f) $\hat{p}_1 = 0.02$.

Figure 3.14 gives the equilibrium and zero stiffness diagrams as function of \hat{p}_2 for five different values of \hat{p}_1 as illustrated on the programming diagram in Figure 3.14(a).

Figure 3.14(b) corresponds to $\hat{p}_1 = 0$. For $\hat{p}_2 < \hat{p}_2^{cr}$, where $\hat{p}_2^{cr} = 0.055$, the mechanism is monostable with stable position $q_0 = \hat{x} = 0$. At $\hat{p}_2 = \hat{p}_2^{cr}$, a pitch-fork bifurcation occurs. The stable position q_0 becomes unstable and bifurcates into two stable positions q_1^\pm . Also, at $\hat{p}_2 = \hat{p}_2^{cr}$, a saddle-node bifurcation occurs for zero stiffness positions.

Figure 3.14(c) corresponds to $\hat{p}_1 = 0.007$. Bifurcation of both equilibrium and zero stiffness occurs at $\hat{p}_2^{cr} = 0.08$ and four new zero stiffness states appear when $\hat{p}_2 > 0.08$.

Figure 3.14(d) corresponds to $\hat{p}_1 = 0.012$ and bifurcation occurs at $\hat{p}_2^{cr} = 0.1$. Note that as \hat{p}_1 increases with \hat{p}_2 fixed, zero stiffness positions move closer to $\hat{x} = 0$ and bifurcation occurs at a higher \hat{p}_2^{cr} .

Figure 3.14(e) corresponds to $\hat{p}_1 = 0.017$. Since $\hat{p}_1 > \hat{p}_1^{cr} = 0.016$, the zero stiffness positions merge and two pitch-fork bifurcations occur at $\hat{p}_2 = \hat{p}_2^a = -0.055$ and $\hat{p}_2 = \hat{p}_2^b = -0.045$. At $\hat{p}_2 = \hat{p}_2^a$, stable position q_0 becomes unstable and bifurcate into two stable states q_3^\pm . At $\hat{p}_2 = \hat{p}_2^b$, unstable position q_0 becomes stable and bifurcates into two unstable positions q_2^\pm . A pitch fork bifurcation occurs at $\hat{p}_2 = \hat{p}_2^{cr}$, where $\hat{p}_2^{cr} = 0.12$ and q_0 bifurcates into two unstable q_1^\pm .

Figure 3.14(f) corresponds to $\hat{p}_1 = 0.02$. This figure is qualitatively the same as Figure 3.14(e), where, for fixed \hat{p}_2 , positions q_3^\pm move apart and q_1^\pm move closer. The bifurcation positions \hat{p}_2^a and \hat{p}_2^b have moved apart.

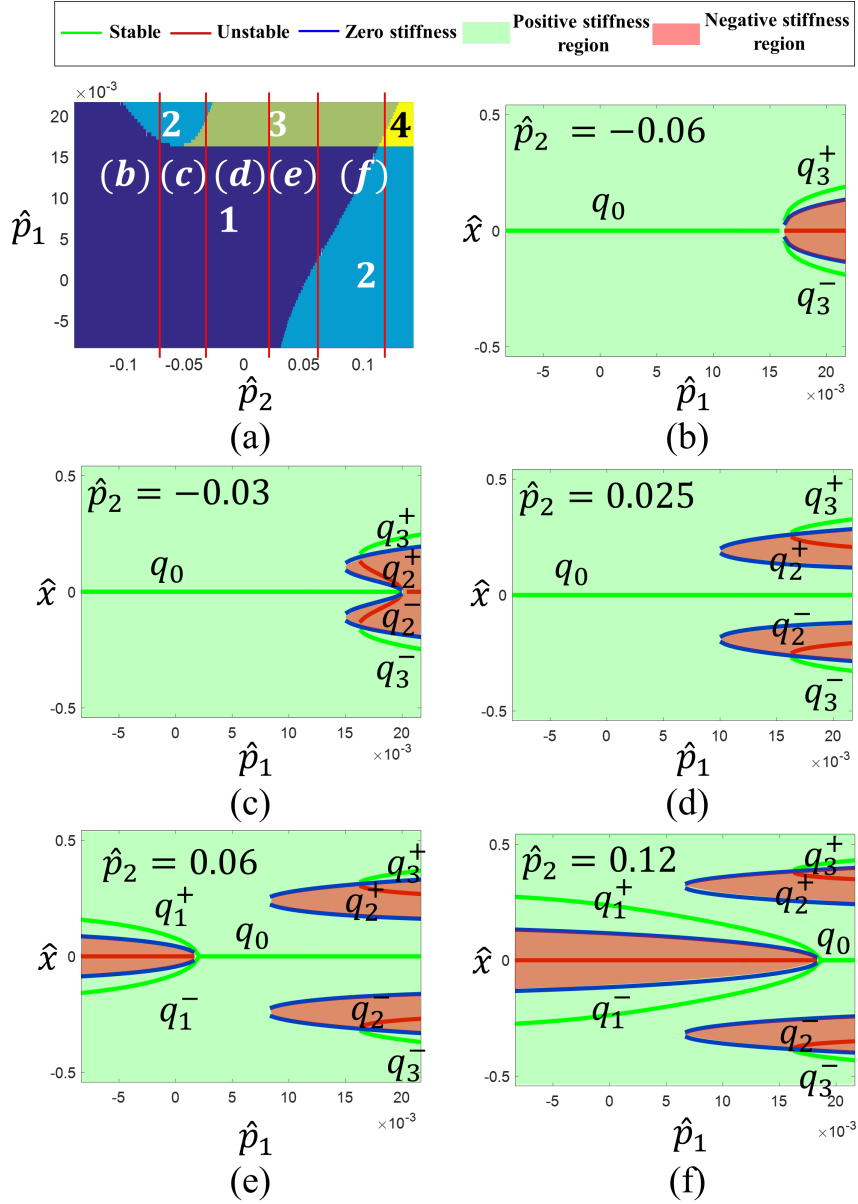


Figure 3.15 – Equilibrium and zero stiffness diagrams for the fixed values shown in (a): (b) $\hat{p}_2 = -0.06$, (c) $\hat{p}_2 = -0.03$, (d) $\hat{p}_2 = 0.025$, (e) $\hat{p}_2 = 0.06$, (f) $\hat{p}_2 = 0.12$.

Similarly, Figure 3.15 gives equilibrium and zero stiffness positions for five different values of \hat{p}_2 , as illustrated in Figure 3.15(a).

Figure 3.15(b) corresponds to $\hat{p}_2 = -0.06$. The mechanism is monostable for $\hat{p}_1 < \hat{p}_1^{cr}$ with a stable state $q_0 = \hat{x} = 0$. At $\hat{p}_1 = \hat{p}_1^{cr}$, stable position q_0 bifurcates into two stable states q_3^\pm and becomes unstable. A saddle node bifurcation occurs for the zero stiffness position at $\hat{p}_1 = \hat{p}_1^{cr}$.

Figure 3.15(c) corresponds to $\hat{p}_2 = -0.03$ with one stable position for $\hat{p}_1 < \hat{p}_1^{cr}$. A saddle node

bifurcation occurs at $\hat{p}_1 = \hat{p}_1^{cr}$, where equilibrium states q_2^\pm, q_3^\pm are created. As illustrated in Section 3.6.1, on increasing \hat{p}_1 , \hat{p}_2^b increases. When $\hat{p}_2^b = \hat{p}_2 = -0.03$, a subcritical pitch-fork bifurcation occurs, the stable state q_0 becomes unstable and bifurcates into two unstable positions q_2^\pm .

Figure 3.15(d) corresponds to $\hat{p}_2 = 0.025$. This figure is qualitatively the same as Figure 3.15(c), where, positions q_2^\pm, q_3^\pm move apart from $x = 0$.

Figure 3.15(e) corresponds to $\hat{p}_2 = 0.06$. An inverted super critical bifurcation occurs when $\hat{p}_2^{cr} = 0.06$, where stable position q_0 becomes unstable on decreasing \hat{p}_1 and bifurcates into two stable states q_1^\pm . Saddle node bifurcations occurs at $p_1 = p_1^{cr}$ where positions q_2^\pm, q_3^\pm are created.

Figure 3.15(f) corresponds to $\hat{p}_2 = 0.12$. This figure is qualitatively the same as Figure 3.15 except that the inverted super critical bifurcation occurs at \hat{p}_1 values greater than \hat{p}_1^{cr} .

Note that in Figures 3.15(c), (d), (e), (f), saddle node bifurcations of zero stiffness positions occur at lower values of \hat{p}_1 than for equilibrium positions.

3.6.3 Stiffness diagrams

Mechanism stiffness at stable and unstable states is of great importance to compliant mechanism design [4]. Using equation (3.20), we calculate the effect of the programming inputs on the stiffness of equilibrium states, recall that the sign of the stiffness determines stability.

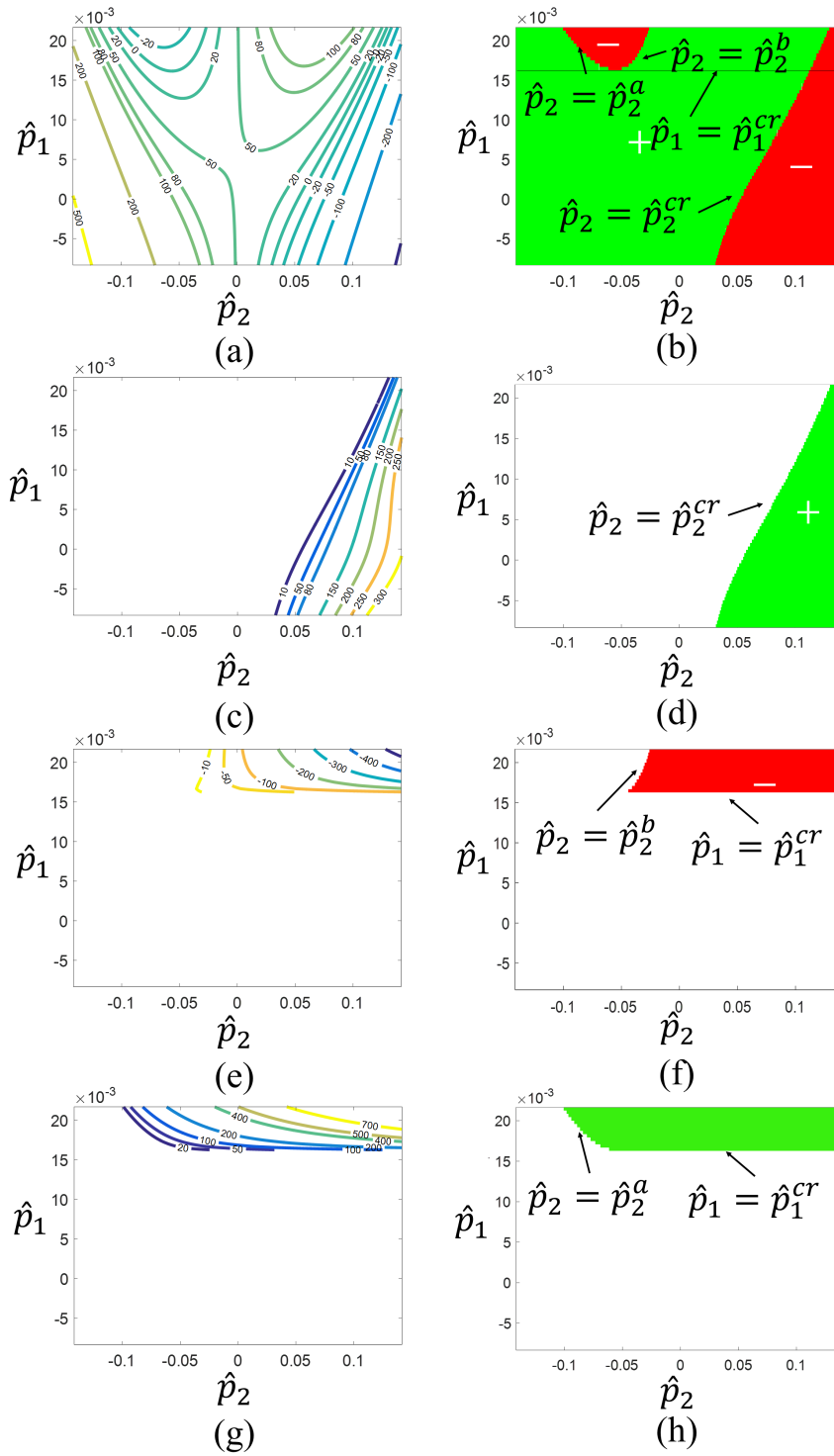


Figure 3.16 – Stiffness and sign of stiffness at equilibrium positions: (a) and (b) for q_0 , (c) and (d) for q_1 , (e) and (f) for q_2 , (g) and (h) for q_3 .

Equilibrium position q_0

The equilibrium position q_0 exists for all \hat{p}_1, \hat{p}_2 . When $\hat{p}_1 < \hat{p}_1^{cr}$, its stiffness \hat{k}_{q_0} decreases with increasing \hat{p}_2 . It is zero at $\hat{p}_2 = \hat{p}_2^{cr}$ and negative for $\hat{p}_2 > \hat{p}_2^{cr}$.

When $\hat{p}_1 > \hat{p}_1^{cr}$, the stiffness \hat{k}_{q_0} decreases with increasing \hat{p}_2 reaching zero at $\hat{p}_2 = \hat{p}_2^a$. It is negative for $\hat{p}_2^a < \hat{p}_2 < \hat{p}_2^b$, zero at $\hat{p}_2 = \hat{p}_2^b$ and negative for $\hat{p}_2 > \hat{p}_2^{cr}$. Figures 3.16 (a),(b) illustrate \hat{k}_{q_0} with respect to \hat{p}_1, \hat{p}_2 .

Equilibrium positions q_1^\pm

The equilibrium positions, q_1^+, q_1^- are symmetric around $\hat{x} = 0$ and they exist when $\hat{p}_2 > \hat{p}_2^{cr}$. Their stiffness \hat{k}_{q_1} is always positive, so they are stable. With \hat{p}_1 fixed, increasing \hat{p}_2 increases \hat{k}_{q_1} .

For \hat{p}_2 fixed, increasing \hat{p}_1 decreases \hat{k}_{q_1} . Figures 3.16 (c),(d) illustrate \hat{k}_{q_1} with respect to \hat{p}_1, \hat{p}_2 .

Equilibrium positions q_2^\pm

The equilibrium positions, q_2^+, q_2^- are unstable, symmetric around $\hat{x} = 0$ and they exist only when $\hat{p}_2 > \hat{p}_2^b$ and $\hat{p}_1 > \hat{p}_1^{cr}$. On increasing \hat{p}_2 for a given \hat{p}_1 , their stiffness \hat{k}_{q_2} decreases. Figures 3.16(e), (d) illustrate \hat{k}_{q_2} with respect to \hat{p}_1, \hat{p}_2 .

Equilibrium positions q_3^\pm

The equilibrium positions, q_3^+, q_3^- are stable, symmetric around $\hat{x} = 0$ and they exist only when $\hat{p}_2 > \hat{p}_2^a$ and $\hat{p}_1 > \hat{p}_1^{cr}$. On increasing \hat{p}_2 for a given \hat{p}_1 , their stiffness \hat{k}_{q_3} increases.

As \hat{p}_1 increases and \hat{p}_2 is fixed, the magnitude of \hat{k}_{q_3} increases. Figure 3.16(g), (f) illustrate \hat{k}_{q_3} with respect to \hat{p}_1, \hat{p}_2 .

3.6.4 Special cases

The T-mechanism exhibits near constant stiffness when the axial loads of its double parallelogram modules equal their zero stiffness loads. This leads to zero and constant force mechanisms [59].

We examine four cases with values illustrated in Figure 3.17(a). We have made FEM simulations which validate the analytical model as discussed in Section 3.7.

Zero force monostable mechanism

When $\hat{p}_1 < \hat{p}_1^{cr}$ and $\hat{p}_2 = \hat{p}_2^{cr}$, the T-mechanism switches from monostability to bistability. The axial load of module 2 is equals its zero stiffness load [6]. The T-mechanism has a near zero reaction force in the range $-0.07 < \hat{x} < 0.07$ for $\hat{p}_1 = 0.0$, $\hat{p}_2 = 0.052$, as illustrated in Figure 3.17(b).

Constant force monostable mechanism

When the axial load on module 1 equals its zero stiffness load and $\hat{p}_2 < \hat{p}_2^a$, the mechanism is monostable and has regions of near constant force. Figure 3.17(c) illustrates the reaction force of the mechanism when $\hat{p}_1 = 0.012$, $\hat{p}_2 = 0$ with constant force range $-0.18 < \hat{x} < -0.13$ and $0.13 < \hat{x} < 0.18$, with $\hat{F} = -4.2$ and 4.2 , respectively.

Zero force bistable mechanism

When $\hat{p}_2 = \hat{p}_2^b$ and $\hat{p}_1 > \hat{p}_1^{cr}$, the mechanism switches from bistability to tristability. The axial load of module 2 equals its zero stiffness load and the mechanism has near zero reaction force at $\hat{x} = 0$ leading to a zero force bistable mechanism. Figure 3.17(d) illustrates the reaction force of the mechanism at $\hat{p}_1 = 0.017$, $\hat{p}_2 = -0.045$, where the zero force range is $-0.03 < \hat{x} < 0.03$.

Constant force bistable mechanism

When $\hat{p}_2 > \hat{p}_2^{cr}$ and $\hat{p}_1 < \hat{p}_1^{cr}$, the mechanism is bistable. When the axial load of module 1 equals its zero stiffness load, the mechanism has near constant force behavior. Figure 3.17(e) illustrates the reaction force of the mechanism at $\hat{p}_1 = 0.007$, $\hat{p}_2 = 0.092$, where the constant force ranges are $-0.31 < \hat{x} < -0.22$ and $0.22 < \hat{x} < 0.31$, with $\hat{F} = -0.13$ and 0.13 , respectively.

Zero force tristable mechanism

When $\hat{p}_1 > \hat{p}_1^{cr}$ and $\hat{p}_2 = \hat{p}_2^{cr}$, the mechanism switches from tristability to quadrastability. The axial load of module 2 equals its zero stiffness load. The mechanism has zero force behavior around $\hat{x} = 0$. Figure 3.17(f) illustrates the reaction force of the mechanism at $\hat{p}_1 = 0.017$, $\hat{p}_2 = 0.12$ with zero force range $-0.03 < \hat{x} < 0.03$.

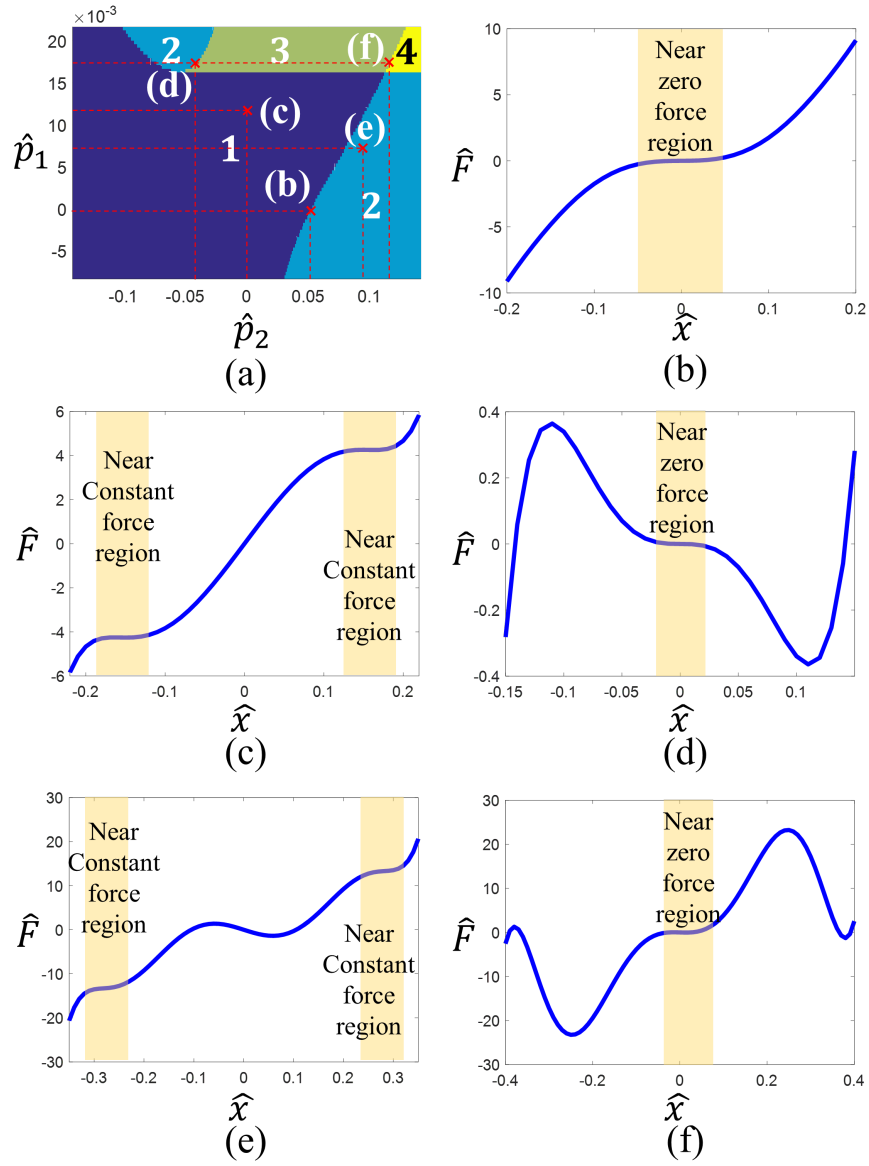


Figure 3.17 – (a) Selected values of \hat{p}_1, \hat{p}_2 leading to near zero force and near constant force regions: (b) zero force monostable mechanism at $\hat{p}_1 = 0, \hat{p}_2 = 0.052$, (c) constant force monostable mechanism at $\hat{p}_1 = 0.012, \hat{p}_2 = 0$, (d) zero force bistable mechanism at $\hat{p}_1 = 0.017, \hat{p}_2 = -0.045$, (e) constant force bistable mechanism at $\hat{p}_1 = 0.007, \hat{p}_2 = 0.092$, (f) zero force tristable mechanism at $\hat{p}_1 = 0.017, \hat{p}_2 = 0.12$.

3.6.5 DOS sensitivity

As demonstrated in Section 6.1, qualitative behavior is determined by the zeros of β_0 , and this parameter is a polynomial in \hat{p}_1 , \hat{p}_2 , as given by equation (3.21) of Section 5.7, and is linear in \hat{p}_1 and cubic in \hat{p}_2 . This gives smooth dependence on \hat{p}_1 , \hat{p}_2 except at bifurcation points, i.e., DOS is locally constant.

Sensitivity to \hat{p}_1 , \hat{p}_2 holds for the DOS at bifurcation points, since \hat{p}_1 , \hat{p}_2 change continuously while the DOS is a discrete number. More generally, sensitivity of DOS at bifurcation is intrinsic to programmable multistable mechanisms since a discrete change occurs by continuous actuation [6].

Our model gives explicit formulas for bifurcation as function of programming input. Section 6.1 shows that bifurcation in \hat{p}_1 occurs at \hat{p}_1^{cr} given by equation (4.15) and for \hat{p}_2 at zeros of β_0 at \hat{p}_2^a , \hat{p}_2^b , \hat{p}_2^{cr} .

3.7 Numerical validation

COMSOL FEM was used to model the stability behavior of the 2-DOP T-mechanism. Geometric nonlinearity was implemented by the solid mechanics module. Mesh convergence tests were performed to ensure the validity of solutions. Figure 3.18 illustrates the deformation of the mechanism for $\hat{p}_1 = 0.0$, $\hat{p}_2 = 0.12$.

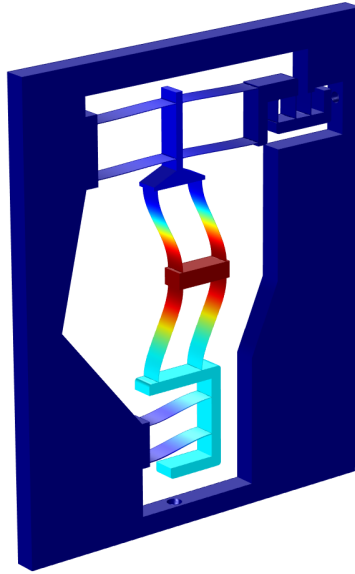


Figure 3.18 – FEM rendering of T-mechanism deformation.

Figure 3.19 gives the reaction force for monostable, bistable, tristable and quadrastable configurations, calculated analytically and numerically. This data indicates that, for small \hat{x} , there is

a good match between our analytical calculations and numerical simulations.

The discrepancy between the analytical and numerical models can reach 20%, as illustrated in Figure 3.19(f). This is explained by having neglected the higher order nonlinear terms given in [84].

However, the analytical and numerical curves are qualitatively similar validating our qualitative analysis of stability behavior.

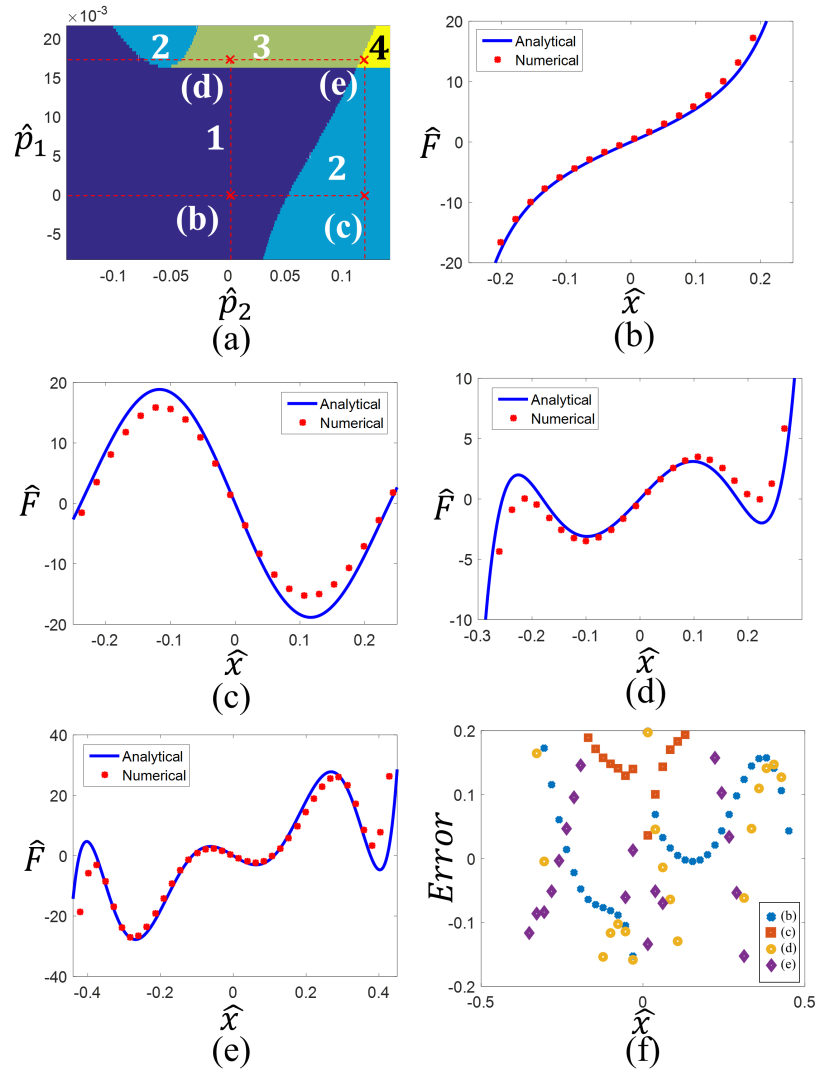


Figure 3.19 – (a) Values of \hat{p}_1 , \hat{p}_2 for FEM simulation with T-mechanism programmed to be (b) monostable at $\hat{p}_1 = 0$, $\hat{p}_2 = 0$, (c) bistable at $\hat{p}_1 = 0$, $\hat{p}_2 = 0.12$, (d) tristable at $\hat{p}_1 = 0.0175$, $\hat{p}_2 = 0$, (e) quadrastable at $\hat{p}_1 = 0.0175$, $\hat{p}_2 = 0.012$, (f) percent difference between analytical and numerical models.

3.8 Applications

We give a brief overview of applications of programmable multistable mechanisms.

1. Multistable mechanisms have been applied to computation. Logical operations were implemented using bistable mechanisms in [85]. Micromechanical computation devices have advantages over electronic circuits for low speed computations [86]. We conjecture that by using higher DOS, it is possible to realize a Turing complete mechanical computer. This is the subject of our current research.
2. Threshold sensors have multiple stable states and they switch between them when sensing input exceeds threshold values, they have been used as acceleration, position and shock threshold sensors [6, 21]. Stability programming extends the threshold sensing concept to programmable sensors, where the number and the value of the threshold states is modifiable.
3. This paper provides a new method for connecting bistable mechanisms to build programmable mechanical meta-materials [87], where the effective value of Young's modulus, the Poisson ratio, and stable configurations can be controlled and stiffness estimated by our analytic model.
4. Puncturing human tissue is required during surgery and necessitates great precision to avoid large forces causing irreversible damage. Stability programming provides control over puncturing force and stroke as we demonstrated in previous work [88].

3.9 Conclusion

We introduced the concept of stability programming and provided a novel analytic model of T-connected 2 degree of programming mechanisms yielding explicit expression for degree of stability, the position and stiffness of equilibrium states as well as estimates for constant force regimes. Our analysis was validated using FEM simulation.

In chapter 4, I present the experimental validation of our analysis. In chapter 5 and chapter 6, the application of PMMs to horological escapements and medical devices is given.

4 Experimental Characterization *

4.1 Introduction

The main goals of this chapter are

1. Experimental validation of the concept of stability programming
2. Experimental characterization of the stability behavior of the T-mechanism, a generic example of programmable multistable mechanism discussed in Chapter 3 [89].
3. Extension of the analytical model in Chapter 3 to parallelogram mechanism having rectangular hinges.

The chapter is arranged as follows. First, we extend our analytical model to the T-combined double parallelogram mechanisms (DPM) consisting of rectangular beam hinges. A prototype of the T-mechanism is manufactured using electro-discharge machining (*EDM*). Then, we discuss the measurement setup and the results, as compared to our analytical and numerical calculations.

4.2 Programmable multistable T-mechanism

A T-combined DPM consists of two modules orthogonally connected. Each module is an axially loaded DPM with two parallel beams centrally connected by a rigid block, as illustrated in Figure 4.1(a). Module 1 is fixed on one extremity and axially guided by programming input p_1 on the other extremity. Module 2 is connected to the central block of module 1 in the lateral direction of the beams of module 1 on one extremity. The other extremity of module 2 is guided by programming input p_2 . An actuation input x is applied to the central block of module 2 in the lateral direction of its beams.

*The content of this chapter has been published as Mohamed Zanaty, and Simon Henein. "Experimental Characterization of a T-shaped Programmable Multistable Mechanism." *Journal of Mechanical Design* 140, no. 9 (2018): 092301.

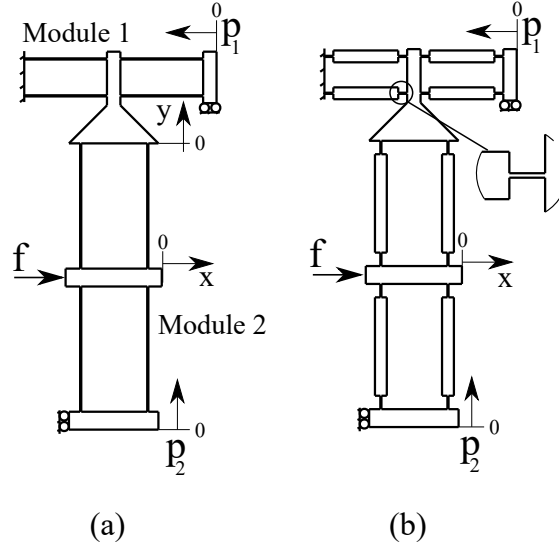


Figure 4.1 – 2-DOP T-combined double parallelogram mechanisms composed of (a) distributed stiffness blades, (b) lumped stiffness rectangular hinges.

As discussed in Chapter 3, the stability behavior of the mechanism depends on the values of p_1 and p_2 . We define p_1^{cr} as the minimum value of p_1 at which module 1 buckles with sufficient lateral force to buckle module 2. Similarly, p_2^c is the minimum value of p_2 at which the lateral stiffness of module 2 is zero at $x = 0$.

Table 4.1 summarizes the range of the programming inputs for a given DOS. It should be noted that

1. The values of p_2^a , p_2^b , p_2^c depend on p_1 .
2. The value of p_1^{cr} depends only on the dimensions of the mechanism.

The concept of stability programming of T-mechanism is still valid for different geometrical variants of parallelogram mechanisms, in which distributed stiffness blades is replaced by rectangular beam hinges, as given in Figure 4.1(b).

In this Chapter, we study T-combined DPM with rectangular beam hinges. They are simpler to manufacture using EDM, compared to distributed stiffness blades discussed in our previous paper [89], and have a relatively longer stroke compared to circular notch hinges [90]. In the rest of this Chapter, we will refer to the T-combined DPM with rectangular hinges as *T-mechanism*, for short.

Figure 4.2 illustrates a T-mechanism with width w . Module 1 has four beams of length ℓ_1 with rigid links of length r_1 and compliant rectangular hinges of length c_1 and thickness t_1 . Module 1 is axially loaded by a spring, referred to as *programming spring*, of stiffness k_r with length ℓ_r and thickness t_r . Module 2 has four beams of length ℓ_2 with rigid links of length r_2

4.2. Programmable multistable T-mechanism

Table 4.1 – DOS of the T-mechanism as a function of the programming inputs, p_1 , p_2 .

p_1	p_2	DOS
$p_1 < p_1^{cr}$	$p_2 < p_2^c$	1
$p_1 > p_1^{cr}$	$p_2 < p_2^a$	1
$p_1 < p_1^{cr}$	$p_2 > p_2^c$	2
$p_1 > p_1^{cr}$	$p_2^a < p_2 < p_2^b$	2
$p_1 > p_1^{cr}$	$p_2^b < p_2 < p_2^c$	3
$p_1 > p_1^{cr}$	$p_2 > p_2^c$	4

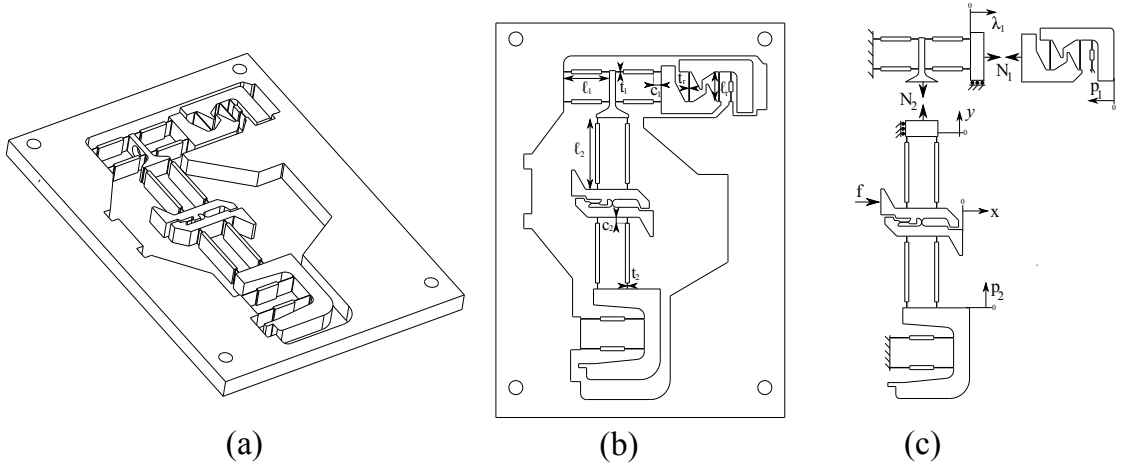


Figure 4.2 – (a) T-shaped mechanism, (b) key dimensions, (c) forces and displacements.

and rectangular hinges of length c_2 and thickness t_2 . The thickness of the rigid links is ten times that of the hinges.

We replaced the central rigid block of module 2 by two rigid blocks connected by two blades, as shown in Figure 4.2, to avoid kinematic over constraints, as illustrated by the equivalent rigid body diagram of the mechanism in Figure 4.3. This modification does not affect the stability behavior of the mechanism. There are three degrees of freedom controlled by programming inputs, p_1 , p_2 , and actuation input, x .

As illustrated in Chapter 2 [89], the stability behavior of the T-mechanism depends on the stiffness ratio of module 1 to module 2, η_2 , stiffness ratio of the programming spring to module 1, η_1 , and length ratio of the beams of module 2 to module 1, α_2 , such that

$$\eta_1 = \frac{I_r \ell_1^3}{I_1 \ell_r^3}, \quad \eta_2 = \frac{I_1 \ell_2^3}{I_2 \ell_1^3}, \quad \alpha_2 = \frac{\ell_2}{\ell_1}. \quad (4.1)$$

We introduce the parameters a_{01} , a_{02} which denote the ratio of the length of rectangular

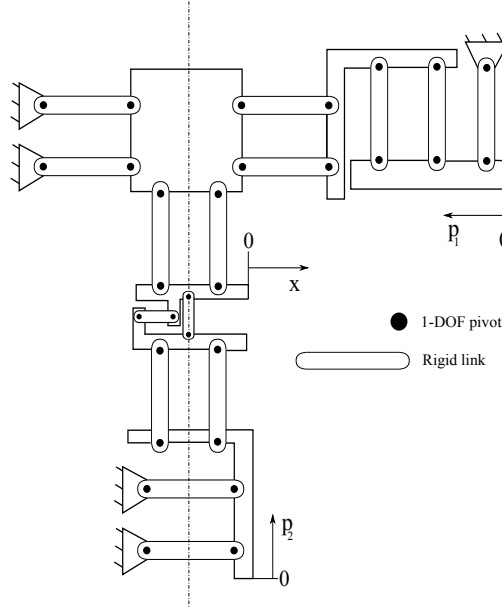


Figure 4.3 – Equivalent rigid body diagram of the T-mechanism.

hinges to the beam length of module 1 and module 2, respectively.

$$a_{01} = \frac{c_1}{\ell_1}, \quad a_{02} = \frac{c_2}{\ell_2}. \quad (4.2)$$

4.3 Analytical model

We calculate the reaction force f of the mechanism upon applying a displacement x . The reaction force is represented as seventh order polynomial from which the stability behavior of the mechanism can be quantified, i.e., DOS, positions of equilibrium states and their stiffness. Our model is based on the same assumptions of Chapter 3.

1. A linear elastic material is used with Young's modulus Y .
2. The shear strain of compliant elements is negligible such that Euler-Bernoulli equations can be applied.
3. Compliant elements are not buckled in their second or higher order buckling modes.
4. Lateral forces of module 1 and module 2 are negligible compared to the buckling load of the beams of the programming spring.
5. The displacement range of the mechanism is within its intermediate range [91].

We normalize all forces of module 2 by $Y w t_2^3 / (12 \ell_2^2)$ and displacements of module 2 by ℓ_2 . Similarly, the forces of module 1 are normalized by $Y w t_1^3 / (12 \ell_1^2)$ and displacements by ℓ_1 .

Following the same procedure discussed in Chapter 3, we derived the reaction force of the T-mechanism having rectangular hinges as a seventh order polynomial. We first evaluate the relation between displacement x and axial displacements λ_1 and λ_2 of module 1 and module 2, respectively, as illustrated in Figure 4.2(c). Then, we calculate the axial loads N_1 and N_2 as functions of x . As discussed in [90], the secant stiffness of module 2 depends on N_2 . Based on that, the reaction force of module 2 which represents the reaction force of the mechanism is calculated.

On applying lateral displacement x to the central block of module 2, axial displacement λ_2 occurs [91, 89]

$$\lambda_2 = p_2 - \frac{6\Psi_2}{5}x^2, \quad (4.3)$$

where,

$$\Psi_2 = \frac{15 - 50a_{02} + 60a_{02}^2 - 24a_{02}^3}{2(3 - 6a_{02} + 4a_{02}^2)^2},$$

ignoring the elastic component of the axial displacement of the compliant beams.

The two modules are orthogonally connected, such that the axial displacement of module 2 is equivalent to the lateral displacement of module 1, leading to the following axial displacement of module 1 [91, 89]:

$$\lambda_1 = -\frac{6\alpha_2^2\Psi_1}{5}\lambda_2^2, \quad (4.4)$$

where,

$$\Psi_1 = \frac{15 - 50a_{01} + 60a_{01}^2 - 24a_{01}^3}{2(3 - 6a_{01} + 4a_{01}^2)^2}.$$

Substituting equation (4.3) in equation (4.4),

$$\lambda_1 = -\frac{6\alpha_2^2\Psi_1 p_2^2}{5} + \frac{72\alpha_2^2\Psi_1 \Psi_2 p_2}{25}x^2 - \frac{216\alpha_2^2\Psi_1 \Psi_2^2}{125}x^4. \quad (4.5)$$

Axial displacement λ_1 loads the programming spring imposing an axial load N_1 on module 1 [89, 90]

$$N_1 = 24\eta_1(p_1 + \lambda_1), \quad (4.6)$$

which modifies secant lateral stiffness of module 1 such that [89, 91]

$$k_s^{p1} = \frac{48}{\Gamma_1} - \frac{12}{5}\Psi_1 N_1, \quad (4.7)$$

Chapter 4. Experimental Characterization

where,

$$\Gamma_1 = \frac{1}{2a_{01}(3 - 6a_{01} + 4a_{01}^2)}.$$

Since module 1 is laterally displaced by λ_2 , it imposes an axial load on module 2 [91]

$$N_2 = \eta_2 k_s^{p1} \lambda_2. \quad (4.8)$$

The lateral reaction force of module 2 is [91, 89]

$$f = \left(\frac{48}{\Gamma_2} - \frac{12}{5} \Psi_2 N_2 \right) x, \quad (4.9)$$

where,

$$\Gamma_2 = \frac{1}{2a_{02}(3 - 6a_{02} + 4a_{02}^2)}. \quad (4.10)$$

Substituting equations (4.5), (4.6), (4.7), (4.8) in equation (4.9), the reaction force f of the mechanism can be written as seventh order polynomial

$$f = x\Phi(x^2), \quad (4.11)$$

where,

$$\Phi(z) = \beta_0 + \beta_1 z + \beta_2 z^2 + \beta_3 z^3, \quad (4.12)$$

and,

$$\begin{aligned} \beta_0 &= \frac{48}{\Gamma_2} - \frac{576\eta_2\Psi_2}{5\Gamma_1} p_2 + \frac{3456\eta_1\eta_2\Psi_1\Psi_2}{25} p_1 p_2, \\ &\quad - \frac{20736\eta_1\eta_2\Psi_1^2\Psi_2\alpha_2^2}{125} p_2^3, \\ \beta_1 &= \frac{3456\eta_2\Psi_2^2}{25\Gamma_1} - \frac{20736\eta_1\eta_2\Psi_1\Psi_2^2}{125} p_1 \\ &\quad + \frac{373248\alpha_2^2\eta_1\eta_2\Psi_1^2\Psi_2^2}{625} p_2^2, \\ \beta_2 &= \frac{-2239488\alpha_2^2\eta_1\eta_2\Psi_1^2\Psi_2^3}{3125} p_2, \\ \beta_3 &= \frac{4478976\alpha_2^2\eta_1\eta_2\Psi_1^2\Psi_2^4}{15625}. \end{aligned} \quad (4.13)$$

The stability behavior of the mechanism can be extracted from the polynomial $\Phi(z)$ [89], where

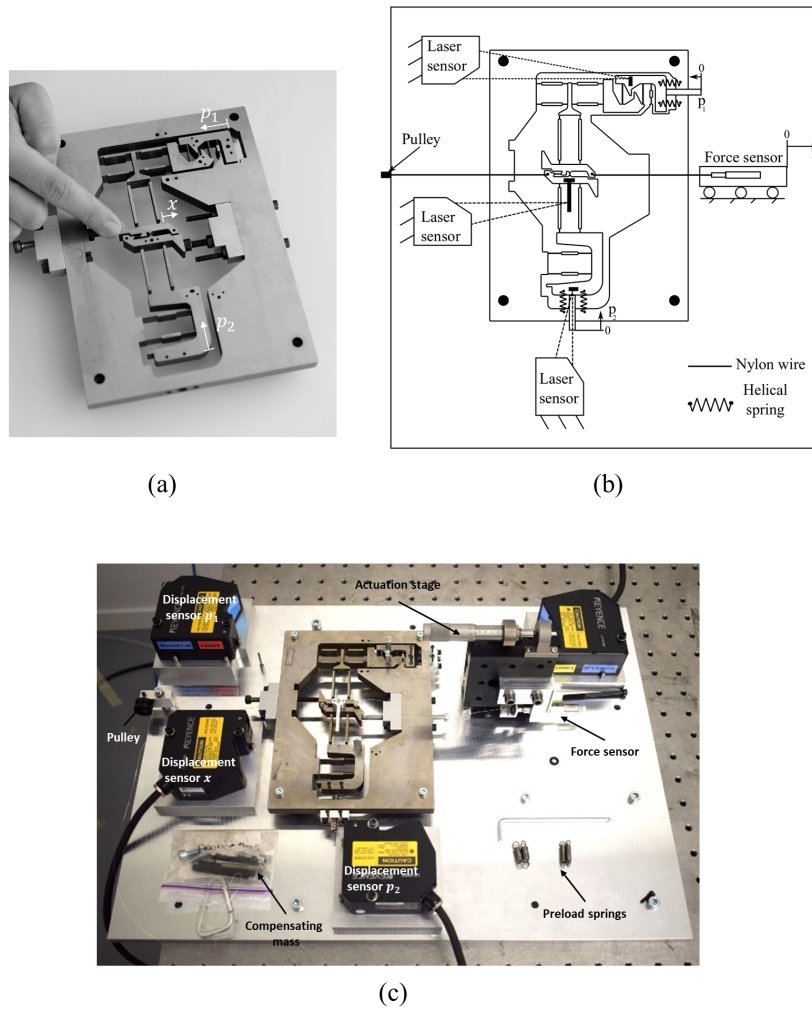


Figure 4.4 – (a) T-shaped mechanism monolithically manufactured by EDM, (b) schematic representation of the measurement setup, (c) realization of the measurement setup.

1. DOS is estimated by calculating the sign alternation of the coefficients of $\Phi(z)$ and the sign of its discriminant for given p_1, p_2 .
2. Equilibrium positions, q_i , are the square root of the positive-valued zeros of $\Phi(z)$.

$$q_0 = 0, \quad q_i^\pm = \pm\sqrt{z_i}, \quad i = 1, 2, 3. \quad (4.14)$$

3. The value of the critical buckling load p_1^{cr} is the zero of the discriminant of β_0 where [89]

$$p_1^{cr} = \frac{5}{6\Gamma_1\eta_1\eta_2} + \frac{126}{127} \left(\frac{\alpha_2^2}{\eta_1^2\eta_2^2\Gamma_2^2\Psi_1\Psi_2^2} \right)^{1/3}. \quad (4.15)$$

4. The values of p_2^a, p_2^b and p_2^c are the zeros of the cubic polynomial, β_0 , where $p_2^a < p_2^b < p_2^c$.
5. The tangential stiffness of the mechanism at its equilibrium states, q_i , is the first derivative of the reaction force with respect to the displacement x at equilibrium positions.

$$k^t = \left. \frac{\partial f}{\partial x} \right|_{x=q_i}. \quad (4.16)$$

Table 4.2 – Dimensions of the T-mechanism

Dimension	Description	Designed	Measured
w	Beam Width	10 [mm]	10[mm]
Programming spring			
ℓ_r	Beam length	15[mm]	15[mm]
t_r	Beam thickness	350[μ m]	345[μ m]
Module 1			
ℓ_1	Beam length	23[mm]	23[mm]
t_1	Hinge thickness	80[μ m]	78[μ m]
c_1	Hinge length	4.0[mm]	3.9[mm]
Module 2			
ℓ_2	Beam length	36[mm]	36[mm]
t_2	Hinge thickness	50[μ m]	49[μ m]
c_2	Hinge length	3[mm]	2.9[mm]

4.4 Numerical simulations

We use COMSOL FEM to model the stability behavior of the mechanism and calculate its reaction force and strain energy for different values p_1, p_2 . The solid mechanics module is used, including the geometric nonlinearity. The displacement control method is utilized, as it is easier to converge, being a single-valued problem. The actuation displacement x applied at

the central block of module 2 is swept and the reaction force is evaluated. The strain energy of the mechanism is estimated by integrating the stored energy density over the volume of the mechanism. Mesh convergence tests are performed to ensure the validity of the solution.

4.5 Fabrication

The T-mechanism was manufactured out of BOHLER K390 steel [92] using EDM, as shown in Figure 4.4(a). EDM is used to manufacture compliant elements of maximum length to thickness ratio of 60 [90]. We selected the dimensions of the T-mechanism in Table 4.2 such that monostability, bistability, tristability and quadrastability can be experimentally verified based on the dimensional analysis in [89]. We used Leica M125 [93] stereoscope for dimension measurements with a resolution down to 50[nm]. The inherent tolerance in the EDM technique leads to differences between designed and measured dimensions as given in Table 4.2.

4.6 Experimental setup

We constructed an experimental measurement setup that consists of three displacement Keyence laser sensors, LK-H082 [94], to measure the imposed values of p_1 , p_2 and x . Aluminum reflecting blocks are mounted on the mechanism as references planes for the sensors as illustrated in Figures 4.4(b), (c). Displacement sensors used for measuring p_1 , p_2 are configured to the range $\pm 2[mm]$ with a resolution of 25[nm]. The actuation displacement sensor is configured to measure the range of $\pm 16[mm]$ with a resolution of 100[nm].

We apply manually the programming inputs via micro-metric screws, while helical springs are used to apply negative values of the programming inputs. The actuation input is applied via a 1-DOF micro-metric stage on which piezo-electric Kistler force sensor, type 9207, is mounted [95]. The sensor is connected to the central block of module 2 via a nylon wire. The force sensor is configured for the range of $\pm 5[N]$ with a resolution of 1[mN]. A known mass is used to compensate for the negative reaction force of the mechanism to avoid snapping. The mass is connected to the central block of module 2 via a wire and pulley. All the sensors are calibrated before the measurement.

We use national instrument cRIO 9035 [96] for the control of the measurement setup and data acquisition. Analog to digital converter NI9220 [97] and charge amplifier Kistler 5171A4 [98] are used for the interface of displacement and force sensors, respectively. A graphical user interface is built for the display of the measurements and reaction force calculation.

4.7 Results and discussion

The dimensional variability of the manufacturing process and the measurements errors are accounted for by using a constant correction factor. This factor is determined by curve fitting the reaction force, as calculated using the analytical model with experimental measurements, when the mechanism is programmed as monostable.

In this section, we use the symbols p_1 , p_2 , x , f to denote the explicit values of the programming inputs of module 1, module 2, actuation input and reaction force respectively instead of representing their normalized values. We present and discuss the results according to the different stability regions of the T-mechanism introduced in [89].

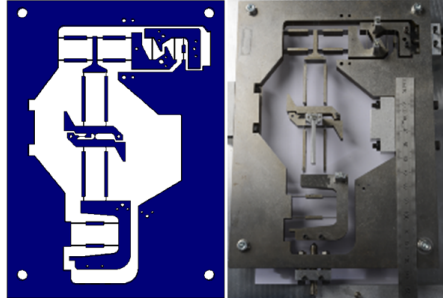


Figure 4.5 – Stable state q_0 of the mechanism programmed in monostable region based on FEM (left) and experiment (right).

4.7.1 Monostable region

The mechanism has only one stable state, i.e., $DOS = 1$ when $p_1 < p_1^{cr}$ and $p_2 < p_2^c$ or $p_1 > p_1^{cr}$ and $p_2 < p_2^a$. Figure 4.5 gives the stable state of the mechanism, q_0 , which occurs at $x = 0$. The reaction force of the mechanism is depicted in Figure 4.6 based on the analytical calculations, numerical simulations and experimental measurements showing a good match.

Upon increasing either p_1 for given p_2 or p_2 for given p_1 , the mechanism stiffness at its stable state decreases until it reaches zero at $p_2 = p_2^a$ for $p_1 > p_1^{cr}$ or $p_2 = p_2^c$ for $p_1 < p_1^{cr}$.

4.7.2 Bistable region

There are two regions in which the mechanism distinctly exhibits bistability.

Region I

This region is defined when $p_1 < p_1^{cr}$ and $p_2 > p_2^c$, where module 2 buckles. Figure 4.7 gives the equilibrium states based on numerical simulations and experimental stable states where q_1^\pm are stable states and q_0 is unstable state.

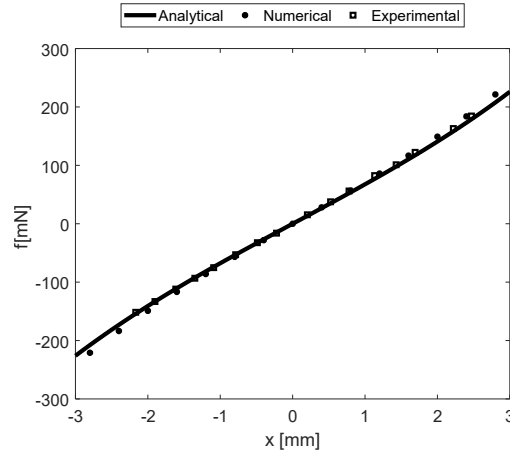


Figure 4.6 – The reaction force of the mechanism when programmed as monostable for $p_1 = 0.0[mm]$ and $p_2 = 0.0[mm]$.

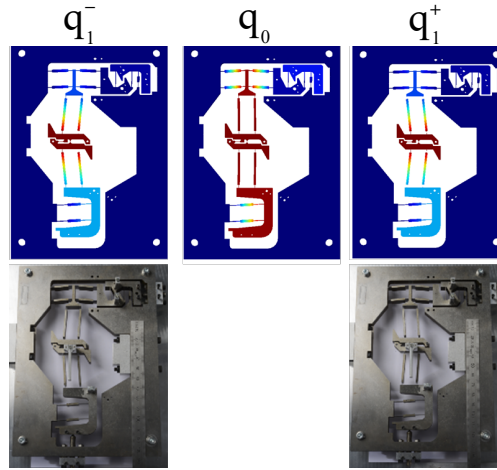


Figure 4.7 – Stable states, q_1^\pm and unstable state, q_0 of the mechanism programmed in bistable region I based on FEM (top) and experiment (bottom).

As p_1 increases for a given p_2 , the stiffness of the mechanism at its equilibrium position decreases till it reaches zero at $p_2^c = p_2$. However, the stiffness increases by increasing p_2 for a given p_1 . Figure 4.8 illustrates the reaction force of the T-mechanism at $p_1 = -0.15[mm]$, $p_2 = 1.1[mm]$.

Region II

This region is defined by $p_1 > p_1^{cr}$ and $p_2^a < p_2 < p_2^b$. The mechanism has unstable state q_0 at $x = 0$. Figure 4.9 illustrates the equilibrium states of the mechanism based on numerical simulations and the equivalent experimental stable states, where q_3^\pm are stable and q_0 is unstable. Figure 4.10 shows the reaction force of the mechanism for $p_1 = 0.39[mm]$ and $p_2 = -0.9[mm]$.

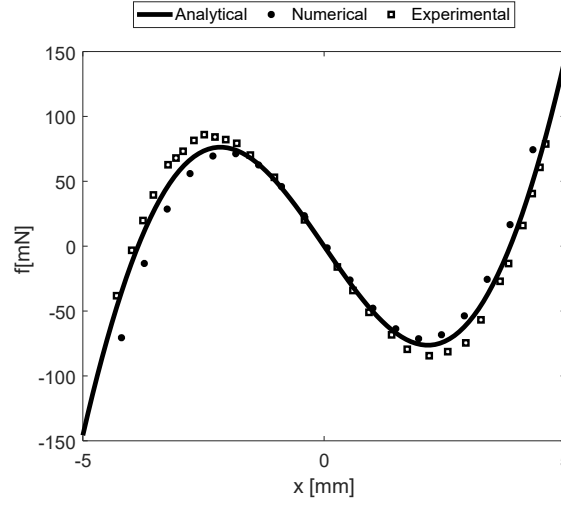


Figure 4.8 – The reaction force of the mechanism programmed as bistable in region I for $p_1 = -0.15[mm]$, $p_2 = 1.1[mm]$.

The mechanism exhibits lower stiffness magnitude around its unstable state, compared to its stable states. As p_2 increases for a given p_1 , the stiffness of the mechanism increases around its stable states q_3^\pm , however, the stiffness magnitude around q_0 may increase or decrease, depending on the range of the applied p_2 . In the case of p_1 increase for a given p_2 , the stiffness magnitude for both stable states q_3^\pm and unstable state q_0 increases.

4.7.3 Tristable region

The mechanism exhibits tristability when $p_1 > p_1^{cr}$ and $p_2^b < p_2 < p_2^c$. Figure 4.11 gives the equilibrium states of the mechanism based on numerical simulations and their equivalent experimental stable states where q_0 , q_3^\pm are stable and q_2^\pm are unstable. The reaction force of the mechanism for $p_1 = 0.36[mm]$, $p_2 = 2.8[mm]$ for imposed displacement x is given in Figure 4.12.

As p_1 increases for a given p_2 , the stiffness of equilibrium states, q_0 , q_2^\pm , q_3^\pm increases. On increasing p_2 for a given p_1 , the stiffness of stable states q_3^\pm and unstable states q_2^\pm increases while the stiffness of the stable state q_0 may increase or decrease depending on p_2 .

4.7.4 Quadrastable region

The mechanism exhibits quadrastability when $p_1 > p_1^{cr}$ and $p_2 > p_2^c$. Figure 4.13 illustrates the seven equilibrium states of the mechanism, based on numerical simulations and the equivalent experimental stable states where q_0 , q_2^\pm are unstable and q_1^\pm , q_3^\pm are stable.

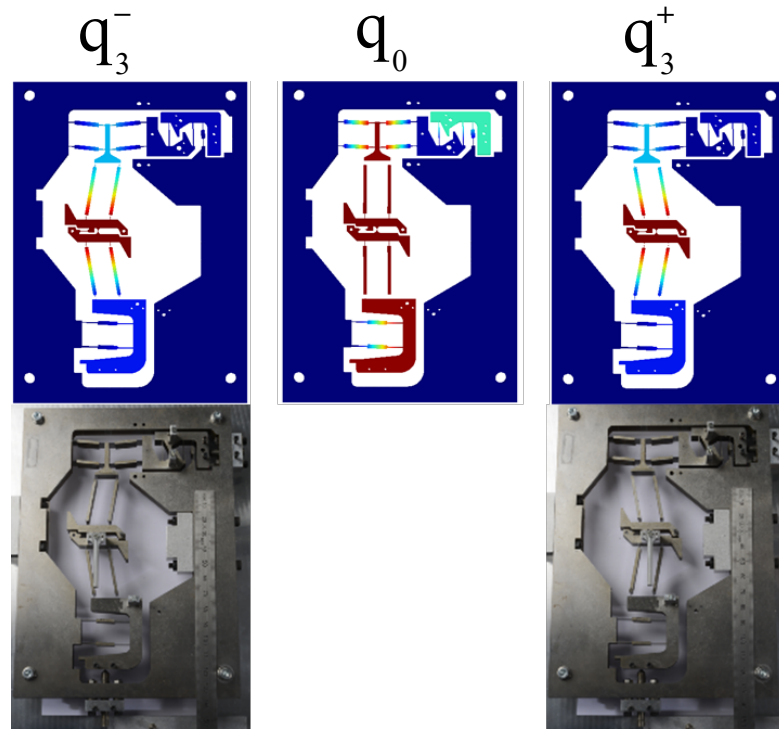


Figure 4.9 – Stable states, q_3^\pm and unstable state, q_0 of the mechanism programmed in bistable region II based on FEM (top) and experiment (bottom).

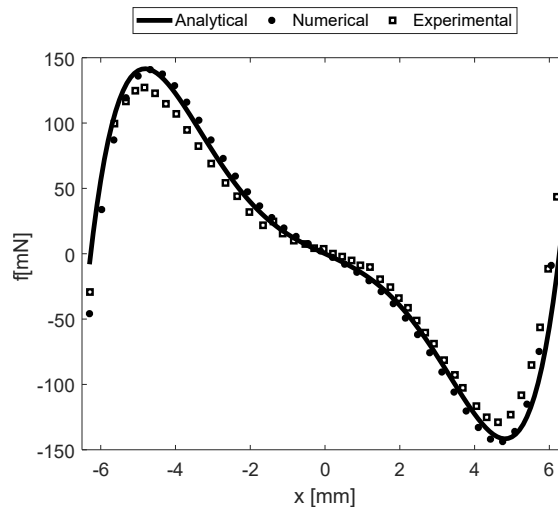


Figure 4.10 – The reaction force of the mechanism programmed as bistable in region II for $p_1 = 0.39[mm]$, $p_2 = -0.9[mm]$.

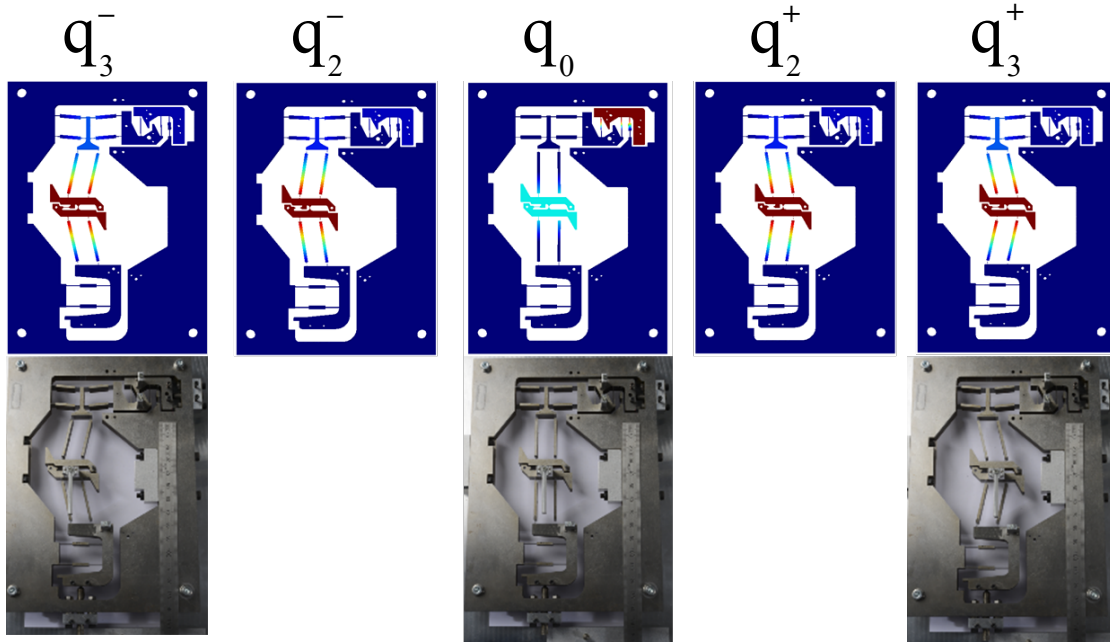


Figure 4.11 – Stable states, q_0 , q_3^\pm and unstable states, q_2^\pm of the mechanism programmed in tristable region based on FEM (top) and experiment (bottom).

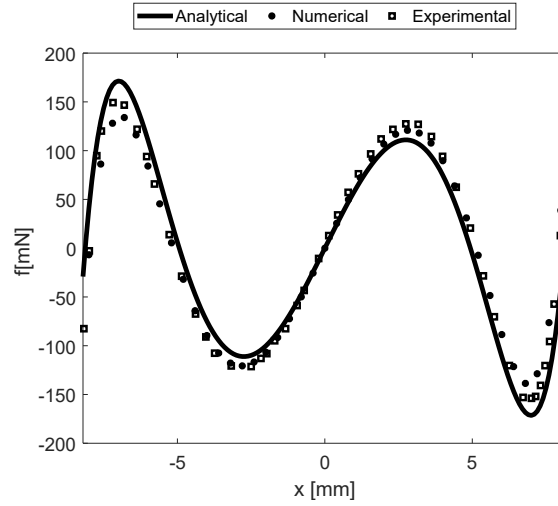


Figure 4.12 – The reaction force of the mechanism programmed as tristable for $p_1 = 0.37[mm]$, $p_2 = 0.0[mm]$.

Figure 4.14 illustrates the reaction force of the mechanism for $p_1 = 0.36[mm]$, $p_2 = 0.8[mm]$. As p_1 increases for a given p_2 , the stiffness of states q_2^\pm , q_3^\pm increases and the stiffness of states q_0 , q_1^\pm decreases. On increasing p_2 for a given p_1 , the stiffness of all equilibrium states, q_0 , q_1^\pm , q_2^\pm , q_3^\pm increases. It is clear that the switching force between q_1^+ and q_1^- is far lower than the switching force from q_1^+ to q_3^+ . This is an intrinsic limitation of the programmable T-shaped mechanism.

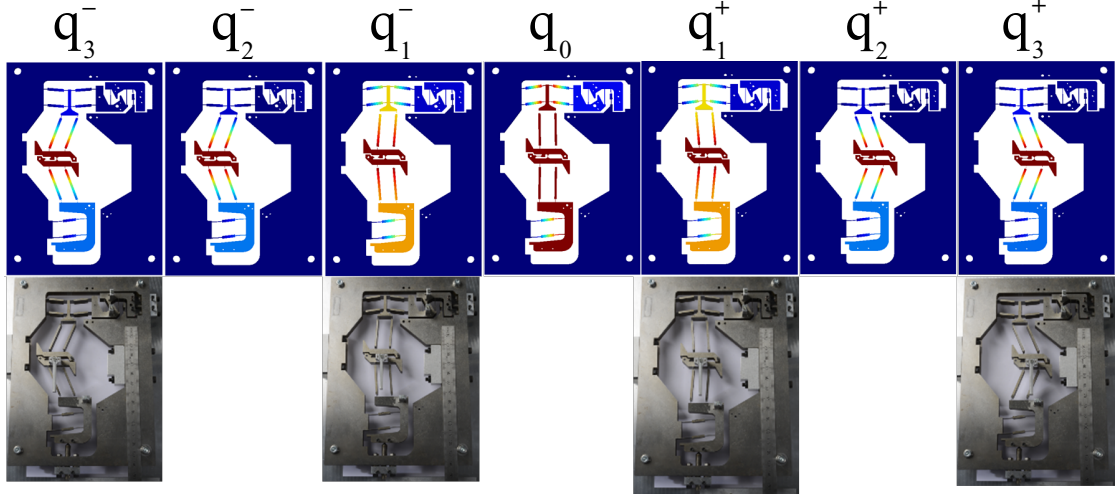


Figure 4.13 – Stable states, q_1^\pm , q_3^\pm , and unstable states, q_0 , q_2^\pm of the mechanism programmed in quadrastable region based on FEM (top) and experiment (bottom).

4.7.5 Summary

The reaction force of the mechanism in the different stability regions was measured. A discrepancy of less than 10% is found in estimating the switching forces for certain values of programming inputs between the analytical model on one side and experimental results and numerical simulations on the other. This is attributed to neglecting higher order nonlinear stiffness terms in the model, as in the case when the mechanism displacement exceeds the intermediate displacement range. We also ignore the axial displacement of the central block of module 1 on calculating the axial force of module 2 which affects the mechanism overall stiffness. Moreover, the effect of the elastic component of the axial displacement of the beams is ignored. The friction of the pulley, which was not considered in the model, is likely to affect the measured stiffness. However, we find the model sufficient for first order estimation of the stability behavior of the T-mechanism.

The effect of the programming inputs on the stiffness magnitude of the T-mechanism, at its equilibrium states based on equation(4.16), is summarized in Table 4.3, where \uparrow indicates an increase, \downarrow indicates a decrease, \rightarrow indicates no change and $\uparrow\downarrow$ denotes dependency of the trend on the range of the applied programming inputs.

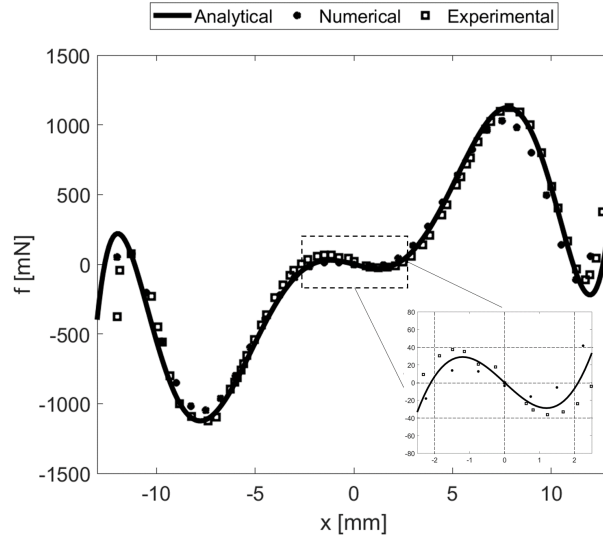


Figure 4.14 – The reaction force of the mechanism programmed as quadrastable for $p_1 = 0.36[mm]$, $p_2 = 2.8[mm]$. The inset illustrates the reaction force upon switching between second and third stable states.

4.7.6 Programming diagram

The programming diagram gives the number of stable states of the T-mechanism, i.e., DOS, upon changing its programming inputs, p_1 , p_2 .

The DOS can be found by evaluating the sign of the discriminant of Φ and the number of sign alteration between the coefficients $\beta_0, \beta_1, \beta_2, \beta_3$ in equation (4.13) [89]. The values of stability boundaries, p_1^{cr} , p_2^a , p_2^b , p_2^c were measured experimentally as reported in Figure 6.15 and show good match with analytical computations within less than 7%.

Table 4.3 – Effect of the programming inputs on stiffness magnitude of the existing equilibrium states.

Region	DOS	Programming inputs		Stiffness at equilibrium states			
		p_1	p_2	q_0	q_1^\pm	q_2^\pm	q_3^\pm
Monostable	1	\uparrow	\rightarrow	\downarrow			
		\rightarrow	\uparrow	\downarrow			
Bistable I	2	\uparrow	\rightarrow	\downarrow	\downarrow		
		\rightarrow	\uparrow	\uparrow	\uparrow		
Bistable II	2	\uparrow	\rightarrow	\uparrow			\uparrow
		\rightarrow	\uparrow	$\uparrow \downarrow$			\uparrow
Tristable	3	\uparrow	\rightarrow	\uparrow		\uparrow	\uparrow
		\rightarrow	\uparrow	$\uparrow \downarrow$		\uparrow	\uparrow
Quadrastable	4	\uparrow	\rightarrow	\downarrow	\downarrow	\uparrow	\uparrow
		\rightarrow	\uparrow	\uparrow	\uparrow	\uparrow	\uparrow

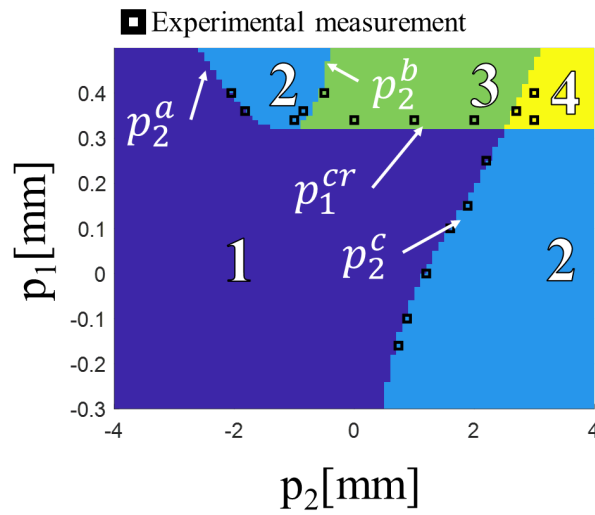


Figure 4.15 – Programming diagram of the T-mechanism in which stability boundaries p_1^{cr} , p_2^a , p_2^b , p_2^c are experimentally verified.

4.7.7 Equilibrium positions

We study the effect of the programming inputs, p_1 , p_2 on the positions of equilibrium states, which are the square roots of the positive-valued zeros of $\Phi(z)$, as given in equation (4.14). We fix one of the programming inputs and sweep the other one.

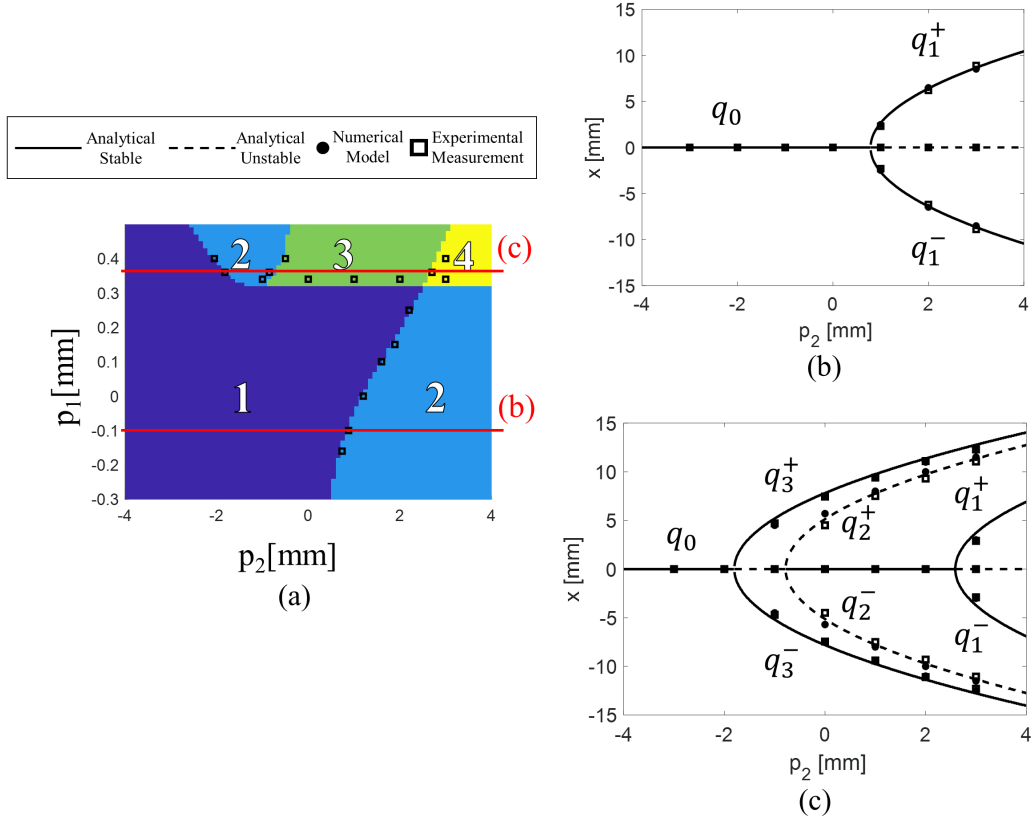


Figure 4.16 – (a) Selected p_1 values of the calculated equilibrium position diagrams as p_2 varies from -4[mm] to 4[mm]. Equilibrium positions diagram at (b) $p_1 = -0.1$ [mm], (c) $p_1 = 0.35$ [mm] verified both numerically and experimentally.

Fixing p_1 and sweeping p_2

There are two qualitatively different equilibrium diagrams as illustrated by the selected values in Figure 4.16(a).

The first case occurs when $p_1 < p_1^{cr}$, the mechanism is monostable with a stable state q_0 at $x = 0$. At $p_2 = p_2^c$, the stable state q_0 becomes unstable and bifurcates into two stable states q_1^\pm as given in Figure 4.16(b). The value of the bifurcation node $p_2 = p_2^c$ depends on p_1 . As p_1 increases, p_2^c increases as well.

The second case occurs when $p_1 > p_1^{cr}$ as illustrated in Figure 4.16(c). In this case, the mech-

anism is monostable for $p_2 < p_2^a$ with a stable state q_0 at $x = 0$. At $p_2 = p_2^a$, the stable state becomes unstable and bifurcates into two stable states q_3^\pm . The mechanism becomes bistable upon increasing p_2 . At $p_2 = p_2^b$, the unstable state q_0 becomes stable and bifurcates into two unstable states q_2^\pm . The mechanism is tristable with increasing p_2 . At $p_2 = p_2^c$, q_0 bifurcates again into two stable states, q_1^\pm and becomes unstable. The mechanism is quadrastable for $p_2 > p_2^c$.

Fixing p_2 and sweeping p_1

When p_2 is fixed as p_1 increases, the value p_2^a decreases and p_2^b, p_2^c increase. Both the values p_2^a, p_2^b exist only for $p_1 \geq p_1^{cr}$. We consider different cases illustrated in Figure 4.17(a).

If $p_2^a > p_2$ for all values of p_1 , the mechanism is monostable with a stable state q_0 at $x = 0$. In the case that p_2 is selected such that $p_2^a < p_2$ and $p_2^b > p_2$ for a certain range of p_1 , the mechanism shows both monostability and bistability. At $p_2^a = p_2$, pitch-fork bifurcation occurs at which stable state q_0 becomes unstable and bifurcates into two unstable states q_3^\pm [89].

If p_2 is selected such that $p_2^b < p_2$ and $p_2^c > p_2$ for a given range of $p_1 > p_1^{cr}$, the mechanism can show monostability, tristability and bistability. For $p_1 < p_1^{cr}$, the mechanism has a stable state q_0 at $x = 0$. At $p_1 = p_1^{cr}$, saddle-node bifurcation occurs and stable states, q_3^\pm , unstable states, q_2^\pm emerge. The mechanism is tristable.

As p_1 increases, p_2^b increases as well. When $p_2^b = p_2$, inverted pitchfork bifurcation occurs. The stable state q_0 becomes unstable and the two unstable states, q_2^\pm merge at $x = 0$, as illustrated in Figure 4.17(b) and the mechanism becomes bistable.

On increasing p_2 and sweeping p_1 , the value of the bifurcation node $p_2^b = p_2$ increases and the equilibrium states, q_2^\pm, q_3^\pm move apart from $x = 0$. When $p_2^b < p_2$ and $p_2^c > p_2$ over the entire range of p_1 , the mechanism functions as monostable for $p_1 < p_1^{cr}$ and tristable mechanism for $p_1 > p_1^{cr}$, as illustrated in Figure 4.17(c).

If p_2 is selected such that $p_2^c < p_2$ for a given range of $p_1 < p_1^{cr}$ and $p_2^b < p_2, p_2^c > p_2$ for $p_1 > p_1^{cr}$, the mechanism can exhibit bistability, monostability and tristability upon changing p_1 , as illustrated in Figure 4.17 (d). For $p_2^c < p_2$, the mechanism has two stable states, q_1^\pm and unstable state q_0 . As p_1 increases, p_2^c increases. At $p_2^c = p_2$, the stable state q_0 becomes stable and the two stable states q_1^\pm merge at $x = 0$ and the mechanism is monostable. At $p_1 = p_1^{cr}$, saddle-node bifurcation occurs and stable states, q_3^\pm and unstable states, q_2^\pm emerge rendering the mechanism tristable.

On further increase of p_2 , the value of the bifurcation node p_2^c increases. If $p_2^c = p_2$ at $p_1 > p_1^{cr}$, the mechanism shows quadrastability for $p_2^c < p_2$ and tristability for $p_2^c > p_2$ while $p_1 > p_1^{cr}$ as illustrated in Figure 4.17(e).

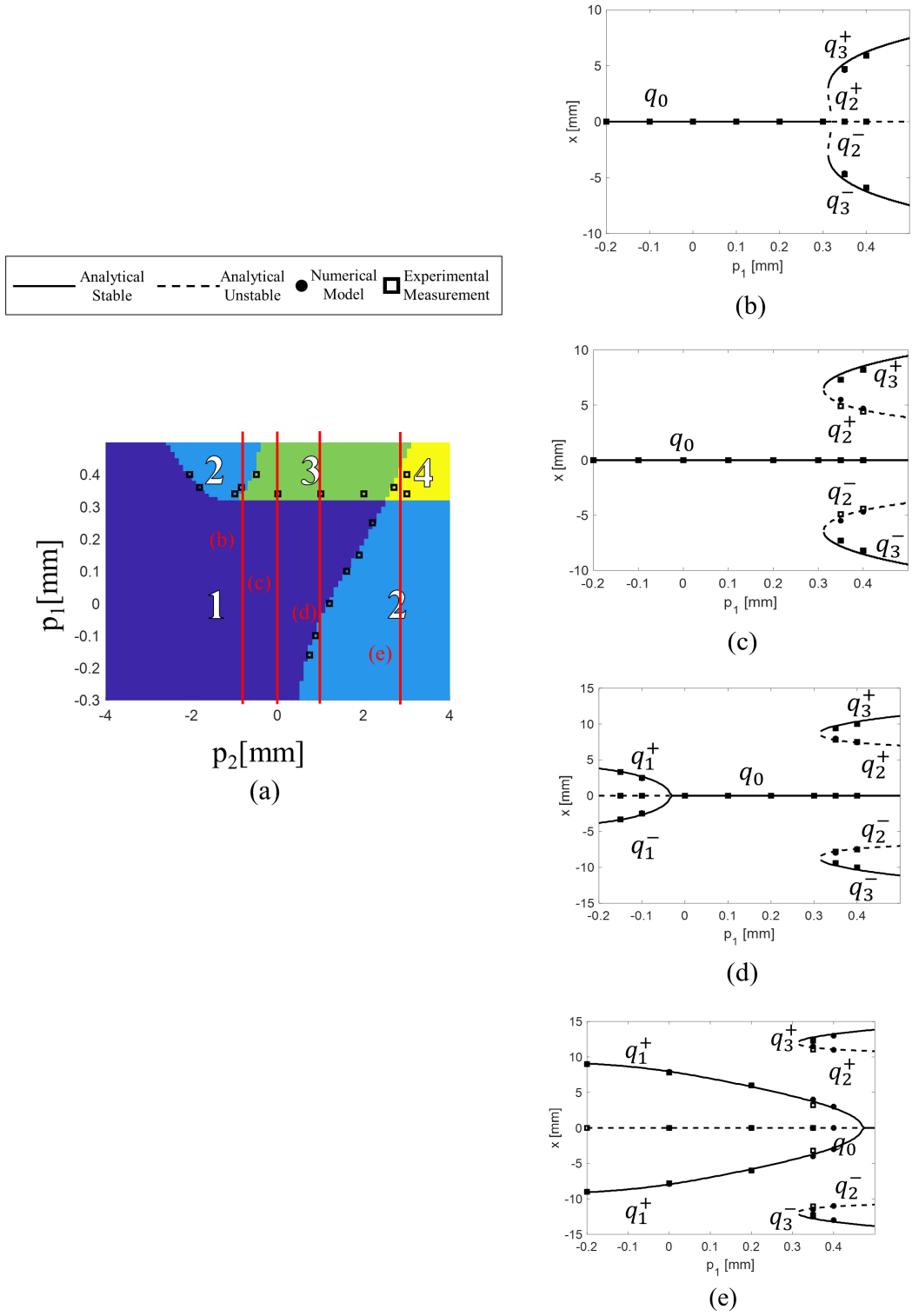


Figure 4.17 – (a) Selected p_2 values of the calculated equilibrium position diagrams as p_1 varies from $-0.2[mm]$ to $0.5[mm]$. Equilibrium positions diagram at (b) $p_2 = -1[mm]$, (c) $p_2 = 0[mm]$, (d) $p_2 = 1[mm]$, (e) $p_2 = 3[mm]$ verified numerically and experimentally.

4.7.8 Zero stiffness positions

As discussed in Section 3.6.4, the mechanism can exhibit zero stiffness along with multistable behavior. This occurs at the values of p_1 , p_2 at which zero stiffness states appear. The zero stiffness states can be found by calculating the roots of the tangential stiffness polynomial in a way similar to the equilibrium positions where the roots of the force polynomial were found, as illustrated in Figure 4.18. The boundaries of the zero stiffness map in Figure 4.18(d) correspond to the values of programming inputs at which zero stiffness occur.

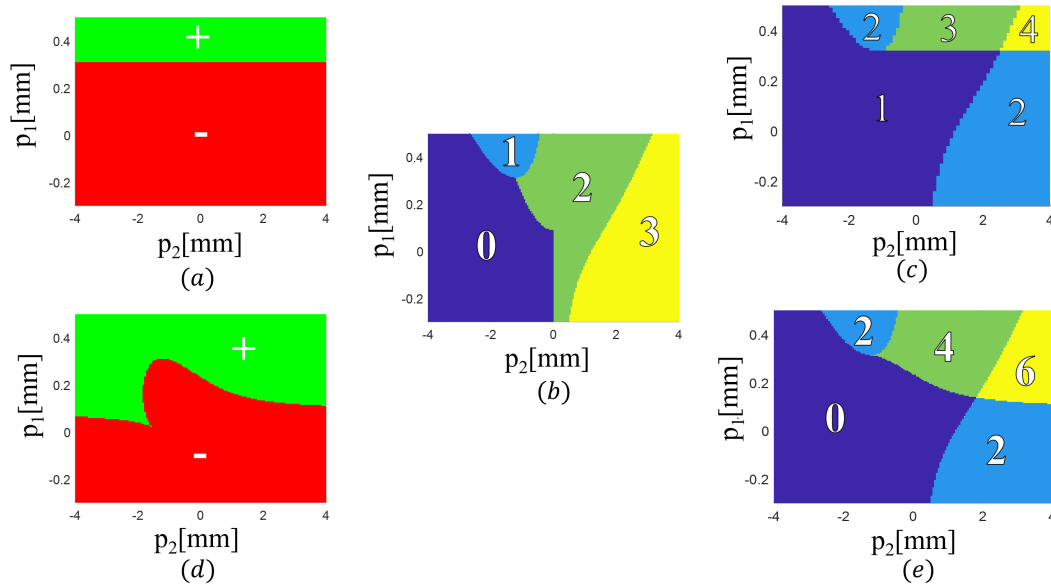


Figure 4.18 – (a) Sign of the discriminant of the force polynomial, (b) number of sign changes of the coefficient, (c) number of stable states, (d) sign of the discriminant of the stiffness polynomial, (e) number of zero stiffness states.

We selected points on the boundaries to verify the operation of the mechanism as zero force monostable (ZFMM), constant force monostable (CFMM), zero force bistable (ZFBM), constant force bistable (CFBM) and zero force tristable mechanisms (ZFTM). Analytical, numerical and experimental calculations were conducted to verify the zero stiffness behavior of the mechanism as illustrated in Figure 4.19.

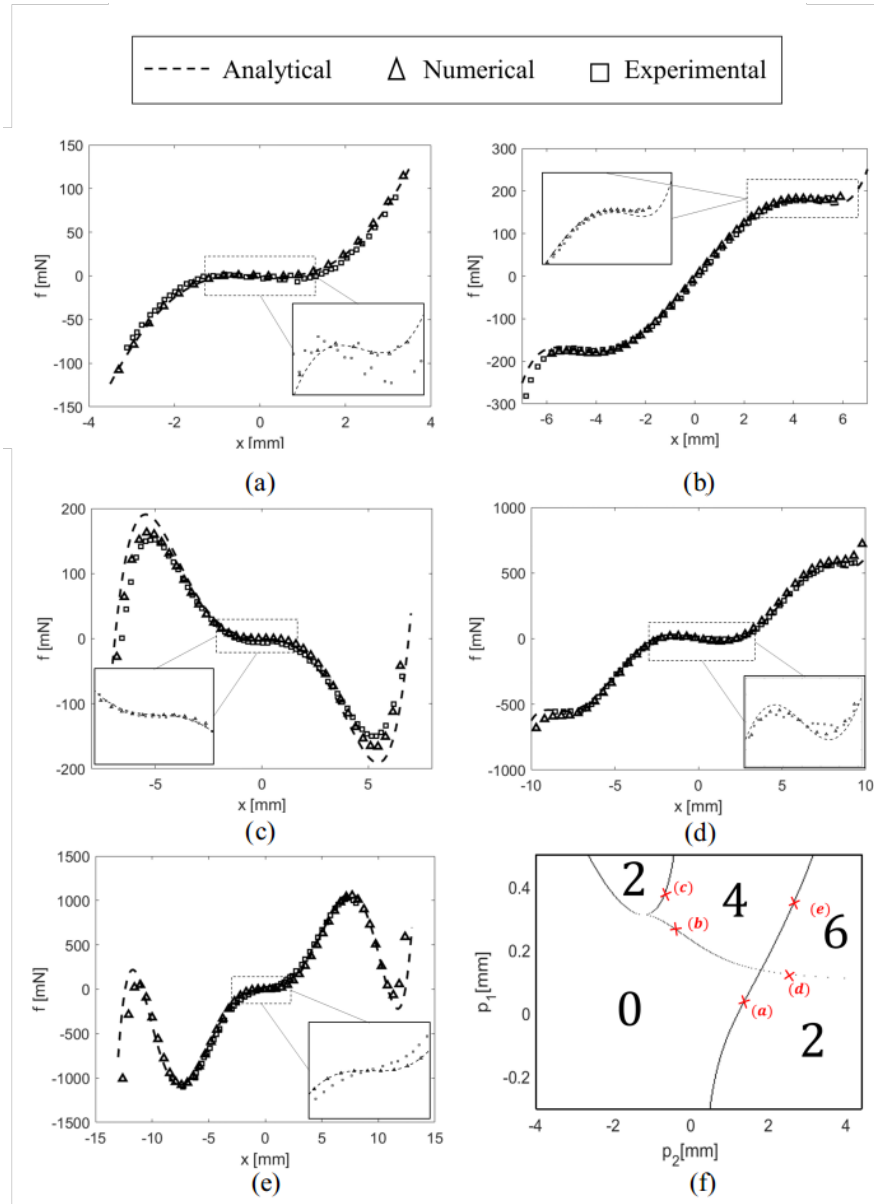


Figure 4.19 – Reaction force of the T-mechanism based on analytical, numerical and experimental measurements for (a) ZFMM at $p_1 = 0.09[mm]$, $p_2 = 1.6[mm]$, (b) CFMM at $p_1 = 0.24[mm]$, $p_2 = 0.0[mm]$, (c) ZFBM at $p_1 = 0.39[mm]$, $p_2 = -0.7[mm]$, (d) CFBM at $p_1 = 0.14[mm]$, $p_2 = 2[mm]$, (e) ZFTM at $p_1 = 0.35[mm]$, $p_2 = 2.65[mm]$, (f) selected points highlighted along the zero stiffness boundaries.

4.8 Conclusion

In this chapter, we experimentally verified the concept of stability programming using T-combined double parallelogram mechanism consisting of rectangular beam hinges. An analytical model of the mechanism was also derived. The reaction force is represented as seventh order polynomial from which the stability behavior of the mechanism is extracted.

Reaction force, programming diagram and equilibrium position bifurcation diagrams were calculated analytically, numerically and experimentally where a mismatch of less than 10% was found.

5 Application I: Detached Snap Escapement *

In this chapter, we present new escapements based on programmable multistable mechanisms for use in mechanical timekeepers such wrist watches. This yields a so-called *constant force detached snap escapement* providing repeatable energy impulses to the oscillator. Our invention is based on the lever escapement, where the anchor functionality is divided into a master anchor and a slave anchor. By further use of a spring as an energy buffer, the oscillator is detached from the direct impulse of the escape wheel. This makes oscillator energy essentially independent of barrel spring driving torque, thereby stabilizing oscillator amplitude. This resolves the problem of isochronism defect by keeping a constant amplitude, thus significantly improving timekeeping accuracy. Moreover, the anchor division detaches the oscillator from unlocking the escape wheel, making the oscillator perturbation also independent of the barrel spring driving torque to improve chronometric accuracy.

5.1 Introduction

The mechanical watch consists of a barrel spring as energy storage unit, a gear train for the display of the time and energy transfer, an escapement as a regulating unit and interface with the oscillator. A simple representation of the mechanical watch, given in Figure 5.1 shows the components of the watch as following [99]:

1. Barrel
2. Center pinion
3. Center wheel
4. Third pinion
5. Third wheel

* Some of the content of this chapter has been submitted on May 19, 2016 as an invention report to the technology transfer office of EPFL

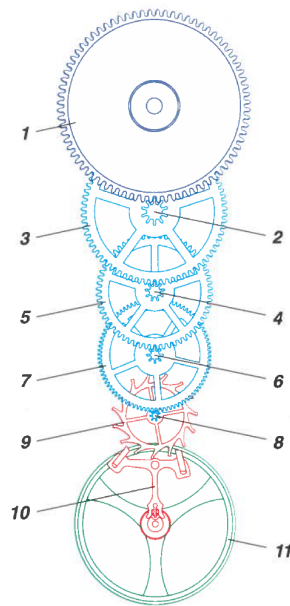


Figure 5.1 – Components of mechanical watch.

- 6. Fourth pinion
- 7. Fourth wheel
- 8. Escape pinion
- 9. Escape wheel
- 10. Pallet fork
- 11. Balance wheel and hairspring

The barrel spring 1 provides the required energy for maintaining the oscillation of the balance wheel and hair spring 11 through the gear train 2-8. The gear train is also used for the time display in terms of hours, minutes and seconds. The escapement 9, 10 works as a regulating unit. It has two functions:

- It regulates the energy given to the oscillator – impulse action.
- It counts the number of oscillations – locking action.

In about 1609, Galileo Galilei formulated the principle of isochronism stating that the period of the oscillator is independent of its energy. Isochronism liberates the measure of time from the energy source and greatly increases chronometric precision compared to previous time bases.

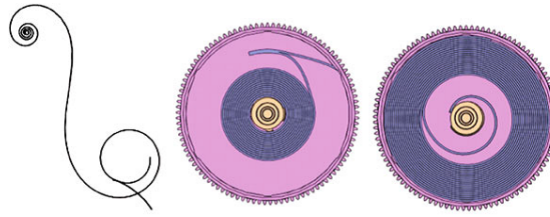


Figure 5.2 – Main spring fully wound (left) and fully unwound (right).

In the case of the mechanical watch, the oscillator consists of a balance wheel and hair spring. Though Hooke's Law predicts that this oscillator is isochronous in theory, but in practice it suffers from isochronism defects [99]. A constant energy supply to the oscillator would maintain a constant amplitude and so a constant period of oscillation. Traditionally, this was done using a fusée [100], but this mechanism is complicated and rarely used in watches. The standard approach has been to do this at the level of the escapement, what is commonly referred to in horology as *constant force escapements*.

The barrel spring, shown in Figure 5.2, is the energy source for the oscillator [99]. However, the torque exerted, in turn energy provided, varies as function of the level of energy stored in the barrel spring, as shown in Figure 5.3 [99].

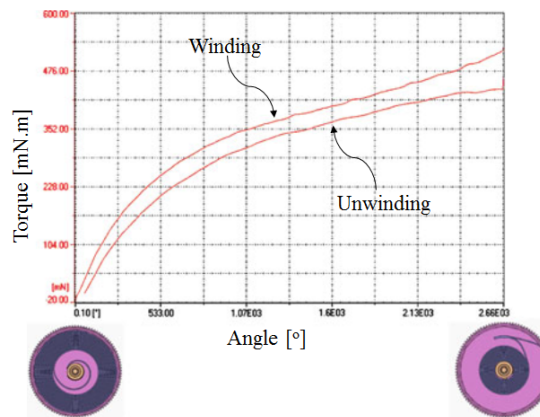


Figure 5.3 – Variation of the torque of the barrel spring with respect to the winding angle.

5.2 State of the art

5.2.1 Constant force escapements

A number of so-called *constant force escapements* have been invented to minimize the variation over time of the energy delivered to the oscillator. We divide escapements into variable force escapements and constant force escapements. With variable force escapements, the energy provided to the oscillator at each cycle depends directly on the driving torque of the main spring.

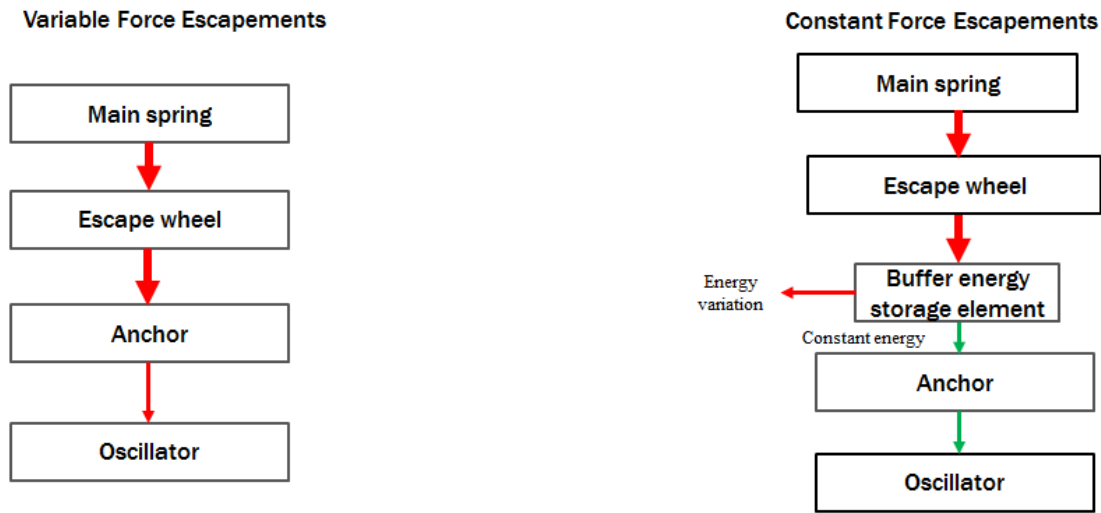


Figure 5.4 – Comparison of the impulse action between variable force escapements and constant force escapements.

Constant energy impulse

Constant force escapements incorporate a buffer acting as a temporary energy storage element. This element provides a constant energy to the oscillator at each cycle and is regularly reloaded by the main energy source. The buffer element is usually a spring or a movable mass. Figure 5.4 shows a conceptual diagram explaining the difference between variable force escapements and constant force escapements. In the case of variable force escapements, the impulse to the oscillator depends directly on the driving torque in the main spring.

Detached unlocking

The second function of the escapement is counting periods of the oscillator. The counting is performed through signals sent from the oscillator consisting of unlocking of the escape wheel by the oscillator. The unlocking requires taking energy from the oscillator and this energy depends on the driving torque of the barrel spring. Therefore, even for a constant force escapement, oscillator amplitude is still affected by the state of the barrel spring due to the variation in unlocking energy.

This energy variation can be eliminated by detaching the oscillator during the unlocking process, known as detached unlocking of the escape wheel. We therefore call such escapements detached escapements as opposed to attached escapements lacking this feature. Figure 5.5 shows the conceptual differences between attached and detached escapements.

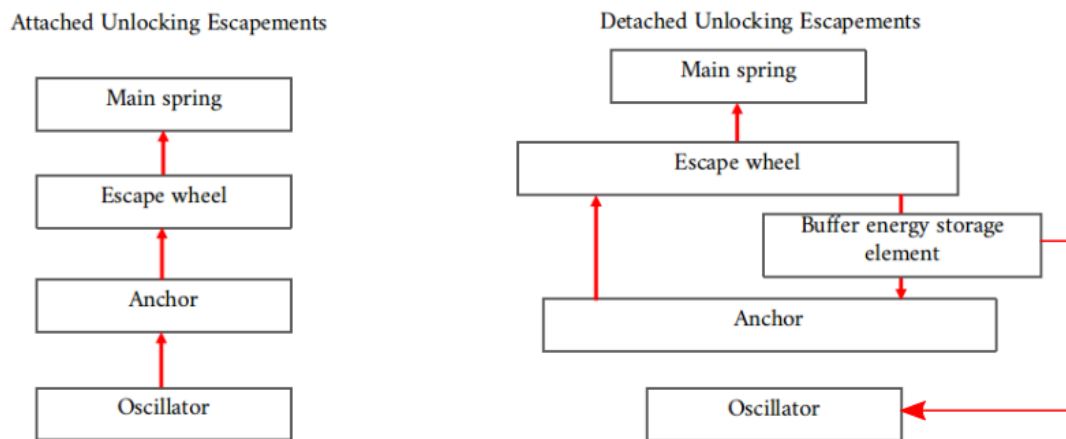


Figure 5.5 – Comparison between the unlocking actions of attached escapements and detached escapements.

Examples of constant force escapements

Constant force escapements are also known as remontoire escapements when applied to clocks. They have a long history where both gravitational and spring forces have been used as energy storage.

1. Gravity escapement

Gravity escapements are constant force escapements for pendulum clocks [101]. The gravity escapement appears to have been invented by Thomas Mudge and the most famous is the *three-legged double wheel escapement* invented by Edmund Beckett Denison for the great clock at Westminster Big Ben [100] which allowed this large turret clock to achieve its 1 second a day accuracy specification [102].

2. Arnfield's detached gravity escapement

Following Harrison's edict that *the pendulum must have dominion over the clockwork* [101], much effort was made to completely isolate the pendulum oscillator from any outside disturbance. Constant force escapements were a first step, but the energy required by the oscillator to unlock the movement depends on friction at the pallets which in turn depends on escape wheel torque and thus on the state of the energy source. In 1987, John Arnfield successfully detached the oscillator from direct unlocking of the escape wheel by modifying the design of Edmund Beckett Denison's Big Ben escapement [103].

3. Girard-Perregaux constant force escapement

This escapement was patented by N. Dehon in 1999 [7] and commercialized by Girard-Perregaux in 2013 for wristwatches. An axially loaded buckled beam is used as the energy

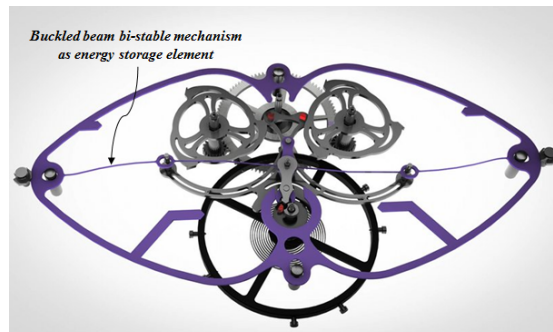


Figure 5.6 – Girard - Perregaux constant force escapement.



Figure 5.7 – Ulysse Nardin constant force escapement.

storage buffer. This beam shows a bistable response providing constant energy impulses to the oscillator.

4. Ulysse Nardin constant force escapement

This escapement uses a pivot based on flexure for the escapement anchor [104]. The mechanism exhibits bistability when an axial force is applied to the virtual pivot, so a constant energy impulse is transmitted to the oscillator.

Disadvantages of constant force escapements

Most constant force escapements do not have detached unlocking. Therefore, oscillator energy is still dependent on barrel spring energy due to friction at pallets and the recoil of the escape wheel. As mentioned above, for clocks, this problem was finally solved by Arnfield [103].

The Girard - Perregaux (GP) and Ulysse Nardin constant force escapements are based on preloaded buckled beam bistable mechanisms. Buckled beam mechanisms are sensitive to preload, changing dramatically the energy impulse to the oscillator. The buckling is a delicate phenomenon which is difficult to model theoretically. Moreover, they are sensitive to the

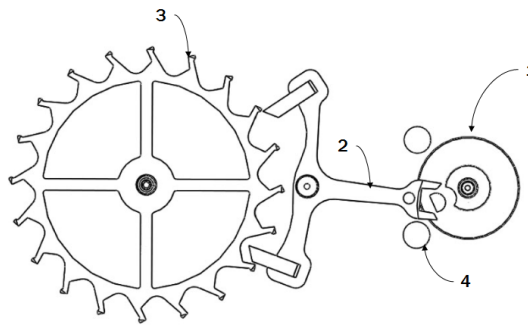


Figure 5.8 – Bottom view of the Swiss lever escapement.

temperature variation.

A disadvantage of GP constant force escapement is the size and it occupies a large part of the watch, requiring the rearrangement of the whole watch components.

Finally, many constant force escapements are inherently not self-starting, i.e., they cannot be started from a stopped state by winding the crown.

5.2.2 Swiss lever escapement

The Swiss lever escapement is used in almost all mechanical wrist watches. It consists of a roller 1, anchor 2 and escape wheel 4, as shown in Figure 5.8. The roller is connected to the balance wheel oscillator. Through the gear train, the escape wheel is coupled to the barrel spring. The Swiss lever escapement is not a constant force escapement.

Operation of the Swiss lever escapement

The Swiss lever escapement performs the two functions of impulsing the oscillator and unlocking the escape wheel by the anchor 2 which also acts as the lever. A description of the phases begins with Figure 5.8 in which the escape wheel 3 is loaded by the main spring, the escape wheel is locked by the entry pallet and the anchor is locked by the banking pin 4. When the oscillator 1 contacts the anchor fork it unlocks the movement, the escape wheel first recoils, due to draw, then slides on the rest plane of the anchor pallet. The tooth of the escape wheel then clears the rest plane and the escape wheel turns freely until it hits and slides on the impulse plane of the anchor, providing energy to the oscillator. After that, the escape wheel rotates freely until it hits the rest plane of the exit pallet. At this point, the escape wheel is locked, and this cycle is repeated on the exit pallet.

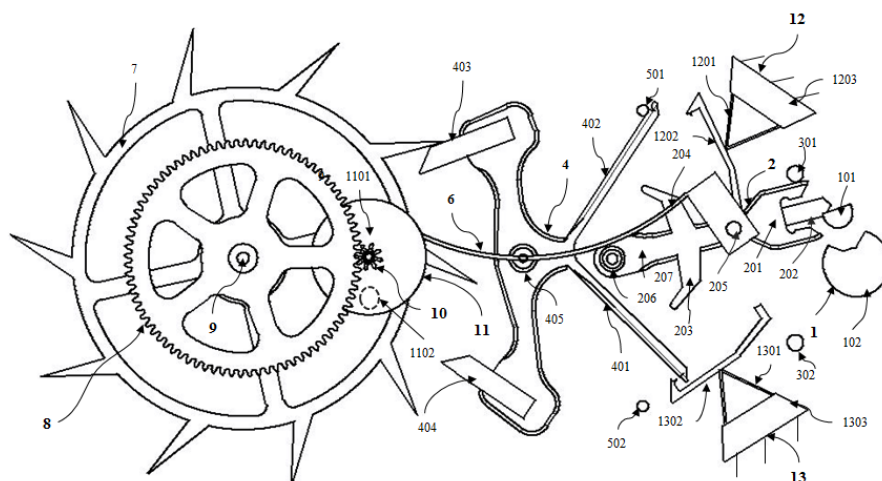


Figure 5.9 – Snap escapement.

Disadvantages of the Swiss lever escapement

The main disadvantages of the Swiss lever escapement, as compared to other watch escapements, are

1. Sliding of escape wheel teeth on anchor pallets is frictional and requires lubrication.
2. All impulses are indirect via a lever.
3. Variation of the energy delivered to the oscillator due to the variation of the driving torque of the main spring.

5.3 Description of the invention

Our invention is a constant force escapement which we have called *snap escapement*. The invention provides constant energy impulses to the oscillator using a programmable multistable mechanism. Additionally, it detaches the oscillator from the escape wheel, thus regularizing oscillator energy losses due to unlocking.

5.3.1 Snap escapement

The snap escapement, shown in Figure 5.9, consists of a roller 1 attached to the oscillator where the oscillator interacts with the escapement. The escapement master anchor 2 impulses the oscillator. The escapement slave anchor locks and unlocks the escape wheel 7. The spring 6 is used as an energy storage buffer element. The spring 6 is reloaded by the escape wheel 7 through a gear 8, a shaft 9, a pinion 10 and a spring wheel 11. Two locking mechanisms 12, 13 are used for securing the motion of the slave anchor against shocks. The following is a list of

Table 5.1 – Components of the Snap Escapement.

Number	Component	Number	Component
1	Roller	101	Impulse pin
102	Disc	2	Master anchor
201	Fork	202	Dart
203	Entry arm	204	Exit arm
205	Spring pin	206	Rotary bearings
207	Lever	3	Master banking pins
301	Entry banking pins	302	Exit banking pins
4	Slave anchor	401	Entry arm
402	Exit arm	403	Entry pallet
404	Exit pallet	405	Rotary bearing
5	Slave banking pins	501	Entry banking pin
502	Exit banking pin	6	Spring
7	Escape wheel	8	Gear
9	Coupling shaft	10	Spring pinion
11	Spring wheel	1101	Spring disc
1102	Spring pin	12	Entry locking mechanism
1201	Locking lever	1202	Locking pivot
1203	Anchoring block	13	Exit locking mechanism
1301	Locking lever	1302	Locking pivot
1303	Anchoring block		

components of the snap escapement.

The snap escapement is based on a programmable multistable mechanism, where the oscillator will program the mechanism from bistability to monostability. Then, energy is released to impulse the oscillator. The escape wheel will program the mechanism from monostability to bistability where the energy is stored in the mechanism.

5.3.2 Snap mechanism

The *snap mechanism* is a programmable multistable mechanism given in Figure 5.10. It consists of a lever rotating around point O connected by a linear spring to the point p . The spring is free to rotate on both of its ends.

The position of point P modifies the mechanism strain energy changing the mechanism stability behavior from monostability to bistability as illustrated in Figure 5.10. As the mechanism switches from bistability to monostability, it releases energy as illustrated in Figures 5.10(c), (d).

For the escapement, we used an equivalent PMM given in Figure 5.11. It is integrated with the lever escapement such that the master anchor 2, representing the lever, is connected by the spring 6 to the spring pin 1102, equivalent to point p , on the spring wheel 11 as shown in

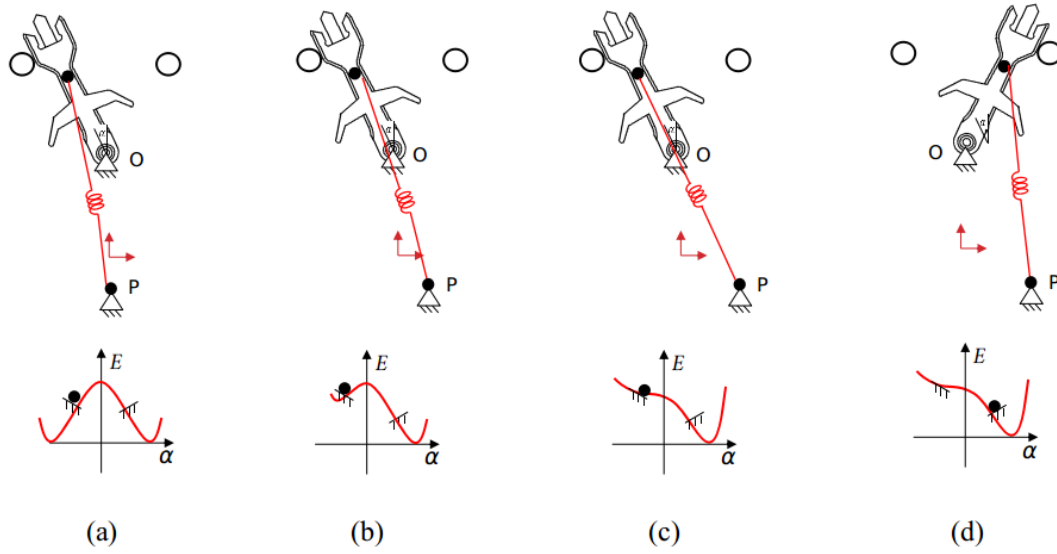


Figure 5.10 – Snap mechanism and its strain energy when programmed as (a) symmetric bistable, (b) asymmetric bistable, (c) zero force monostable, (d) monostable. The ball represents the position of the lever.

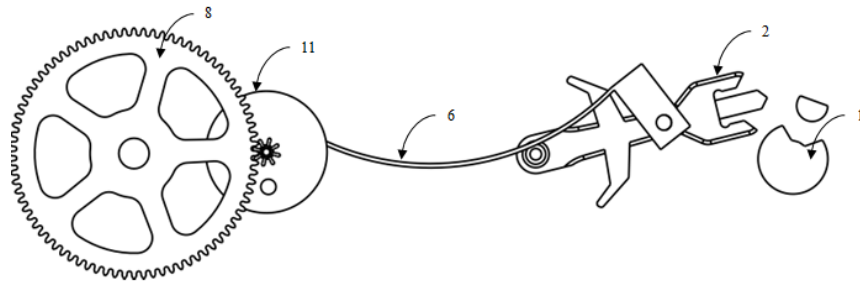


Figure 5.11 – Equivalent snap mechanism integrated within our presented escapement.

Figure 5.11. The mechanism is actuated by the oscillator through the roller 1.

The spring wheel 11 is coupled to the escape wheel 7 through gear 8 and pinion 10. As the tooth of the escape wheel moves from the entry 403 to the exit pallet 404 of the slave anchor, the spring wheel rotates 180 degrees.

The basic concept behind the mechanism is illustrated in Figure 5.12. Based on the location of point P representing the spring pin 1102 relative to the point O, the mechanism functions either as a bistable mechanism or a monostable mechanism. In both cases, the mechanism snaps between a high energy states A and C to a low energy states B and D, respectively.

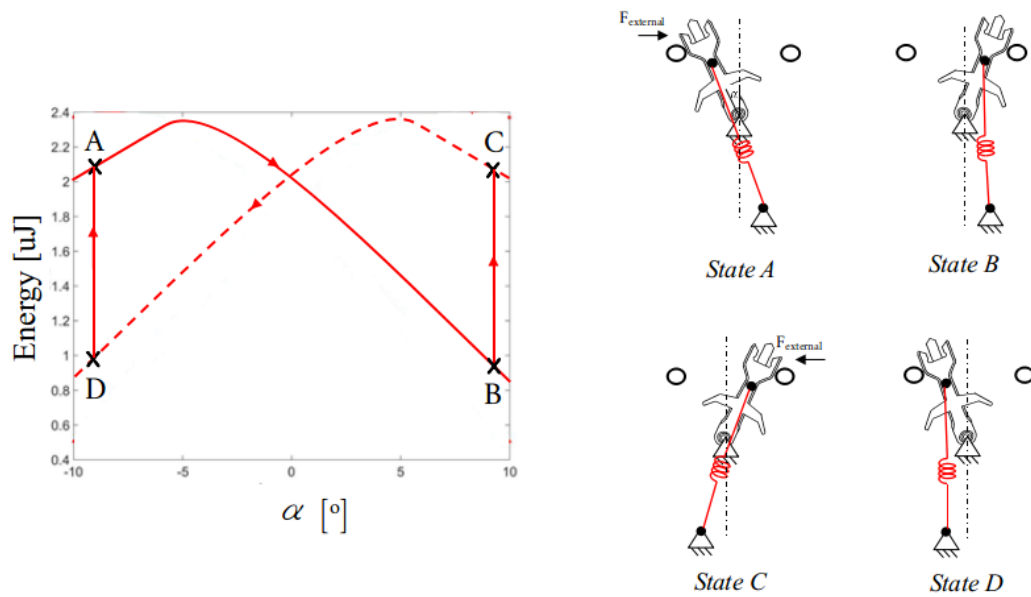


Figure 5.12 – Snap mechanism as it switches between its stable states.

5.3.3 Master and slave anchors

Two anchors are used in this escapement, which we denote master anchor 2 and slave anchor 4, as illustrated in Figure 5.13. The master anchor 2 impulses the oscillator 1 with a constant energy through the snap mechanism. After that, the master anchor contacts and moves the slave anchor 4 which in turn unlocks the escape wheel 7. Note that unlocking is done without interaction with the oscillator.

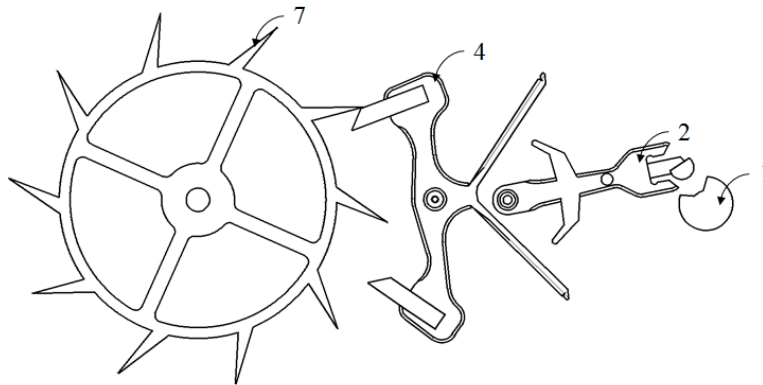


Figure 5.13 – Master(2) and slave(4) anchors of the snap escapement.

5.3.4 Operation of the snap escapement

The snap escapement has five principal phases:

- Actuating the master anchor
- Impulsing the oscillator
- Unlocking the escape wheel
- Impulsing the slave anchor
- Loading the spring

The escapement action consists of 14 steps.

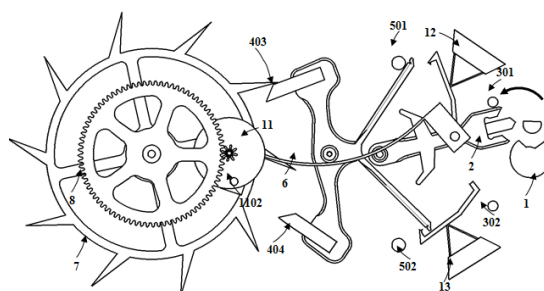


Figure 5.14 – Step 1

Step 1: Initial state - Figure 5.14

- Roller 1: is moving freely counterclockwise.
- Master anchor 2: rests on the banking pin 301.

- Slave anchor 4: rests on banking pin 501 and is locked by the tooth of escape wheel 7 due to draw.
- Spring 6: is loaded.
- Escape wheel 7: is immobile on the rest plane of the entry pallet 403 of the slave anchor 4.
- Spring wheel 11: is not moving.

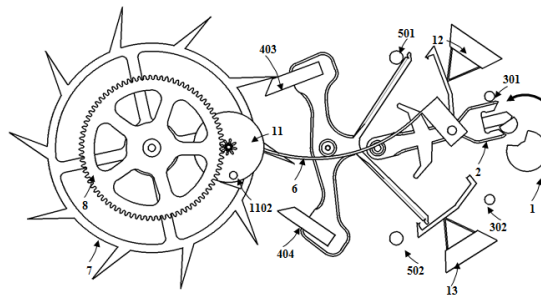


Figure 5.15 – Step 2.

Step 2: Start of actuation of the master anchor - Figure 5.15

- Roller 1: contacts, unlocks and moves the master anchor 2.
- Master anchor 2: is unlocked and moved by roller 1 towards its unstable position.
- Slave anchor 4: rests on the banking pin 501 and is locked by the tooth of the escape wheel 7.
- Spring 6: is gaining energy.
- Escape wheel 7: is immobile on the rest plane of the entry pallet 403 of the slave anchor.
- Spring wheel 11: is not moving.

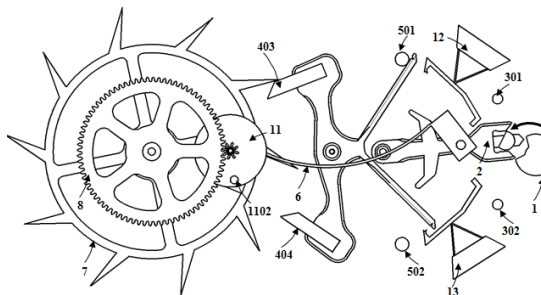


Figure 5.16 – Step 3.

Step 3: End of actuation of the master anchor - Figure 5.16

Chapter 5. Application I: Detached Snap Escapement

- Roller 1: is moving the master anchor 2 and moving counterclockwise
- Master anchor 2: is in basin of attraction of its second stable position.
- Slave anchor 4: rests on the banking pin 501 and is locked by the tooth of the escape wheel 7.
- Spring 6: is gaining/releasing energy design dependent.
- Escape wheel 7: is immobile on the rest plane of the entry pallet 403 of the slave anchor 4.
- Spring wheel 11: is not moving.

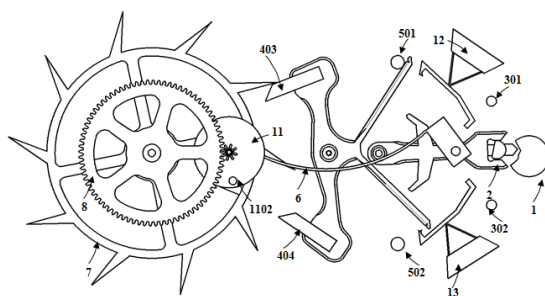


Figure 5.17 – Step 4.

Step 4: Start of impulse to the oscillator - Figure 5.17

- Roller 1: is pushed by the master anchor 2.
- Master anchor 2: is pushing the roller 1.
- Slave anchor 4: rests on the banking pin 501 and is locked by the tooth of the escape wheel 7.
- Spring 6: is releasing energy.
- Escape wheel 7: is immobile on the rest plane of the entry pallet 403 of the slave anchor 4.
- Spring wheel 11: is not moving.

Step 5: End of impulse to the oscillator - Figure 5.18

- Roller 1: moves freely in counterclockwise direction.
- Master anchor 2: moves toward its second stable position.

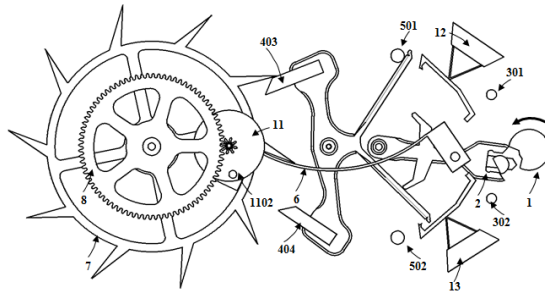


Figure 5.18 – Step 5.

- Slave anchor: rests on the banking pin 501.
- Spring 6: is releasing energy.
- Escape wheel 7: is immobile on the rest plane of the entry pallet 403 of the slave anchor 4.
- Spring wheel 11: is not moving.

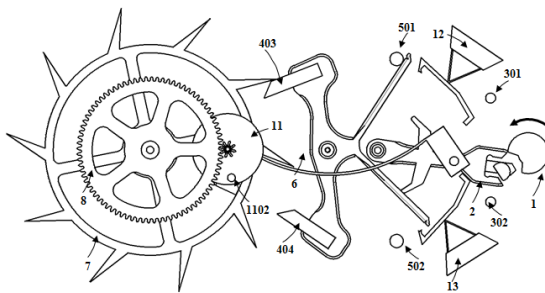


Figure 5.19 – Step 6.

Step 6: Unlocking of the slave anchor - Figure 5.19

- Roller: is free and moving counterclockwise.
- Master anchor 2: unlocks the locking lever 13 of the slave anchor 4.
- Slave anchor 4: turns clockwise.
- Spring 6: is gaining/releasing energy design dependent.
- Escape wheel 7: is immobile and on the rest plane of the entry pallet 403 of the slave anchor.
- Spring wheel 11: is not moving.

Step 7: Start of unlocking of escape wheel - Figure 5.20

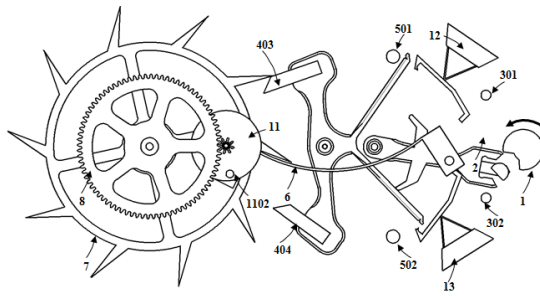


Figure 5.20 – Step 7.

- Roller 1: is free and moving counterclockwise.
- Master anchor 2: moves the slave anchor 4.
- Slave anchor 4: moved by the master anchor 2.
- Spring 6: is releasing energy.
- Escape wheel 7: slides on the rest plane of the entry pallet 403 of the slave anchor 4 and is moving counterclockwise due to draw.
- Spring wheel 11: is moving clockwise.

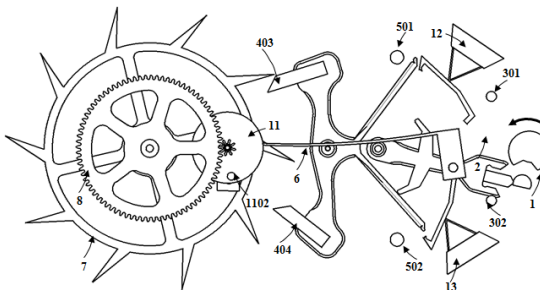


Figure 5.21 – Step 8.

Step 8: End of the unlocking of the escape wheel - Figure 5.21

- Roller 1: is free and moving counterclockwise.
- Master anchor 2: rests on the banking pin 302.
- Slave anchor 4: turning freely clockwise catching up to slave anchor.
- Spring 6: is at its low energy state.
- Escape wheel 7: leaves the rest plane 403 and starts to turn freely clockwise.

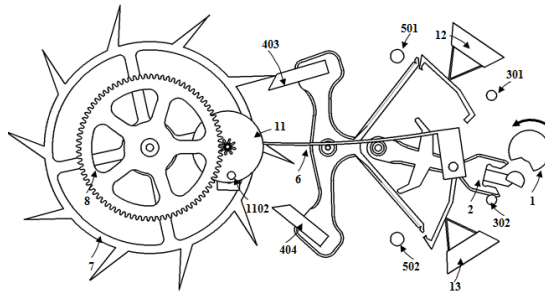


Figure 5.22 – Step 9.

- Spring wheel 11: is moving counterclockwise.

Step 9: Escape wheel catches up to the slave anchor- Figure 5.22

- Roller 1: is free and moving counterclockwise.
- Master anchor: rests on the banking pin 302.
- Slave anchor 4: turning freely clockwise until contacted by the escape wheel.
- Spring 6: is at low energy state.
- Escape wheel 7: moves freely until it hits the impulse plane of the entry pallet 403 of the slave anchor 4.
- Spring wheel 11: is moving counterclockwise.

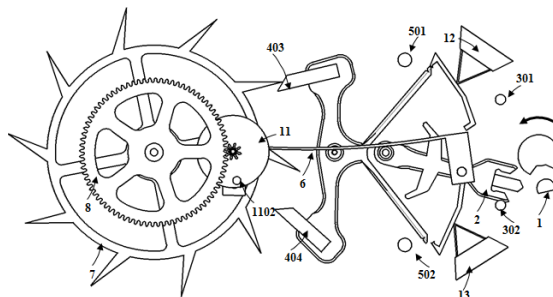


Figure 5.23 – Step 10.

Step 10: Impulse to the slave anchor - Figure 5.23

- Roller 1: is free and moving counterclockwise.
- Master anchor 2: rests on the banking pin 302.
- Slave anchor 4: moved by the escape wheel 7

- Spring 6: is releasing energy.
- Escape wheel 7: slides on the impulse plane of the slave anchor 4 and moving it.
- Spring wheel 11: is moving counterclockwise loading spring 6.

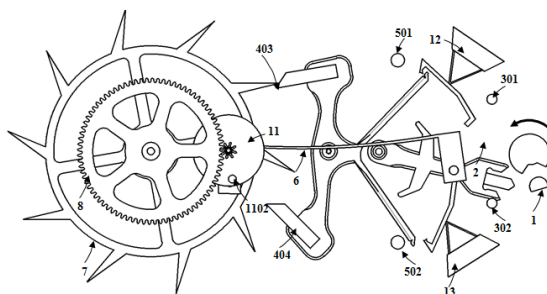


Figure 5.24 – Step 11.

Step 11: Slave anchor enters the locking mechanism - Figure 5.24

- Roller 1: is free and moving counterclockwise.
- Master anchor 2: resting on the banking pin 302.
- Slave anchor 4: is moved by the escape wheel 7 entering the locking mechanism 12.
- Spring 6: is at low energy state.
- Escape wheel 7: moves clockwise sliding on the impulse plane 403 of the slave anchor 4.
- Spring wheel 11: is moving counterclockwise loading spring 6.

Step 12: End of the impulse of the slave anchor - Figure 5.25

- Roller 1: is free and moving counterclockwise.
- Master anchor 2: resting on the banking pin 302.
- Slave anchor 4: turns freely until it reaches the banking pin 502.
- Spring 6: is around its low energy state.
- Escape wheel 7: leaves slave anchor impulse plane 403 and is moving clockwise loading the spring.
- Spring wheel 11: is moving counterclockwise loading spring 6.

Step 13: Loading the spring - Figure 5.26

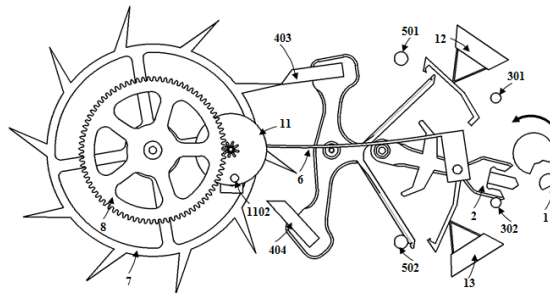


Figure 5.25 – Step 12.

- Roller 1: is free and moving counterclockwise
- Master anchor 2: rests on the banking pin 302
- Slave anchor 4: rests on the banking pin 502.
- Spring 6: is loading by the spring wheel 11.
- Escape wheel 7: rotates clockwise towards the rest plane of the exit pallet 404 of the slave anchor 4.
- Spring wheel 11: moved counterclockwise for the remaining part of its 180 degree rotation, loading the spring 6.

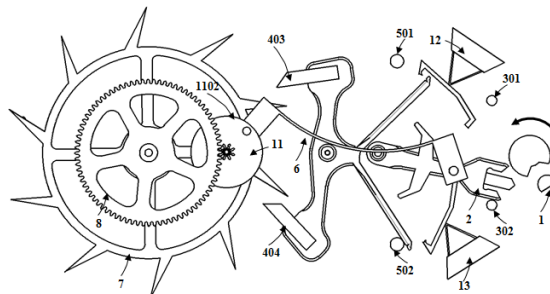


Figure 5.26 – Step 13.

Step 14: End of loading the spring - Figure 5.27

- Roller 1: is free and moving counterclockwise
- Master anchor 2: rests on the banking pin 302
- Slave anchor 4: rests on the banking pin 502.
- Spring 6: is loaded by the spring wheel 11.
- Escape wheel 7: completes its 18 degrees rotation by reaching the rest plane of the exit pallet.

- Spring wheel 11: completes its 180 degrees rotation counterclockwise, loading the spring 6.

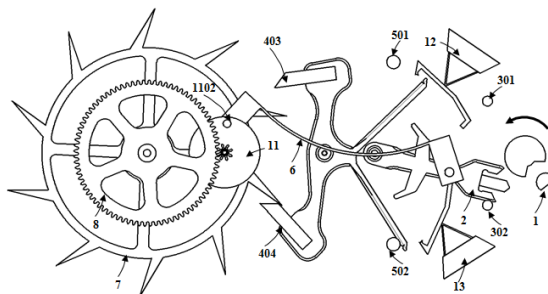


Figure 5.27 – Step 14.

5.3.5 Security

Mechanical watches are susceptible to shocks and must be secured against these shocks. In particular, the anchors of the snap escapement must be secured.

In our invention, the master anchor 2 is secured by the dart 202 and the disc of the roller 102. The slave anchor is locked by draw and pressure of the escape wheel and by the locking mechanisms 12 and 13.

5.3.6 Self-starting

It is considered desirable for a watch to be self-starting. This is generally taken to mean that after letting the movement completely runs down, it is always possible to restart the watch by simply winding the crown. One of the advantages of the Swiss lever escapement is that it is self-starting.

The versions of the snap escapement presented above do not appear to be inherently self-starting. In order to self-start, the movement must stop with the escape wheel unlocked since winding the crown with a locked escape wheel only increases locking pressure due to draw.

An examination of the escapement phases show that when the escape wheel is unlocked, the master anchor is locked and therefore cannot be unlocked since the oscillator is assumed immobile.

It is conceivable that the invention could be modified to ensure self-starting.

5.4 Demonstrator

A demonstrator of the snap escapement was built. A rubber band was used as the elastic element for energy storage. Figure 5.28 gives the structured demonstrator. The operation of the snap mechanism was verified using a separate demonstrator illustrated in Figure 5.29.

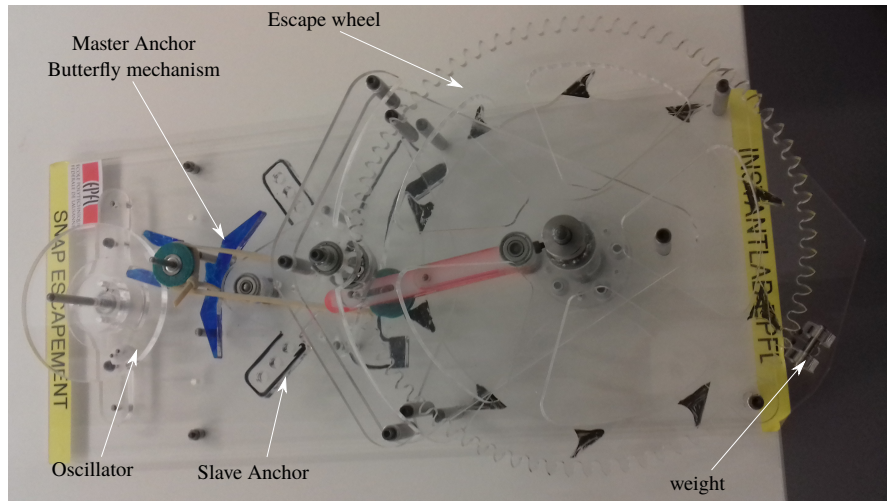


Figure 5.28 – A demonstrator of the snap escapement.

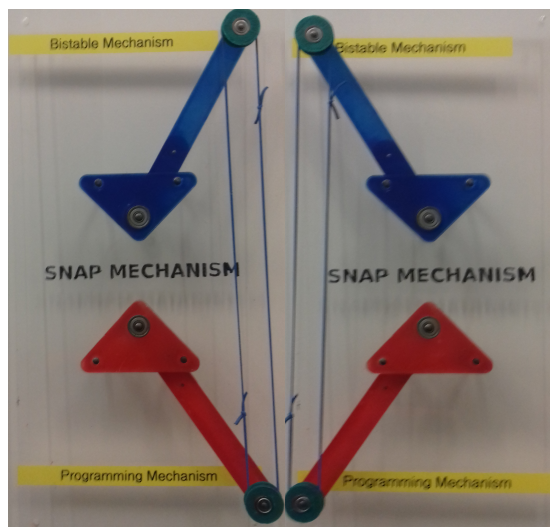


Figure 5.29 – Snap bistable mechanism - two stable states, red lever for programming and blue lever is the output.

A high speed camera was utilized to verify the different operation phases of the snap escapement operations as illustrated in Figures 5.30-5.35 while the roller is rotating in the counter clockwise direction. This includes master anchor unlocking, oscillator impulse, escape wheel unlocking, locking of slave anchor and spring reload.

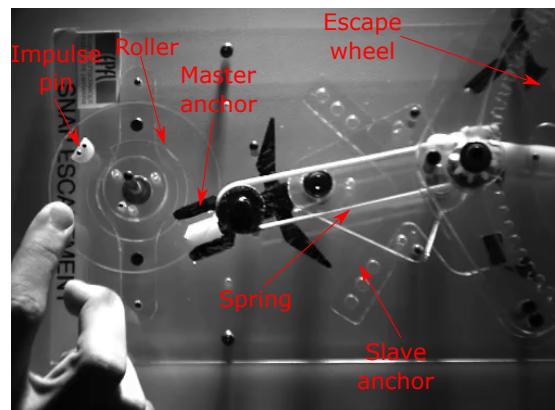


Figure 5.30 – Top view of snap escapement - high speed camera

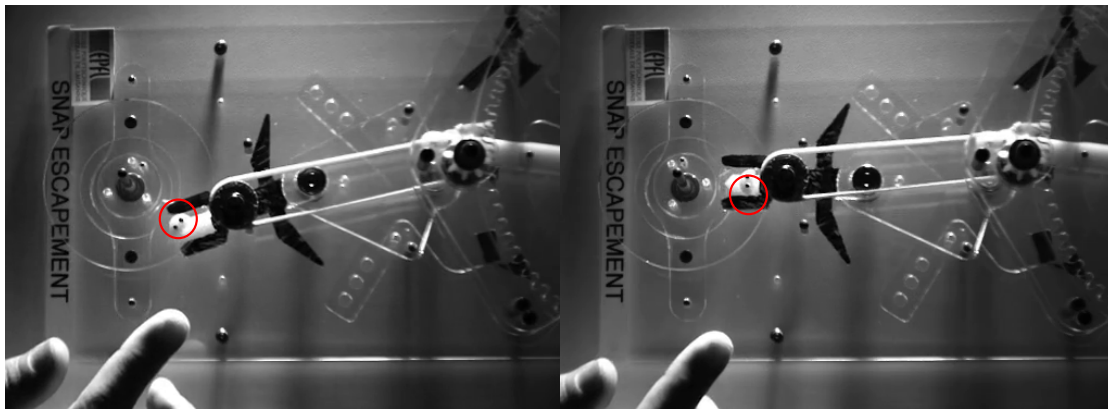


Figure 5.31 – Unlocking of the master anchor

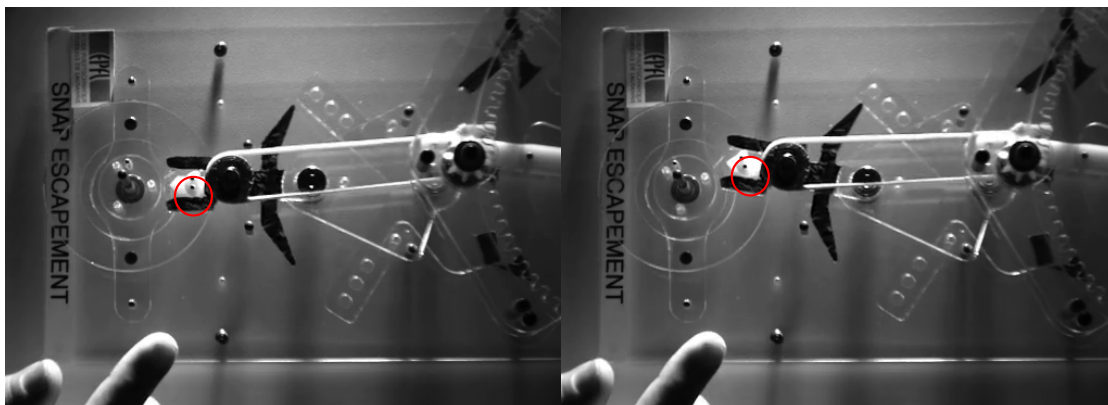


Figure 5.32 – Impulse of the oscillator



Figure 5.33 – Unlocking of the escape wheel

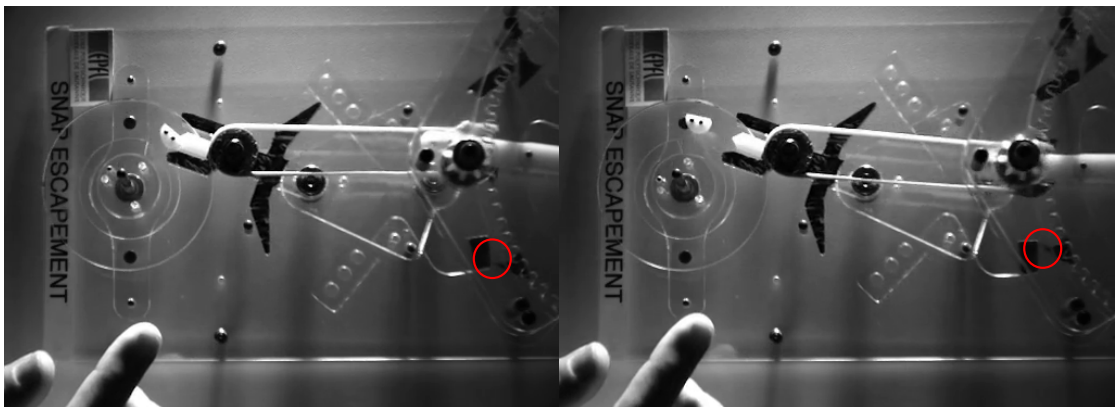


Figure 5.34 – Locking of the slave anchor

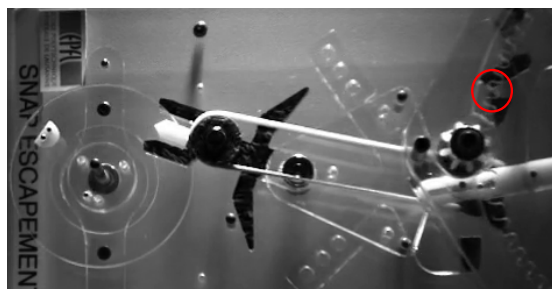


Figure 5.35 – Spring reload

5.5 Conclusion

Programmable multistable mechanisms can release repeatable amount of energy on switching from bistability to monostability. This amount of energy can be used for oscillator impulse to maintain a constant oscillation period. In this chapter, we used the snap mechanism, in addition, the mechanisms introduced in chapters 3-4 can be integrated within the escapement. Figure 5.36 summarizes the possible energy diagrams for programmable multistable mechanisms that can be integrated within constant force escapements.

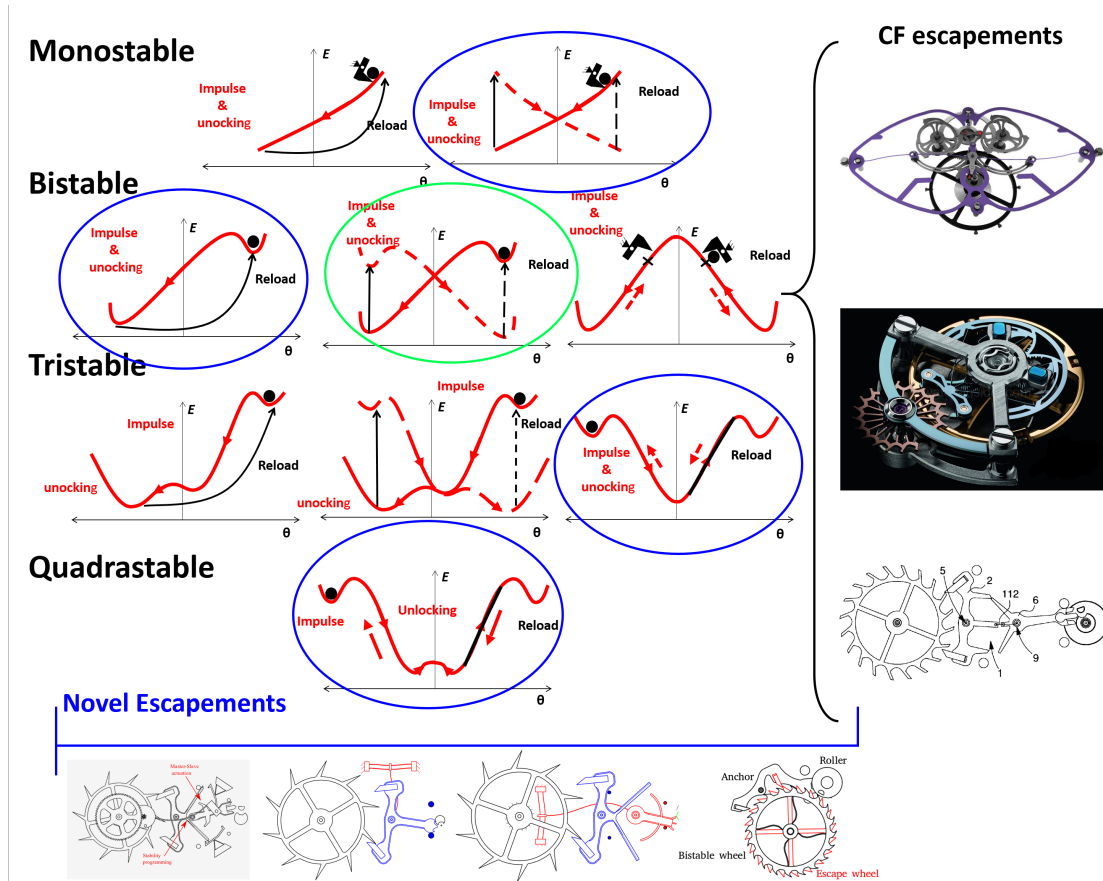


Figure 5.36 – A summary of possible energy curves for constant force escapements and classification of the state of art escapements. Blue ovals are escapements which were studied during the thesis and the green oval gives the energy curve for the escapement presented in this chapter. Escapement on the right side of the figure from top to bottom are Girard-Perregaux escapement, Ulysse Nardin escapement and Nivarox escapement.

6 Application II: Retinal Vein Cannulation *

In this chapter, we present novel medical devices for safe surgical puncturing, in particular a cannula for the treatment of retinal vein occlusion. This passive mechanical device has an adjustable stroke and exerts a puncture force independent of operation applied displacement. The innovative feature of this tool is that puncturing stroke is decoupled from operator input thereby minimizing the possibility of over puncturing. This is achieved using our concept of stability programming, where the user modifies the mechanism strain energy as opposed to imposing direct displacement which is the case for standard bistable mechanisms. Ultra fast laser 3D printing is used to manufacture the needle in glass. A microfluidic channel is integrated into the needle tip for drug injection. Numerical simulations and experimental measurements validate the mechanical stability behavior of the puncture mechanism and characterize its puncturing force and stroke.

6.1 Introduction

Human body puncturing is a common surgical process having associated risks, namely *over puncturing* where the puncture tool overshoots its target. The tool becomes ineffective and bleeding or even death may occur. A survey of the impact of over-puncturing is given in Ref. [105].

For the purpose of this work, *puncturing* means entering a region surrounded by a boundary having a higher penetration resistance. Over puncturing typically occurs because the force used to cross the boundary accelerates the puncturing device and the resulting speed in the low resistance region makes it overshoots the intended target. The challenge, therefore, is to limit the stroke of the puncturing device.

The stroke of the puncture device can be decomposed into surgeon displacement and tool displacement, that is displacement of tool moving parts. Surgeon displacement relies on the

* Some of the content of this chapter has been submitted for publication to the ASME Journal of Medical Devices as Zanaty et al., "Programmable Multistable Mechanisms for Safe Surgical Puncturing."

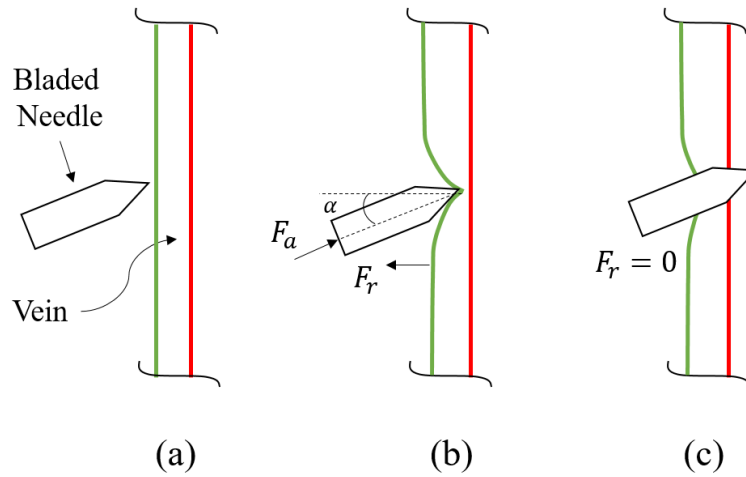


Figure 6.1 – Vein over puncturing: F_a and F_r represents the applied and resistance force and α is the puncturing angle.

human capacity to exert a sufficient puncturing force followed by limiting the stroke. For delicate operations, human performance may not be sufficiently reliable.

Standard puncturing devices such as trocars, have no moving parts, so force and stroke depend on human performance. As explained above, an overly large stroke occurs when there is a large puncturing force, so trocars have a sharp bladed tip to reduce puncturing force. However, this increases the consequences of the over puncturing [106]. Current research is examining robotic surgery which eliminates tremor and limits stroke [107] [108] [109].

Another approach is to integrate movable parts into the tool. These tools can be classified into two groups. The first consists of retractable devices where the puncturing tip retracts once puncturing occurs [110], [111]. These have proven difficult to scale down to satisfy micro surgical requirements. The second group consists of limited stroke devices [112]. This type of devices will be the subject of this work. We will show that this technique can be adapted to micro surgery, in particular *retinal vein cannulation*.

6.1.1 Retinal vein cannulation (RVC)

Vein cannulation is an example of delicate micro puncturing. It further requires drug injection so classical trocars can not be used. A needle punctures the vein and halts inside for the injection duration. In this case, overpuncturing leads to incorrect injection as illustrated in Figure 6.1. Cannulation becomes more difficult with decreasing vein size as puncturing force approaches the limits of human performance. One of the most challenging cases is eye surgery.

Retinal vein occlusion (RVO) is an eye condition at which the retinal vein is blocked, reducing oxygen delivery to the retina [113]. This can lead to macular edema, retinal cells death and

neovascularization, all resulting in vision loss [114]. RVO affects 16 million worldwide with more prevalence among the elderly [113].

RVC is a delicate treatment of RVO [114] and has been proven to be effective. It consists of the following steps, illustrated in Figure 6.2.

1. The needle contacts the vein.
2. The needle punctures the vein and halts.
3. Injection is made.
4. The needle is retracted.

An optical microscope is used to provide visual feedback to the surgeon. It informs the surgeon of puncturing occurrence and drug injection.

Remark. In the case of veins, over-puncturing means puncturing the opposite wall of the vein, so increasing the puncturing angle reduces the possibility of over puncturing, see Figure 6.1.

6.1.2 Challenges of RVC

Technical difficulties of RVC include

1. The diameter of the needle tip must be less than the retinal vein diameter which can vary from 50 to 400 microns.
2. The needle should be sufficiently sturdy to handle the puncturing process.
3. Safe puncturing force can be less than 50[mN], beyond human sensing capability. This can require a force sensor.
4. A gradual force increase can displace the vein instead of puncturing it.
5. Human tremor is of the order of 100 microns, possibly greater than vein diameter.
6. The tool should maintain its position during injection which may exceed 10 minutes.
7. The entire RVC device should fit into a cylinder of 0.9[mm] diameter (20 gauge).

Glass micropipettes with sharp tips are commonly used [115], but they can fracture during puncturing. Stainless steel needles with a curved tip have been used [107], but they do not fit in a 20 gauge cylinder. Pre-bent flexible stainless needles have been proposed [108], but they require extra steps to cannulate the vein. A snake-like cannula is presented in Ref. [116], however, it requires a precise nano-scale motors for controlling the cannula position.

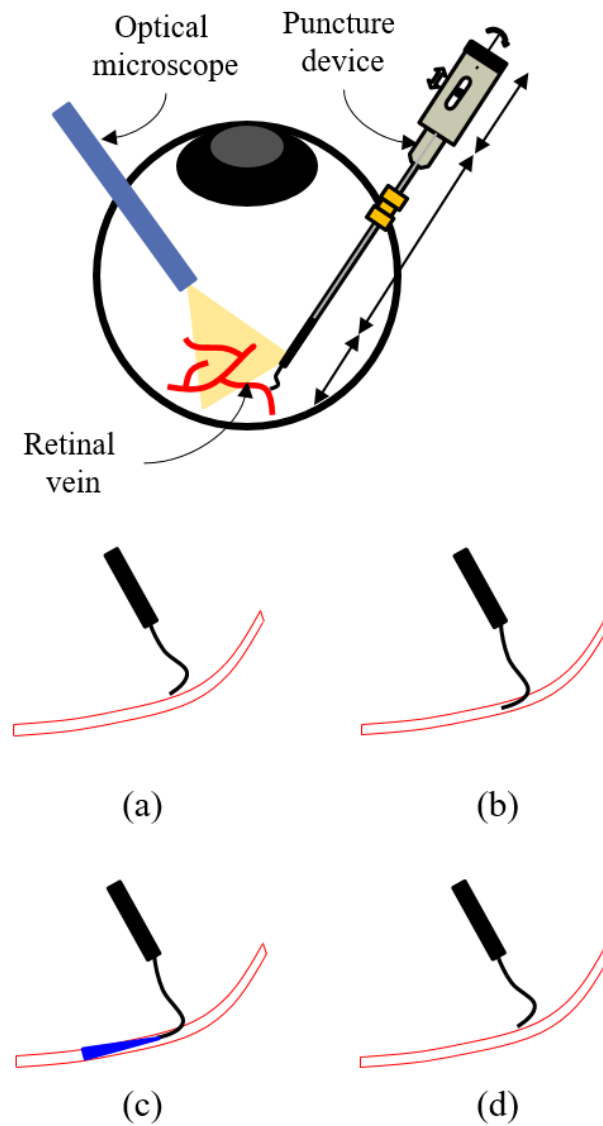


Figure 6.2 – Retinal vein cannulation, (a) needle in contact with the vein, (b) needle punctures the vein, (c) injection is made, (d) needle retracts from the vein.

6.2 Safe puncture optimized tool for RVC

The main result of this chapter is a new passive mechanical puncture tool, the *Safe Puncture Optimized Tool* (SPOT). Compliant micro mechanisms are integrated within the cannula to limit its stroke independent of surgeon displacement. The main novelty is the application of *stability programming*, a concept introduced in our previous work [89]. This allows the stroke of the tool to be adjusted mechanically to a fixed value and be decoupled of the operator displacement.

Figure 6.3 gives the main components of the puncture tool including handle, shaft and puncture mechanism. The handle has two inputs at which the surgeon applies p_1^a and p_2^a . These inputs are converted to micro-scale as, p_1 , p_2 , and transferred to the puncture mechanism via shafts. The input p_1 adjusts the tool stroke based on the vein diameter and p_2 triggers the puncturing.

The puncture mechanism has two stable states, pre-puncturing and post-puncturing states given in Figure 6.4 (a), (b) respectively. At $p_2 = p_2^r$, the mechanism switches from the pre-puncture to the post-puncture state and puncturing occurs. In this chapter, we focus only on the design of the puncture mechanism given in Figure 6.3(d).

6.2.1 Utilization protocol

The surgeon uses the following protocol to cannulate the retinal vein using a visual feedback from the microscope.

1. The value of p_1 determines the stroke which is adjusted by rotating a disc, see Figure 6.3.
2. The surgeon selects an initial value $p_1 = p_1^d$ based on the vein diameter, so that the tool will not over puncture, see Figure 6.17.
3. The tool is initially at its pre-puncturing state.
4. The surgeon uses optical feedback to place the tool tip in contact with the vein.
5. In order to change the puncturing state, the surgeon modifies p_2 using a slider on the tool handle, see Figure 6.3.
6. The surgeon pushes the p_2 slider until visual feedback indicates that the tool is at its post-puncturing state.
7. Using visual feedback, the surgeon determines if puncturing has occurred.
 - 7a. If puncturing occurs without over-puncturing, the procedure is successful.
 - 7b. If over-puncturing has occurred, then, the procedure has failed.

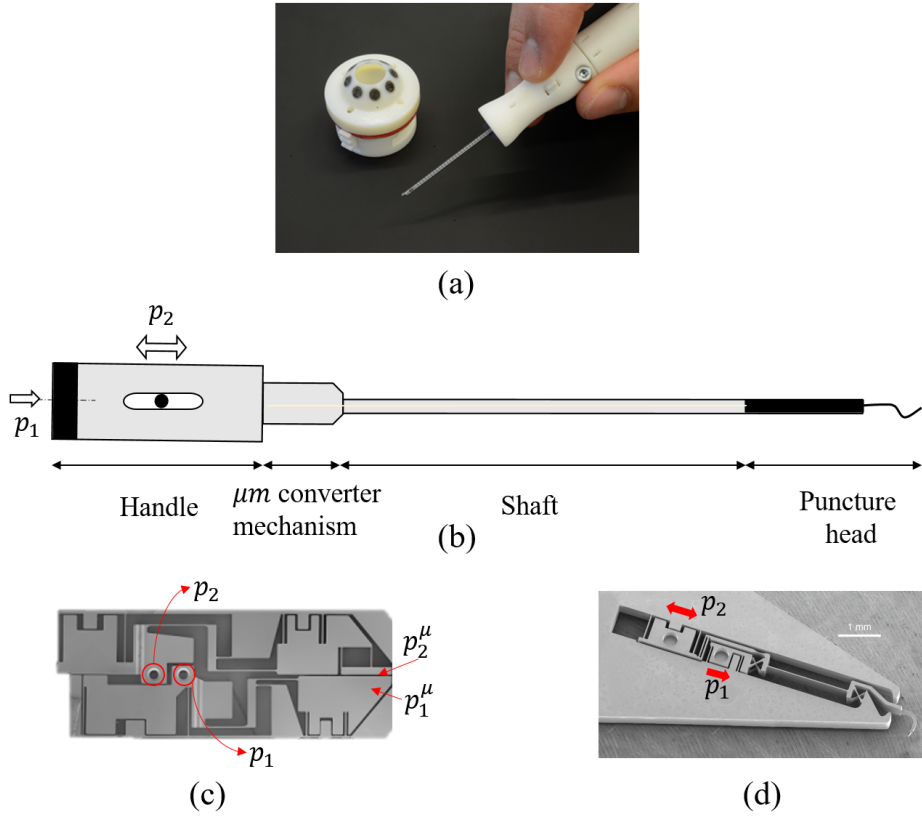


Figure 6.3 – (a) Our tool, (b) graphical representation, (c) micro-converter mechanism, (d) puncture mechanism.

- 7c. If puncturing has not occurred, the surgeon pulls the p_2 slider till the tool reaches its pre-puncturing state, the surgeon slightly increases p_1 and returns to step 6.

In the case of successful puncturing, the cannulation is continued by drug injection. Following injection, the surgeon pulls the p_2 slider returning the tool to its pre-puncturing state and removes the tool from the eye.

6.2.2 Theoretical design

Mechanical multistability

Our tool relies on the concept of multistability to produce repeatable puncturing with tunable stroke. Multistable mechanisms are mechanical devices which have more than one stable state within their range of motion [76]. They store and release strain energy as they deform under imposed displacement x or force F . They can function as switch when displaced between their stable states, and characterized by their rapid energy release once they surpass their unstable state. A simple example is the bistable mechanism as realized by a hair clip.



(a)



(b)

Figure 6.4 – Stable states of the mechanism for $p_1 = 10[\mu m]$, puncturing occurs on switching from (a) pre-puncturing state to (b) post-puncturing state.

Multistable mechanisms are used to improve the safety of medical operations such as cranial drilling as they rapidly release energy on surpassing their unstable state. This was utilized to prevent over drilling [111].

Definitions

The strain energy of multistable mechanisms has N energy minima corresponding to *stable states*, s_1, s_2, \dots, s_N and $N - 1$ energy maxima representing *unstable states*, u_1, u_2, \dots, u_{N-1} , as illustrated in the strain energy in Figure 6.5(a), where $N = 2$. Energy is required to surpass the *barrier* (ΔE) existing between the stable states.

We distinguish two categories of multistable mechanisms based on the actuation method, the first category is *displacement driven multistable mechanisms* in which the position is altered without modifying the energy profile and *programmable multistable mechanisms* in which the energy profile is modified by the displacement imposed.

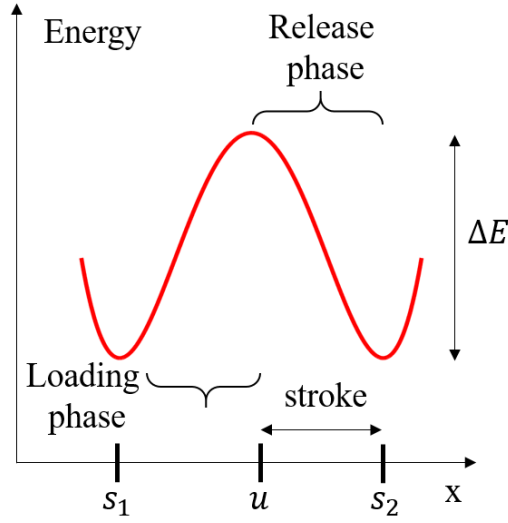


Figure 6.5 – Strain energy of displacement driven bistable mechanism as function of its position x .

Displacement driven bistable mechanism

One degree of freedom (DOF) bistable mechanisms can be displaced between their stable states by imposing direct displacement to modify their position x , as illustrated in Figure 6.5. As x increases from stable state s_1 , the stored strain energy increases until the mechanism reaches its unstable state u , we call this the *loading phase*. After that, the mechanism releases its stored energy till it reaches its other stable state s_2 , we call this the *release phase*. Since the energy profile is fixed, the exerted force during the release phase is repeatable for the given stroke, as illustrated by the reaction force in Figure 6.5(b).

In order to reach the release phase, the operator must displace the mechanism up to a displacement $x_u > u$, we call this *overloading*. During overloading the operator applies a force thereby adding energy to the system which increases the stroke. This means that repeatability of the energy release depends on the repeatability of x_u , which is difficult if $x_u - u$ is of the order of human sensory perception. Figure 6.6 illustrate the impact of overload on the mechanism position where the ball represents the mechanism state.

For human driven micro-scale devices, displacement driven multistable mechanisms do not have a high degree of repeatable energy release and stroke. Therefore, imposed displacement and the mechanism position should be decoupled, this can be implemented by programmable multistable mechanisms.

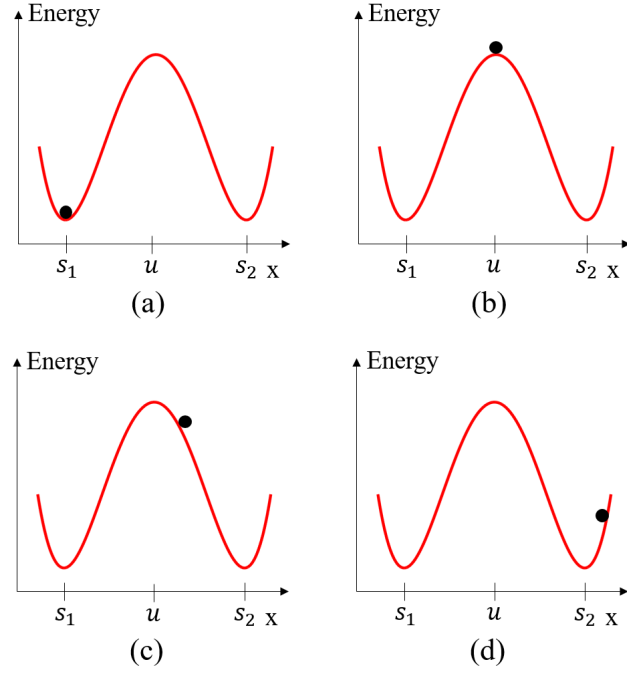


Figure 6.6 – Strain energy of displacement driven bistable mechanism where the mechanism position is denoted by the ball at (a) stable state s_1 , (b) unstable state u with no overload $x_u = 0$, (c) overload $x_u > 0$, (d) overload after surpassing s_2 .

Programmable multistable mechanism

Programmable multistable mechanisms (PMM) have an energy profile modified by external inputs that we call *programming inputs*. These inputs can change the number and position of stable states as well as trigger energy release. In this chapter, we consider only the case of stability programming between monostability and bistability.

Figure 6.7 gives the strain energy of the programmable multistable mechanism used in our tool. We describe the energy profiles corresponding to the protocol steps given in Section 2.1. Once again the ball represents the state.

Initially the mechanism is monostable as given in Figure 6.7(a) corresponding to Step 1. As p_1 is increased, the mechanism becomes bistable and the stroke is tuned by selecting $p_1 = p_1^d$ of Step 2, as illustrated in Figure 6.7(b). The mechanism is in state s_1 .

Step 6 corresponds to Figures 6.7(c)-(f). As p_2 is increased, the energy profile remains bistable until $p_2 = p_2^s$ as shown in Figure 6.7(c). The mechanism remains in state s_1 during this step (the variation of s_1 with respect to p_2 is negligible).

At p_2^s , the mechanism is once again monostable with stable state s_2 , as illustrated in Figure 6.7(d). As p_2 is further increased, there is a value p_2^r at which the mechanism overcomes

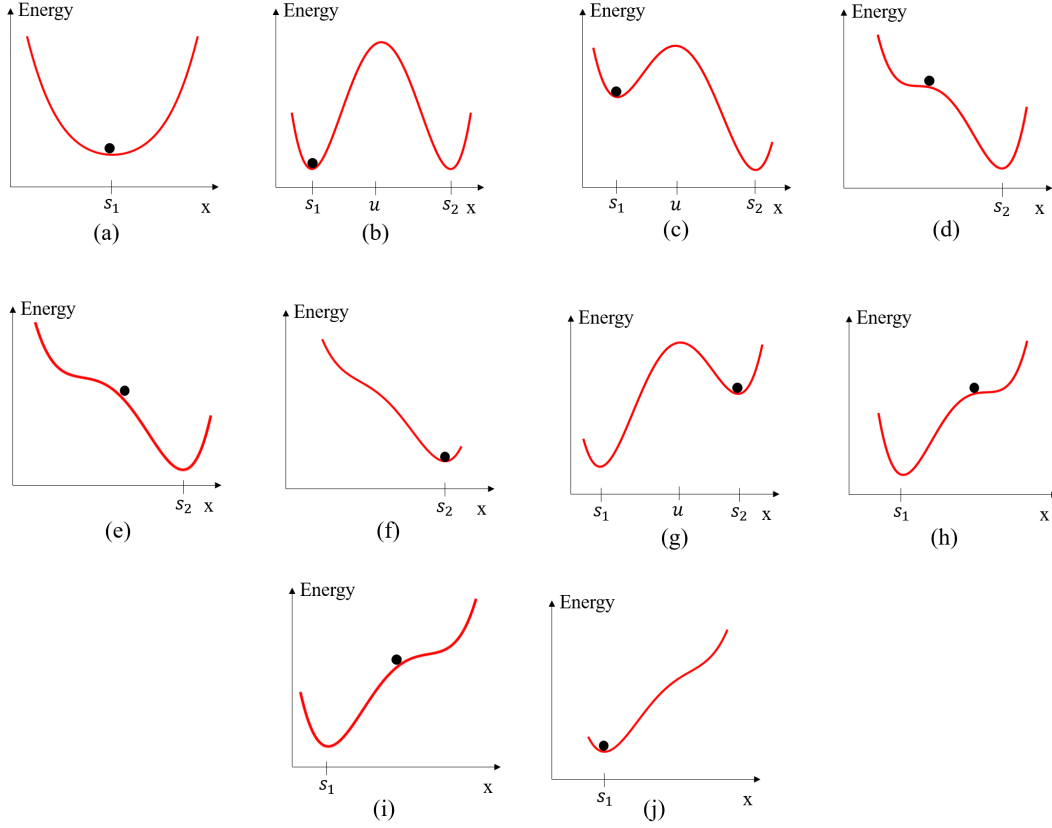


Figure 6.7 – Strain energy of programmable bistable mechanism for different values of p_1 , p_2
 (a) $p_1 < p_1^{cr}$, (b) $p_1 > p_1^{cr}$, $p_2 = 0$, (c) $p_1 > p_1^{cr}$, $0 < p_2 < p_2^s$, (d) $p_1 > p_1^{cr}$, $p_2 = p_2^s$, (e) $p_1 > p_1^{cr}$, $p_2 = p_2^r$, (f) $p_1 > p_1^{cr}$, $p_2 > p_2^r$, (g) $p_1 > p_1^{cr}$, $-p_2^s < p_2 < 0$, (h) $p_1 > p_1^{cr}$, $p_2^s < p_2 < 0$, (i) $p_1 > p_1^{cr}$, $p_2 = -p_2^r$, (j) $p_1 > p_1^{cr}$, $p_2 < -p_2^r$.

static damping and starts to release energy, see Figure 6.7(e).

Energy release rapidly displaces the mechanism to state s_2 independent of p_2 overload as shown in Figure 6.7(f). Further increase of p_2 slightly affects the position of the mechanism.

Step 7c corresponds to Figures 6.7(g)-(i), simply reversing the steps illustrated in Figure 6.7(c)-(e) by decreasing p_2 .

Key remark. Figure 6.7(e) always occurs at the same value p_2^r , so energy release is repeatable and stroke is decoupled from operator actuation input.

6.2.3 Tool design

We chose a programmable multistable mechanism having the energy profiles in Figure 6.7. The conceptual design is shown in Figure 6.8 and our physical construction satisfies the

requirements of retinal vein cannulation discussed in Section 1.3.

A conceptual design

A conceptual representation of our tool is given in Figure 6.8, it consists of a beam anchored on both sides via pivots. The *puncturing pivot* is connected to the needle tip and fixed to the tool frame. The body of the *actuation pivot* translates according to p_1 in the axial direction of the beam.

The input p_2 acts by translating a slider which loads a *programming spring* translating an intermediate block which in turn rotates the actuation pivot via a rigid link. The angular position α^a of the actuation pivot determined by p_2 leads to an angular deflection α^p of the puncturing pivot.

When $p_1 = 0$, the beam is straight so $\alpha^a = \alpha^p = 0$. As p_1 increases, it remains straight until $p_1 > p_1^{cr}$ when the beam buckles. Further increase of p_1 increases the strain energy and leads to higher energy release. A suitable value is chosen, e.g., p_1^d , as discussed in Section 2.1.

The buckled beam has two stable states corresponding to the pre-puncturing and post-puncturing states, having angular deflections α_1^a, α_1^p and α_2^a, α_2^p , respectively.

Starting at the pre-puncturing state, α_1^a, α_1^p , puncturing occurs by increasing p_2 which rotates the actuation pivot clockwise. The mechanics of the double pinned buckled beam is such that the puncture pivot rotates imperceptibly, so that α^p has essentially the same value α_1^p [117]. On reaching p_2^r of Section 2.2.4, the mechanism releases its energy and rapidly reaches its post-puncturing state and α_1^p switches to α_2^p , this corresponds to the puncturing phase.

Flexure-based realization

The equivalent flexure mechanism of our conceptual design is given in Figure 6.9. It consists of a beam anchored on both extremities by 3D cross pivots corresponding to the double pinned beam. Each pivot has three overlapped beams with optimized profile to increase their stroke as illustrated in Figure 6.10. The needle tip is connected to the puncture pivot and contains a fluidic channel for drug injection as shown in Figure 6.11.

The actuation pivot is guided by a parallel beam stage at which p_1 is imposed. The input p_2 is applied on a parallel beam stage which is connected serially to the programming spring which consists of two beams. The programming spring is serially connected to the actuation pivot via a circular hinge. Stoppers are used to limit the range of p_1, p_2 and puncture angle α_p .

Tool advantages

Our mechanism has the following advantages for retinal vein cannulation.

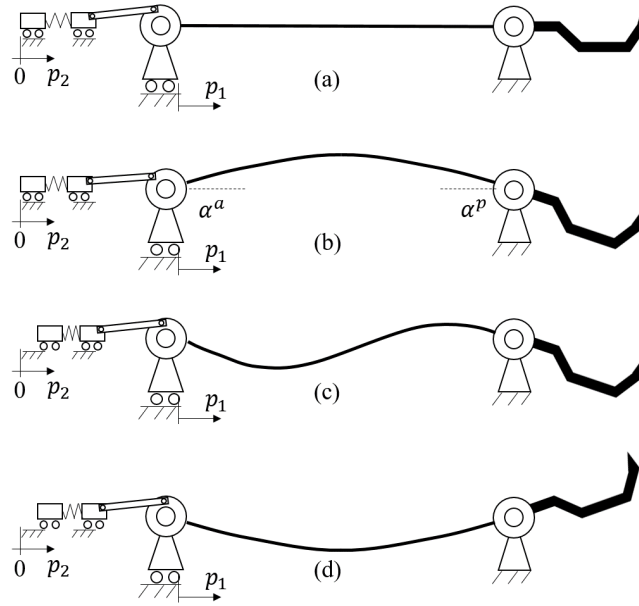


Figure 6.8 – Mechanism deformation for (a) initial state, (b) pre-puncturing state, (c) unstable state, (d) post-puncturing state.

1. Multistable mechanisms release their energy rapidly, thereby addressing standard cannulation problems (Section 1.3).
2. The stroke of the tool is independent of surgeon actuation during puncturing, thereby decreasing the possibility of overpuncturing (Section 2.2.4).
3. Tool stroke can be adjusted by the surgeon prior to puncturing making the tool adaptable to different vein sizes. Moreover, this allows gradual stroke increase for a given vein, thereby minimizing the possibility of overpuncturing (Section 2.1).
4. The needle tip has non significant movement during the loading phase, thereby, decreasing the variability of the tool positioning (Section 2.2).
5. The maximum force exerted by the tool is adjustable, thereby eliminating the need for a force sensor (Section 1.3).
6. Once inside the vein, the needle position is stable making this suitable for long injection periods exceeding 10 minutes (Section 1.3).

6.3 Dimensioning

We used the finite element method to dimension the mechanism. COMSOL solid mechanics module was selected to calculate the mechanism strain energy in terms of programming

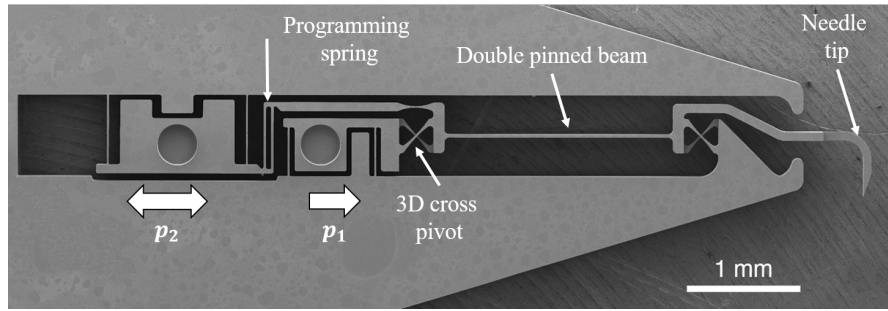


Figure 6.9 – The puncture mechanism illustrating its main components and the programming inputs, p_1 , p_2 .

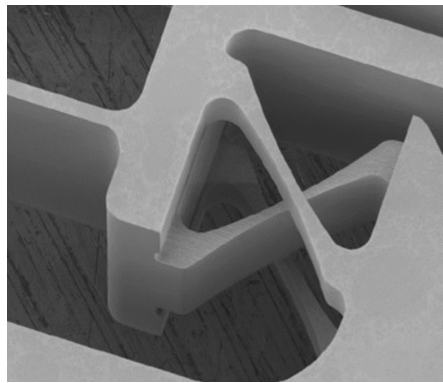


Figure 6.10 – A 3D cross pivot for beam anchoring.

inputs, thereby estimating the tool stroke. Mesh convergence tests were performed to ensure solution validity.

The mechanism dimensions were selected to satisfy the specifications of Section 1.3: a programmable stroke from $5[^\circ]$ to $20[^\circ]$ and a puncturing force exceeding $8[mN]$.

Our FEM simulations showed that these specifications are satisfied when the double pinned beam has length $2[mm]$, thickness $30[\mu m]$, width $200[\mu m]$ and the programming spring consists of two identical beams, each of length $500[\mu m]$ and thickness $25[\mu m]$.

6.4 Fabrication

We used fused silica (glass) as our tool material since its elastic properties are consistent with the tool specifications. A femto-laser etches fused silica whose transparency at the selected wavelength allows laser penetration. The laser is absorbed where focused changing the material properties, in particular, the etching rate, which is 200 times higher in exposed regions than in unexposed regions. Accordingly, the tool dimensions were adapted to the different etching rates. This allowed us to satisfy the tight fabrication tolerances, which are of order $1[\mu m]$.

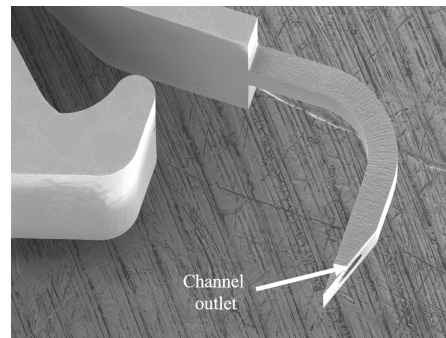


Figure 6.11 – The needle tip with an integrated fluidic channel for drug injection.

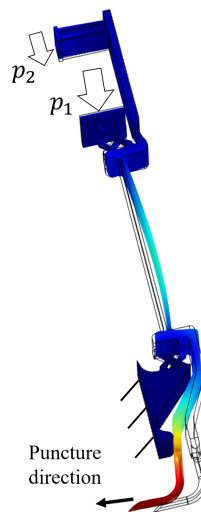


Figure 6.12 – 3D rendering of the deformation of the puncture mechanism based on FEM simulations.

We exposed a $500[\mu m]$ thick fused silica to a $1030[nm]$ femto-second laser focused by a $20X$ Objective 0.4 numerical aperture lens. Exposure took 30 minutes and the etching lasted 8 hours. The tool was manufactured in collaboration with FemtoPrint SA using their innovative technology [118, 119, 120].

6.5 Characterization

The mechanical behavior of the puncture tool is studied including the mechanism stroke, puncturing force, number of stable states and their positions. An experimental setup is built to verify the mechanical behavior of the tool. The tool functionality was tested by the cannulation of the retinal vein of pig eyes.

6.5.1 Experimental measurements

We validate numerically and experimentally the stability behavior of the tool, i.e., we evaluate the number and positions of the stable states for given programming inputs. Then, we study the effect of the programming inputs on the mechanism stroke and puncture force, the crucial parameters for successful puncturing.

An experimental setup was built to characterize the mechanical behavior of the puncture tool. The spatial position of the puncture tool was controlled by a 5-DOF stage as illustrated in Figure 6.13. Programming inputs were applied by micro-metric screws and their values were measured using an optical microscope of resolution $0.5[\mu m]$. A Futek LPM 200 load cell with resolution of $0.1[mN]$ was used to measure puncturing force of the needle tip.

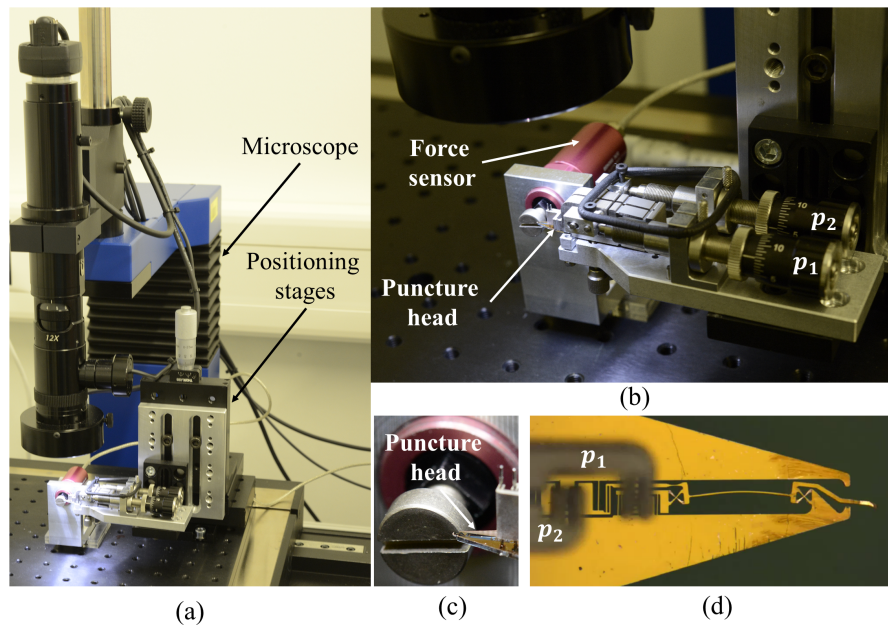


Figure 6.13 – (a) Experimental setup, (b) Driving micro-metric screws and force sensor, (c) Interface between the sensor and the needle tip, (d) The puncture mechanism under microscope.

6.5.2 Results and discussion

The number of stable states as a function of the programming inputs is illustrated by the *programming diagram*, as shown in Figure 6.15. This characterizes the qualitative behavior of the mechanism.

The set of values (p_1, p_2) is divided into regions where the mechanism is monostable versus bistable. As explained in Section 2.2, the boundaries between these regions corresponds to p_2^r which depends on p_1 .

We also explicitly computed and experimentally validated the energy profiles for given values (p_1, p_2) . In particular, Figure 6.14 shows how for $p_1 = 15[\mu m]$, the energy profile changes for a given set of p_2 values. This corresponds to puncturing as explained in Section 2.2. It is seen that the qualitative nature of energy profile is consistent with the discussion of Section 2.2.

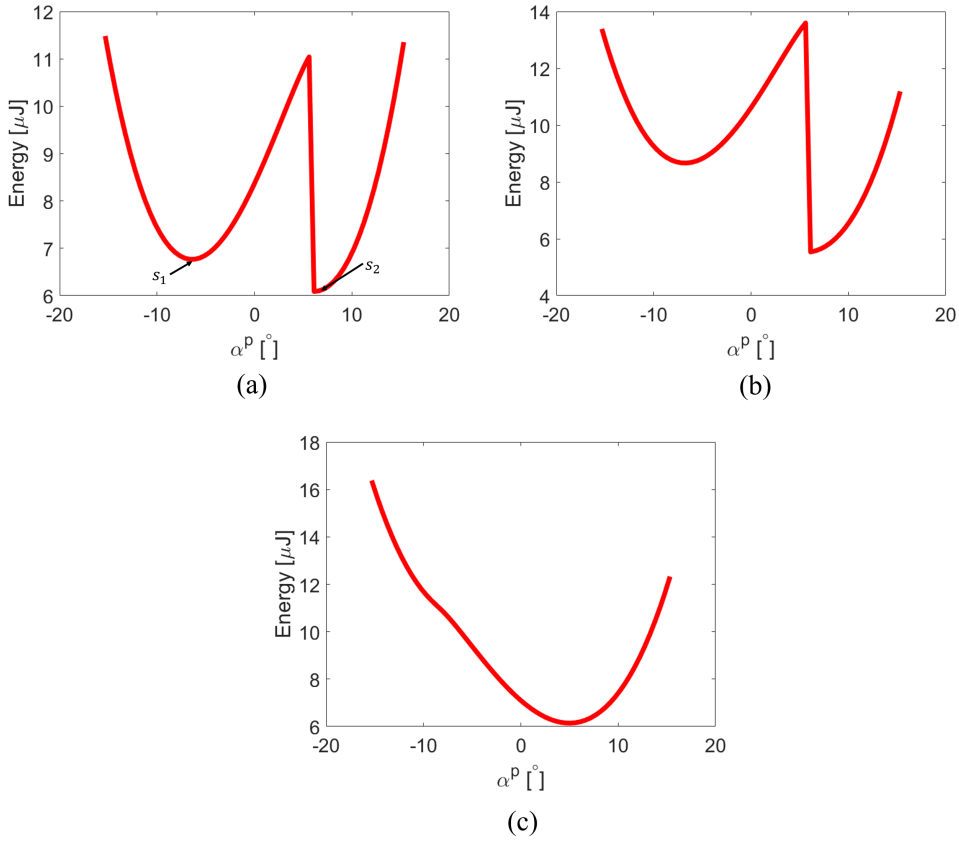


Figure 6.14 – Strain energy of the puncture mechanism for $p_1 = 15[\mu m]$ on switching from pre-puncturing state s_1 to post-puncturing state s_2 based on FEM simulations.

An advantage of our tool is decoupling the surgeon actuation input p_2 and the puncture pivot position α^p before and after energy release as illustrated in Figure 6.16 for $p_1 = 15[\mu m]$. As p_2 changes, α^p is slightly modified. At $p_2 = p_2^r$, the mechanism snaps to its post-puncturing

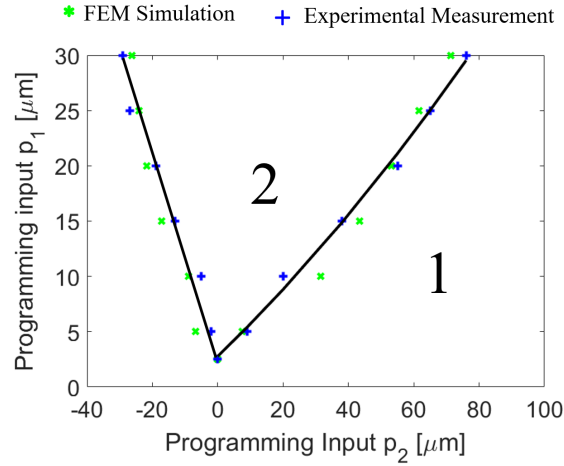


Figure 6.15 – Programming diagram giving the relation between the number of stable states and programming inputs.

state. The value at which the mechanism switches between its stable states depends on the direction of the applied p_2 .

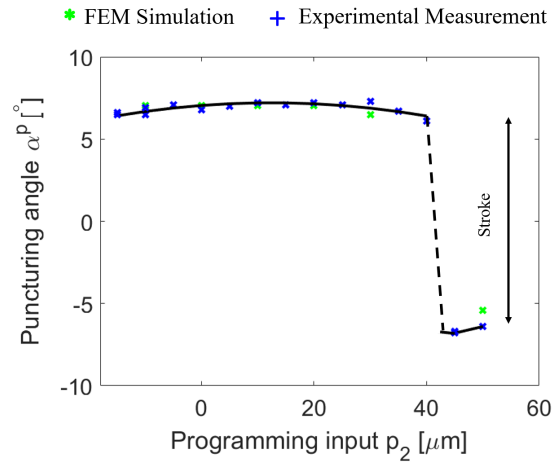


Figure 6.16 – The angular position of the needle tip as function of p_2 at $p_1 = 15[\mu\text{m}]$ based on numerical and experimental measurements.

We validated the ability to tune stroke using p_1 . Figure 6.17 illustrates the relation between the stroke and p_1 . This shows that the stroke increases with p_1 ensuring that a significant range of strokes is possible making the tool adaptable to different vein diameters. In addition, Figure 6.18 shows that the maximum force at the needle tip increases with increasing p_1 where quasi-static measurement conditions are applied.

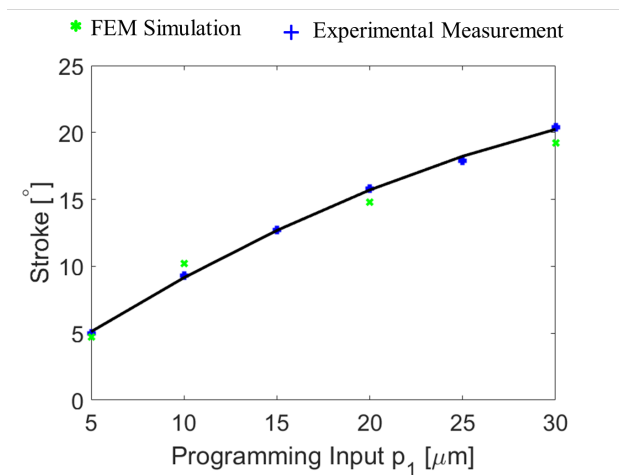


Figure 6.17 – The angular stroke of the needle tip versus p_1 based on numerical and experimental measurements.

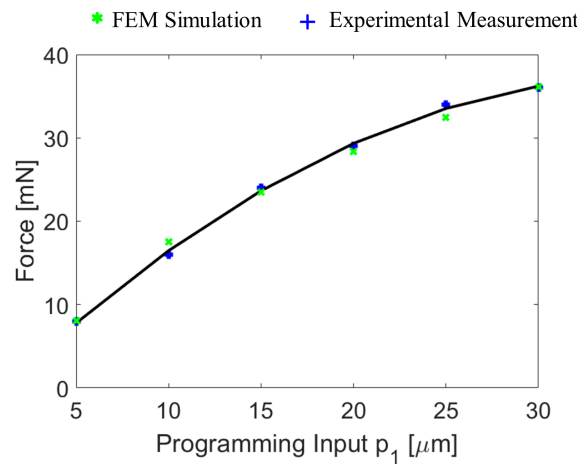


Figure 6.18 – The maximum force during energy release in quasi-static mode versus p_1 based on numerical and experimental measurements.

6.5.3 Pig eye testing

We used pig eyes to verify the functionality of the tool. The retinal vein of pig eyes was successfully cannulated. We used optical microscope and high speed camera to verify the vein cannulation as illustrated in Figure 6.19.

The pig eyes were prepared as follows. We divided the eye into two parts so that the retina is easily accessed without being deformed. Second, we removed the vitreous humour by capillary forces so we can verify the puncturing occurrence. After that, the puncture tool was positioned using the 5-DOF stage so that the needle was in contact with the vein at its pre-puncturing state. Micrometric screws were used to program and trigger the puncturing. A Leica M125 stereo microscope was used to assess the needle tip position.

The minimum vein diameter successfully cannulated is $150[\mu m]$. This limitation is returned to the accuracy of the positioning stage and vein motion during the tool loading phase of the tool.

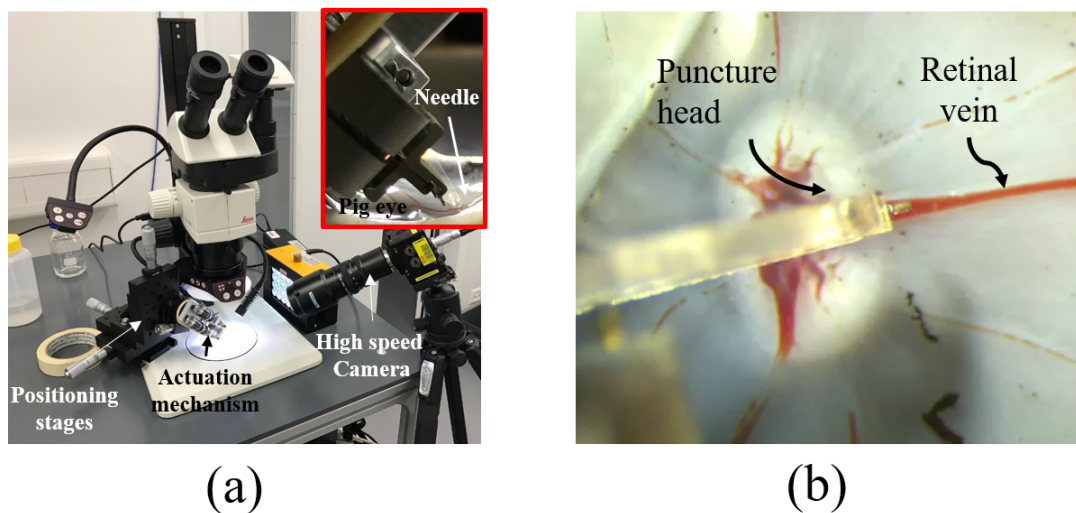


Figure 6.19 – (a) Pig eye cannulation setup, (b) puncture mechanism in contact with the retinal vein.

6.6 Conclusion and perspectives

We applied our concept of stability programming to design retinal vein cannulas for the treatment of vein occlusion.

Our theoretical analysis indicates that stability programming can advantageously decouple operator input from instrument position enabling safe puncturing.

Our tool appears to be one of the first examples of complicated 3D structures manufactured

Chapter 6. Application II: Retinal Vein Cannulation

by ultra-fast laser printing in glass highlighting the great potential of this technology.

Our current research applies programmable multistable mechanisms to other medical operations requiring delicate procedures.

7 Contributions and Perspectives

7.1 Contributions

The main contributions of this thesis are

1. Introduction of programmable multistable mechanisms (PMMs).
2. Analytical and numerical modeling of a generic PMM with experimental validation.
3. Complete qualitative description of the stability behavior of a generic PMM.
4. Application of PMMs to watches with new constant force escapements.
5. Application of PMMs to surgical tool with a novel ophthalmological device.
6. Demonstration that femto-laser 3D printing can fabricate non-planar compliant microstructures out of glass.

7.2 Perspectives

My current research concerns applications of my thesis to metamaterials.

As opposed to naturally existing materials whose building blocks are atoms, a metamaterial has artificial building blocks, known as meta-atoms, whose design can tune the metamaterial's global properties.

Using PMMs as meta-atoms, we develop a new family of metamaterial which we call *programmable metamaterials*. In this way, we can tune elastic properties such as Young's modulus, Poisson ratio, shear modulus to have non naturally occurring values.

Bibliography

- [1] S. H. Strogatz, *Nonlinear dynamics and chaos: with applications to physics, biology, chemistry, and engineering*. Westview press, 2014.
- [2] L. P. Pook, *Understanding pendulums: a brief introduction*, vol. 12. Springer Science & Business Media, 2011.
- [3] A. M. Lyapunov, “The general problem of the stability of motion,” *International journal of control*, vol. 55, no. 3, pp. 531–534, 1992.
- [4] L. L. Howell, *Compliant mechanisms*. John Wiley & Sons, 2001.
- [5] S. P. Timoshenko and J. M. Gere, “Theory of elastic stability,” *McGrawHill-Kogakusha Ltd, Tokyo*, 1961.
- [6] M. Saif, “On a tunable bistable MEMS-theory and experiment,” *Journal of Microelectromechanical Systems*, vol. 9, pp. 157–170, June 2000.
- [7] N. Dehon, “Mecanisme d’échappement,” Sept. 30 2009. EP Patent App. EP20,080,153,450.
- [8] D. A. Porter and T. A. Berfield, “A bi-stable buckled energy harvesting device actuated via torque arms,” *Smart Materials and Structures*, vol. 23, no. 7, p. 075003, 2014.
- [9] J. Qiu, J. H. Lang, A. H. Slocum, and R. Strumpler, “A high-current electrothermal bistable mems relay,” in *Micro Electro Mechanical Systems, 2003. MEMS-03 Kyoto. IEEE The Sixteenth Annual International Conference on*, pp. 64–67, IEEE, 2003.
- [10] J. Qiu, J. H. Lang, and A. H. Slocum, “A curved-beam bistable mechanism,” *Microelectromechanical Systems, Journal of*, vol. 13, no. 2, pp. 137–146, 2004.
- [11] S. Park and D. Hah, “Pre-shaped buckled-beam actuators: theory and experiments,” *Sensors and Actuators A: Physical*, vol. 148, no. 1, pp. 186–192, 2008.
- [12] C.-C. Wu, M.-J. Lin, and R. Chen, “The derivation of a bistable criterion for double v-beam mechanisms,” *Journal of Micromechanics and Microengineering*, vol. 23, no. 11, p. 115005, 2013.

- [13] S. Krylov, S. Seretensky, and D. Schreiber, "Pull-in behavior of electrostatically actuated multistable microstructures," in *ASME 2007 International Design Engineering Technical Conferences and Computers and Information in Engineering Conference*, pp. 759–768, American Society of Mechanical Engineers, 2007.
- [14] S. Krylov, S. Seretensky, and D. Schreiber, "Pull-in behavior and multistability of a curved microbeam actuated by a distributed electrostatic force," in *Micro Electro Mechanical Systems, 2008. MEMS 2008. IEEE 21st International Conference on*, pp. 499–502, IEEE, 2008.
- [15] G. Salinas and S. Givli, "Can a curved beam bistable mechanism have a secondary equilibrium that is more stable than its stress-free configuration?," *Microsystem Technologies*, pp. 1–8, 2014.
- [16] J. Zhao, Y. Huang, R. Gao, G. Chen, Y. Yang, S. Liu, and K. Fan, "Novel universal multistable mechanism based on magnetic - mechanical - inertial coupling effects," *IEEE Transactions on Industrial Electronics*, vol. 61, pp. 2714–2723, June 2014.
- [17] U. Sonmez and C. C. Tutum, "A compliant bistable mechanism design incorporating elastica buckling beam theory and pseudo-rigid-body model," *Journal of Mechanical Design*, vol. 130, no. 4, p. 042304, 2008.
- [18] B. D. Jensen and L. L. Howell, "Bistable configurations of compliant mechanisms modeled using four links and translational joints," *Journal of Mechanical Design*, vol. 126, no. 4, pp. 657–666, 2004.
- [19] B. D. Jensen and L. L. Howell, "Identification of compliant pseudo-rigid-body four-link mechanism configurations resulting in bistable behavior," *Journal of Mechanical Design*, vol. 125, no. 4, pp. 701–708, 2003.
- [20] B. D. Jensen, L. L. Howell, and L. G. Salmon, "Introduction of two-link in-plane, bistable compliant mems," in *Proceeding of the 1998 ASME Design Engineering Technical Conferences, DETC98/MECH-5837*, 1998.
- [21] T. Gomm, L. L. Howell, and R. H. Selfridge, "In-plane linear displacement bistable microrelay," *Journal of Micromechanics and Microengineering*, vol. 12, no. 3, p. 257, 2002.
- [22] M. B. Parkinson, B. D. Jensen, and G. M. Roach, "Optimization-based design of a fully-compliant bistable micromechanism," in *ASME 2000 Design Engineering Technical Conference, Paper No. DETC2000MECH-14119*, 2000.
- [23] N. D. Masters and L. L. Howell, "A self-retracting fully compliant bistable micromechanism," *Microelectromechanical Systems, Journal of*, vol. 12, no. 3, pp. 273–280, 2003.
- [24] N. D. Masters and L. L. Howell, "A three degree-of-freedom model for self-retracting fully compliant bistable micromechanisms," *Journal of Mechanical Design*, vol. 127, no. 4, pp. 739–744, 2005.

-
- [25] D. L. Wilcox and L. L. Howell, "Fully compliant tensural bistable micromechanisms (ftbm)," *Microelectromechanical Systems, Journal of*, vol. 14, no. 6, pp. 1223–1235, 2005.
- [26] D. L. Wilcox and L. L. Howell, "Double-tensural bistable mechanisms (dtbm) with on-chip actuation and spring-like post-bistable behavior," in *ASME 2005 International Design Engineering Technical Conferences and Computers and Information in Engineering Conference*, pp. 537–546, American Society of Mechanical Engineers, 2005.
- [27] R. Luharuka and P. J. Hesketh, "Design of fully compliant, in-plane rotary, bistable micromechanisms for mems applications," *Sensors and Actuators A: Physical*, vol. 134, no. 1, pp. 231–238, 2007.
- [28] R. Luharuka and P. J. Hesketh, "A bistable electromagnetically actuated rotary gate microvalve," *Journal of Micromechanics and Microengineering*, vol. 18, no. 3, p. 035015, 2008.
- [29] H. Matoba, T. Ishikawa, C.-J. Kim, and R. S. Muller, "A bistable snapping microactuator," in *Micro Electro Mechanical Systems, 1994, MEMS'94, Proceedings, IEEE Workshop on*, pp. 45–50, IEEE, 1994.
- [30] C. P. Lusk and L. L. Howell, "Spherical bistable micromechanism," *Journal of Mechanical Design*, vol. 130, no. 4, p. 045001, 2008.
- [31] B. H. Hanna, J. M. Lund, R. J. Lang, S. P. Magleby, and L. L. Howell, "Waterbomb base: a symmetric single-vertex bistable origami mechanism," *Smart Materials and Structures*, vol. 23, no. 9, p. 094009, 2014.
- [32] I. Foulds, N. Trinh, S. Hu, S. Liao, R. Johnstone, and M. Parameswaran, "A surface micromachined bistable switch," in *Electrical and Computer Engineering, 2002. IEEE CCECE 2002. Canadian Conference on*, vol. 1, pp. 465–469, IEEE, 2002.
- [33] I. G. Foulds, M. T. Trinh, S. Hu, S. W. Liao, R. W. Johnstone, and M. A. Parameswaran, "New design for surface micromachined bistable and multistable switches," *Journal of Micro/Nanolithography, MEMS, and MOEMS*, vol. 2, no. 4, pp. 255–258, 2003.
- [34] I. Foulds and M. Parameswaran, "Hysteresis spring single digital input bistable mechanism," in *MEMS, NANO and Smart Systems, 2005. Proceedings. 2005 International Conference on*, pp. 455–458, July 2005.
- [35] B. Goessling, T. Lucas, E. Moiseeva, J. Aebersold, and C. Harnett, "Bistable out-of-plane stress-mismatched thermally actuated bilayer devices with large deflection," *Journal of Micromechanics and Microengineering*, vol. 21, no. 6, p. 065030, 2011.
- [36] Y. Oh, *Synthesis of multistable equilibrium compliant mechanisms*. PhD thesis, Umich, 2008.

Bibliography

- [37] Y. S. Oh and S. Kota, "Synthesis of multistable equilibrium compliant mechanisms using combinations of bistable mechanisms," *Journal of Mechanical Design*, vol. 131, no. 2, p. 021002, 2009.
- [38] G. Chen, D. L. Wilcox, and L. L. Howell, "Fully compliant double tensural tristable micromechanisms (DTTM)," *Journal of Micromechanics and Microengineering*, vol. 19, no. 2, p. 025011, 2009.
- [39] G. Chen and Y. Du, "Double-young tristable mechanisms," *Journal of Mechanisms and Robotics*, vol. 5, no. 1, p. 011007, 2013.
- [40] J. S. Han, C. Mazller, U. Wallrabe, and J. G. Korvink, "Design, simulation, and fabrication of a quadstable monolithic mechanism with x-and y-directional bistable curved beams," *Journal of Mechanical Design*, vol. 129, no. 11, pp. 1198–1203, 2007.
- [41] G. Chen, Q. T. Aten, S. Zirbel, B. D. Jensen, and L. L. Howell, "A tristable mechanism configuration employing orthogonal compliant mechanisms," *Journal of Mechanisms and Robotics*, vol. 2, no. 1, p. 014501, 2010.
- [42] G. Chen, Y. Gou, and A. Zhang, "Synthesis of compliant multistable mechanisms through use of a single bistable mechanism," *Journal of Mechanical Design*, vol. 133, no. 8, p. 081007, 2011.
- [43] Y. Gerson, S. Krylov, B. Ilic, and D. Schreiber, "Design considerations of a large-displacement multistable micro actuator with serially connected bistable elements," *Finite Elements in Analysis and Design*, vol. 49, no. 1, pp. 58–69, 2012.
- [44] T. M. Pendleton and B. D. Jensen, "Compliant wireform mechanisms," *Journal of Mechanical Design*, vol. 130, no. 12, p. 122302, 2008.
- [45] G. Chen, Y. Liu, and Y. Gou, "A compliant 5-bar tristable mechanism utilizing metamorphic transformation," in *Advances in Reconfigurable Mechanisms and Robots I*, pp. 233–242, Springer, 2012.
- [46] G. Chen, S. Zhang, and G. Li, "Multistable behaviors of compliant sarrus mechanisms," *Journal of Mechanisms and Robotics*, vol. 5, no. 2, p. 021005, 2013.
- [47] P. A. Halverson, L. L. Howell, B. D. Jensen, and S. P. Magleby, "Concepts for achieving multi-stability in compliant rolling-contact elements," in *ASME 2007 International Design Engineering Technical Conferences and Computers and Information in Engineering Conference*, pp. 67–73, American Society of Mechanical Engineers, 2007.
- [48] P. A. Halverson, L. L. Howell, and S. P. Magleby, "Tension-based multi-stable compliant rolling-contact elements," *Mechanism and Machine Theory*, vol. 45, no. 2, pp. 147–156, 2010.

- [49] M. Ohsaki and S. Nishiwaki, "Shape design of pin-jointed multistable compliant mechanisms using snapthrough behavior," *Structural and Multidisciplinary Optimization*, vol. 30, no. 4, pp. 327–334, 2005.
- [50] M. Hafez, M. D. Lichter, and S. Dubowsky, "Optimized binary modular reconfigurable robotic devices," *Mechatronics, IEEE/ASME Transactions on*, vol. 8, no. 1, pp. 18–25, 2003.
- [51] J. Oberhammer, M. Tang, A.-Q. Liu, and G. Stemme, "Mechanically tri-stable, true single-pole-double-throw (SPDT) switches," *Journal of Micromechanics and Microengineering*, vol. 16, no. 11, p. 2251, 2006.
- [52] R. Harne, M. Schoemaker, and K. Wang, "Multistable chain for ocean wave vibration energy harvesting," in *SPIE Smart Structures and Materials+ Nondestructive Evaluation and Health Monitoring*, pp. 90570B–90570B, International Society for Optics and Photonics, 2014.
- [53] G.-W. Kim and J. Kim, "Compliant bistable mechanism for low frequency vibration energy harvester inspired by auditory hair bundle structures," *Smart Materials and Structures*, vol. 22, no. 1, p. 014005, 2013.
- [54] B. Ando, S. Baglio, F. Maiorca, and C. Trigona, "Analysis of two dimensional, wide-band, bistable vibration energy harvester," *Sensors and Actuators A: Physical*, vol. 202, pp. 176–182, 2013.
- [55] M. S. Baker and L. L. Howell, "On-chip actuation of an in-plane compliant bistable micromechanism," *Microelectromechanical Systems, Journal of*, vol. 11, no. 5, pp. 566–573, 2002.
- [56] C. Nordquist, M. Baker, G. Kraus, D. A. Czaplewski, and G. Patrizi, "Poly-silicon based latching rf mems switch," *Microwave and Wireless Components Letters, IEEE*, vol. 19, pp. 380–382, June 2009.
- [57] A. Michael, C. Y. Kwok, K. Yu, and M. Mackenzie, "A novel bistable two-way actuated out-of-plane electrothermal microbridge," *Microelectromechanical Systems, Journal of*, vol. 17, no. 1, pp. 58–69, 2008.
- [58] B. Charlot, W. Sun, K. Yamashita, H. Fujita, and H. Toshiyoshi, "Bistable nanowire for micromechanical memory," *Journal of Micromechanics and Microengineering*, vol. 18, no. 4, p. 045005, 2008.
- [59] J. Herder, *Free Energy System: Theory. conception and design of statically balanced spring mechanisms*. PhD thesis, Delft University of Technology, 2001.
- [60] K. Hoetmer, J. L. Herder, and C. J. Kim, "A building block approach for the design of statically balanced compliant mechanisms," in *ASME 2009 International Design Engineering Technical Conferences and Computers and Information in Engineering Conference*, pp. 313–323, American Society of Mechanical Engineers, 2009.

- [61] K. Hoetmer, J. L. Herder, and C. J. Kim, "A building block approach for the design of statically balanced compliant mechanisms," in *ASME 2009 International Design Engineering Technical Conferences and Computers and Information in Engineering Conference*, pp. 313–323, American Society of Mechanical Engineers, 2009.
- [62] J. Lassooij, N. Tolou, G. Tortora, S. Caccavaro, A. Menciassi, and J. Herder, "A statically balanced and bi-stable compliant end effector combined with a laparoscopic 2dof robotic arm," *Mechanical Sciences*, 3 (2), 2012, 2012.
- [63] A. D. Roetter, C. P. Lusk, and R. Dubey, "Bistable compliant extension aid for a polycentric prosthetic knee," in *ASME 2009 International Design Engineering Technical Conferences and Computers and Information in Engineering Conference*, pp. 241–248, American Society of Mechanical Engineers, 2009.
- [64] A. D. Roetter, C. P. Lusk, and R. Dubey, "Bistable compliant extension aid for a polycentric prosthetic knee," in *ASME 2009 International Design Engineering Technical Conferences and Computers and Information in Engineering Conference*, pp. 241–248, American Society of Mechanical Engineers, 2009.
- [65] B. M. Wisse, W. D. van Dorsser, R. Barents, and J. Herder, "Energy-free adjustment of gravity equilibrators using the virtual spring concept," in *Rehabilitation Robotics, 2007. ICORR 2007. IEEE 10th International Conference on*, pp. 742–750, IEEE, 2007.
- [66] G. Chen and S. Zhang, "Fully-compliant statically-balanced mechanisms without pre-stressing assembly: concepts and case studies," *Mech. Sci*, vol. 2, no. 2, pp. 169–174, 2011.
- [67] M. Stranczl and J. Helfer, "Ancre flexible à force constante," Mar. 12 2014. EP Patent App. EP20,120,183,559.
- [68] S. Zhang and G. Chen, "Design of compliant bistable mechanism for rear trunk lid of cars," in *Intelligent Robotics and Applications*, pp. 291–299, Springer, 2011.
- [69] B. A. Fulcher, D. W. Shahan, M. R. Haberman, C. C. Seepersad, and P. S. Wilson, "Analytical and experimental investigation of buckled beams as negative stiffness elements for passive vibration and shock isolation systems," *Journal of Vibration and Acoustics*, vol. 136, no. 3, p. 031009, 2014.
- [70] J. Casals-Terre, A. Fargas-Marques, and A. M. Shkel, "Snap-action bistable micromechanisms actuated by nonlinear resonance," *Microelectromechanical Systems, Journal of*, vol. 17, no. 5, pp. 1082–1093, 2008.
- [71] R. Harne and K. Wang, "A review of the recent research on vibration energy harvesting via bistable systems," *Smart Materials and Structures*, vol. 22, no. 2, p. 023001, 2013.
- [72] D. Younesian and M.-R. Alam, "Multi-stable mechanisms for high-efficiency and broadband ocean wave energy harvesting," *Applied Energy*, vol. 197, pp. 292–302, 2017.

-
- [73] R. A. Receveur, C. R. Marxer, R. Woering, V. C. Larik, and N.-F. de Rooij, "Laterally moving bistable MEMS DC switch for biomedical applications," *Journal of Microelectromechanical Systems*, vol. 14, no. 5, pp. 1089–1098, 2005.
- [74] T. Pendleton and B. Jensen, "Development of a tristable compliant mechanism," in *Proceedings of 12TH IFToMM world congress A*, vol. 835, p. 2007, 2007.
- [75] L. L. Howell, S. P. Magleby, and B. M. Olsen, *Handbook of compliant mechanisms*. Wiley Online Library, 2013.
- [76] S. Henein, *Conception des guidages flexibles*. PPUR presses polytechniques, 2001.
- [77] P. Cazottes, A. Fernandes, J. Pouget, and M. Hafez, "Bistable buckled beam: Modeling of actuating force and experimental validations," *Journal of Mechanical Design*, vol. 131, pp. 101001–101001, Sept. 2009.
- [78] Y. Gerson, S. Krylov, and B. Ilic, "Electrothermal bistability tuning in a large displacement micro actuator," *Journal of Micromechanics and Microengineering*, vol. 20, no. 11, p. 112001, 2010.
- [79] H. Fang, S. Li, H. Ji, and K. Wang, "Dynamics of a bistable miura-origami structure," *Physical Review E*, vol. 95, no. 5, p. 052211, 2017.
- [80] S. Henein, *Conception des structures articules guidages flexibles de haute precision*. PhD thesis, Ecole polytechnique federale de Lausanne, 2000.
- [81] M. Zanaty, *Programmable multistable mechanisms*. PhD thesis, Ecole polytechnique federale de Lausanne, 2018.
- [82] G. Birkhoff and S. Mac Lane, *A survey of modern algebra*. Universities Press, 1966.
- [83] M. Bensimhoun, "Historical account and ultra-simple proofs of descartes's rule of signs, de gua, fourier, and budan's rule," *arXiv preprint arXiv:1309.6664*, 2016.
- [84] G. Hao, "Extended nonlinear analytical models of compliant parallelogram mechanisms: third-order models," *Transactions of the Canadian Society for Mechanical Engineering*, vol. 39, no. 1, pp. 71–83, 2015.
- [85] R. C. Merkle, "Two types of mechanical reversible logic," *Nanotechnology*, vol. 4, no. 2, p. 114, 1993.
- [86] M. Hafiz, L. Kosuru, and M. I. Younis, "Microelectromechanical reprogrammable logic device," *Nature communications*, vol. 7, p. 11137, 2016.
- [87] A. Rafsanjani, A. Akbarzadeh, and D. Pasini, "Snapping mechanical metamaterials under tension," *Advanced Materials*, vol. 27, no. 39, pp. 5931–5935, 2015.

Bibliography

- [88] M. Zanaty, A. Rogg, T. Fussinger, A. Lovera, C. Baur, Y. Bellouard, and S. Henein, "Safe puncture tool for retinal vein cannulation," in *Proceeding of Design of medical devices (DMD)*, 2017.
- [89] M. Zanaty, I. Vardi, and S. Henein, "Programmable multistable mechanisms: Synthesis and modeling," *Journal of Mechanical Design*, vol. 140, no. 4, p. 042301, 2018.
- [90] S. Henein, ed., *The art of flexure mechanism design*. EPFL press, 2017.
- [91] S. Awtar, A. H. Slocum, and E. Sevincer, "Characteristics of beam-based flexure modules," *Journal of Mechanical Design*, vol. 129, no. 6, pp. 625–639, 2007.
- [92] www.bohler-edelstahl.com/en/K390PM.php. [Accessed 2017-12-17].
- [93] www.leica-microsystems.com/products/stereo-scopes-microscopes/research/details/product/leica-m125-c. [Accessed 2017-12-17].
- [94] www.keyence.com/products/measure/laser-1/lk-g5000/models/lk-h082/index.jsp. [Accessed 2017-12-17].
- [95] www.kistler.com/en/product/type-9207/. [Accessed 2017-12-17].
- [96] www.ni.com/en-us/supprt/model.crio-9035.html. [Accessed 2017-12-17].
- [97] www.ni.com/en-us/support/model.ni-9220.html. [Accessed 2017-12-17].
- [98] www.kistler.com/en/products/components/signals-conditioning/charge-amplifier-module-ki-5171a-for-ni-compactrio. [Accessed 2017-12-17].
- [99] C.-A. Reymondin, G. Monnier, D. Jeanneret, U. Pellaratti, and E. technique de la Vallée de Joux (Le Sentier), *The theory of horology*. Swiss Federation of Technical Colleges: Watchmakers of Switzerland, Training and Educational Programm, 1999.
- [100] A. L. Rawlings, *The science of clocks and watches*. Pitman Pub. Corp., 1948.
- [101] P. Woodward, "My own right time-an exploration of clockwork design," *My Own Right Time-An Exploration of Clockwork Design*, by Philip Woodward, pp. 176. Foreword by Philip Woodward. Oxford University Press, Sep 1995. ISBN-10: 0198565224. ISBN-13: 9780198565222, p. 176, 1995.
- [102] C. McKay, *Big Ben, The Great Clock and the Bells at the Palace of Westminster*. Oxford University, 2010.
- [103] Arnfield, "An interially detached gravity escapement," *Horological Journal* 130(4), 1987.
- [104] S. vonGunten, "Ancre a pivotement flexible," *Bulletin de la Societe Suisse de Chronometrie* 69, 2012.
- [105] S. Krishnakumar and P. Tambe, "Entry complications in laparoscopic surgery," *Journal of gynecological endoscopy and surgery*, vol. 1, no. 1, p. 4, 2009.

-
- [106] J. Fanning, M. Shah, and B. Fenton, "Reduced-force closed trocar entry technique: analysis of trocar insertion force using a mechanical force gauge," *JSLs: Journal of the Society of Laparoendoscopic Surgeons*, vol. 15, no. 1, p. 59, 2011.
- [107] A. Gijbels, E. B. Vander Poorten, P. Stalmans, and D. Reynaerts, "Development and experimental validation of a force sensing needle for robotically assisted retinal vein cannulations," in *Robotics and Automation (ICRA), 2015 IEEE International Conference on*, pp. 2270–2276, IEEE, 2015.
- [108] B. Gonenc, N. Tran, P. Gehlbach, R. H. Taylor, and I. Iordachita, "Robot-assisted retinal vein cannulation with force-based puncture detection: Micron vs. the steady-hand eye robot," in *Engineering in Medicine and Biology Society (EMBC), 2016 IEEE 38th Annual International Conference of the*, pp. 5107–5111, IEEE, 2016.
- [109] H. Yu, J.-H. Shen, K. M. Joos, and N. Simaan, "Design, calibration and preliminary testing of a robotic telemanipulator for oct guided retinal surgery," in *Robotics and Automation (ICRA), 2013 IEEE International Conference on*, pp. 225–231, IEEE, 2013.
- [110] N. Begg, "A novel tip-retraction mechanism for puncture devices," *Journal of Mechanical Design*, vol. 136, no. 10, p. 105002, 2014.
- [111] P. M. Loschak, K. Xiao, H. Pei, S. B. Kesner, A. J. Thomas, and C. J. Walsh, "Assured safety drill with bi-stable bit retraction mechanism," in *ASME 2013 International Design Engineering Technical Conferences and Computers and Information in Engineering Conference*, pp. V06AT07A001–V06AT07A001, American Society of Mechanical Engineers, 2013.
- [112] R. E. Wyrick, "Medicine injection devices and methods," Nov. 20 2007. US Patent 7,297,136.
- [113] S. Rogers, R. L. McIntosh, N. Cheung, L. Lim, J. J. Wang, P. Mitchell, J. W. Kowalski, H. Nguyen, and T. Y. Wong, "The prevalence of retinal vein occlusion: pooled data from population studies from the united states, europe, asia, and australia," *Ophthalmology*, vol. 117, no. 2, pp. 313–319, 2010.
- [114] T. Y. Wong and I. U. Scott, "Retinal-vein occlusion," *New England Journal of Medicine*, vol. 363, no. 22, pp. 2135–2144, 2010.
- [115] T. Asami, H. Kaneko, K. Miyake, I. Ota, G. Miyake, S. Kato, S. Yasuda, T. Iwase, Y. Ito, and H. Terasaki, "An endovascular cannulation needle with an internal wire for the fragmentation of thrombi in retinal vein occlusion," *Translational vision science & technology*, vol. 5, no. 5, pp. 9–9, 2016.
- [116] X. He, V. Van Geirt, P. Gehlbach, R. Taylor, and I. Iordachita, "Iris: Integrated robotic intraocular snake," in *Robotics and Automation (ICRA), 2015 IEEE International Conference on*, pp. 1764–1769, IEEE, 2015.

Bibliography

- [117] N. Dehon, "Escapement mechanism," Nov. 6 2012. US Patent 8,303,167.
- [118] A. Steimle, "3d micro-printing: A new era for med-tech applications," *Laser Technik Journal*, vol. 15, no. 1, pp. 32–34, 2018.
- [119] Y. Bellouard, A. Said, M. Dugan, and P. Bado, "Fabrication of high-aspect ratio, micro-fluidic channels and tunnels using femtosecond laser pulses and chemical etching," *Optics express*, vol. 12, no. 10, pp. 2120–2129, 2004.
- [120] www.femtoprint.ch/. [Online; accessed 02-April-2018].

Mohamed ZANATY

PERSONAL INFORMATION

Birth Date October 2, 1987

Work Rue de Maladiere 71b

Address 2000 Neuchatel, Switzerland

Phone (+41) 79 171 19 95

E-mail zanatymg@gmail.com

EDUCATION

Ph.D. Microsystems and Microelectronics

2014 - 2018

Ecole Polytechnique Federale de Lausanne (EPFL), Switzerland

Thesis title: Programmable Multistable Mechanisms: Design, Modeling, Characterization and Applications.

Thesis venue: Instant-Lab, Microcity, Neuchatel, Switzerland.

Supervisors: Professor Simon Henein and Dr. Ilan Vardi.

M.Sc. Microsystem Engineering

2011 - 2013

Assiut University, Egypt

Thesis title: Design, Modeling and Characterization of MEM Resonators for Biosensing.

Thesis venue: IMEC, Leuven, Belgium.

Supervisors: Professor Ann Witvrouw and Dr. Harrie Tilmans.

B.Sc. Electrical Engineering

2004 - 2009

Assiut University, Egypt

Thesis title: Design and Implementation of Smart Cell Phone Jammers using Universal Software Radio Peripheral (USRp).

Supervisors: Professor Mohammad Abbas.

EMPLOYMENT HISTORY & RESPONSIBILITIES

Doctoral Assistant

2014 - 2018

EPFL, Neuchatel, Switzerland

- Conceptual design, modeling, manufacturing and experimental characterization of programmable compliant multistable mechanisms and their medical and horological applications.
- Assist in preparing exercises for undergraduate courses - Mechanical design - Compliant structure design.
- Follow-up of undergraduate students on mechanical engineering projects.
- Assist in organizing seminars and lectures on compliant structures.

Head of Engineering

2013-2018

LuxNour Technologies, Portland, Oregon, USA

- Conceptual design, modeling and simulation of pick and place tools to enable high volume manufacturing of micro-LED displays.

Research Engineer

2013 - 2014

IMTEK, Freiburg, Germany

- Modeling, design, microfabrication and characterization of magnetic meta-material for enhancing signal to noise ratio of magnetic resonance imaging (MRI).
- Optimization of the inkjet printing of micro-coils for MRI.
- Follow up of graduate students on micromechanical projects.

Research Assistant

2011 - 2013

IMEC, Leuven, Belgium

- Design, modeling, micro fabrication and characterization of meta-material based bulk acoustic wave resonators for bio-molecular sensing applications.
- Analytical modeling of the impact of nonlinear Casimir and Van der Waals forces on the dynamic behavior of nano-cantilevers.
- Guidance of undergraduate trainees.
- Organization of workshops on FEM simulations of electromechanical resonators.

Research Assistant

2010 - 2011

Assiut University, Assiut, Egypt

- VHDL, python coding and PCB design of optical transceivers.
- ASIC design of analog to digital converters.
- Teaching assistant for undergraduate electrical engineering students.
- Assist in the preparation of undergraduate curriculum for the mechatronics department.
- Follow up of bachelor graduation projects.

Technician

06 - 10/2008

Hellenic Air Force, Volos, Greece

- Troubleshooting and on ground maintenance of radio beacons for Huey UH-1H and Apache helicopters.

TEACHING

Mechanism Design I/II

2015-6-7

Ecole Polytechnique Federale de Lausanne, Switzerland - Microengineering section - Bachelor semester 3 / 4

Mechanical Design I/II

2014-5

Ecole Polytechnique Federale de Lausanne, Switzerland - Microengineering and mechanical sections - Bachelor semesters 1/2

Microsystem Design I/ II

2013-4

University of Freiburg, Germany - Microengineering section - Master semesters 2/3

Semiconductor Devices I/II

2009-10

Assiut University, Egypt - Electrical engineering section - Bachelor semesters 1/2

Integrated Circuit Design

2009-10

Assiut University, Egypt - Electrical engineering section - Bachelor semesters 4/5

AWARDS, FELLOWSHIPS & APPROVED RESEARCH FUNDS

- Recipient of the SNSF early postdoc mobility fellowship, November 2018.
- One of the eight finalists for Science slam at the Swiss medtech day, 2018.
- Recipient of the Swiss Commission of Technology and Innovation (CTI) fund for the development of retinal vein cannulation needles, 2015.
- Recipient of the Intel corporation - Center of Excellence in Nano-Manufacturing Applications (CENA) fellowship, 2011.
- Orascom research grant awarded to the top three electrical engineering bachelor graduates, Egypt, 2010.
- IEEE finalist for the best undergraduate project in the Middle East and North Africa region, 2010.
- Academic excellence award, Assiut University, 2004-2009.
- Graduated with distinction and honors (first of 400 students graduating class), electrical engineering department, Assiut University, 2009.

TECHNICAL & LANGUAGE SKILLS

FEM

COMSOL, ANSYS

SOFTWARE

MATLAB, ~~W~~_E^T_EX, PYTHON, LABVIEW

MANUFACTURING

Mask design, Photo-lithography, Etching, Wire-bonding.

3D printing, PCBs, CNC, Laser cutting, Conventional machining.

LANGUAGES

English: Fluent, French: B2 Level, German: B1 Level

ACADEMIC MEMBERSHIPS & ACTIVITIES

- Student Member of the American Society of Mechanical Engineers (ASME).
- Student Member of the International Electrical and Electronic Engineers (IEEE).
- Technical Reviewer of the ASME Journal of Mechanical Design
- Technical Reviewer of the ASME International Design Engineering and Technology Conferences.
- Associate Editor of VLSI Egypt Magazine, 2012-2014.

PUBLICATIONS

• Publications in Peer-reviewed Scientific Journals

1. **Zanaty, M.**, Vardi, I. and Henein, S., 2018. Programmable multistable mechanisms: Synthesis and modeling. ASME Journal of Mechanical Design, 140(4), p.042301. - Selected as a feature article.
2. **Zanaty, M.** and Henein, S., 2018. Experimental Characterization of a T-shaped Programmable Multistable Mechanism. ASME Journal of Mechanical Design, 140(9), p.092301.

• Peer-reviewed Conference Proceedings

3. **Zanaty, M.**, and Henein, S., 2018. Programmable Constant-Force Multistable Mechanisms. ASME International Design Engineering Technical Conferences and Computers and Information in Engineering Conference, Quebec, Canada, August 26-29.
4. **Zanaty, M.**, Rogg, A., Fussinger, T., Lovera, A., Baur, C., Bellouard, Y. and Henein, S., 2017. Safe puncture tool for retinal vein cannulation. Design of Medical Devices (DMD), Eindhoven, the Netherlands, Nov. 14-15.
5. Kahrobaiyan, M.H., **Zanaty, M.** and Henein, S., 2017. An Analytical Model for Beam Flexure Modules Based on the Timoshenko Beam Theory. ASME International Design Engineering Technical Conferences and Computers and Information in Engineering Conference, Cleveland, OH, USA, August 6-9.
6. Rottenberg, X., Jansen, R., Cherman, V., Witvrouw, A., Tilmans, H.A.C., **Zanaty, M.**, Khaled, A. and Abbas, M., 2013, November. Meta-materials approach to sensitivity enhancement of MEMS BAW resonant sensors. In IEEE SENSORS, Baltimore, MD, USA, Nov. 3 - 6.
7. **Zanaty, M.**, Jansen, R., Rochus, V., Abbas, M., Witvrouw, A., Tilmans, H.A.C. and Rottenberg, X., 2013. Influence of nonlinear intermolecular forces on the harmonic behavior of NEM resonators. In IEEE Thermal, Mechanical and Multi-Physics Simulation

and Experiments in Microelectronics and Microsystems (EuroSimE), Wroclaw, Poland, April 14-17.

8. **Zanaty, M.**, Jansen, R., Rochus, V., Abbas, M., Witvrouw, A., Tilmans, H.A.C. and Rottenberg, X., 2012. Influence of the nonlinearity introduced by the van der waals force on the behaviour of nem resonators. In 23rd Micromechanics and Microsystems Europe Conference, Illmenau, Germany, Sept. 5-7.

- **Patents and Licenses**

9. **Zanaty, M.**, Henein, S., 2015, Systeme Multistable Programmable, Patent Number EP3266737A1.

10. **Zanaty, M.**, Baur, C., Henein, S., 2016, Device for Controlled Puncturing of Bodily Vein, Patent Number EP16180443.0.

11. **Zanaty, M.**, Vardi, I., Henein, S., 2016, Constant Force Snap Escapement, Patent Pending.

12. Kahrobayian, M., **Zanaty, M.**, Baur, C., Henein, S., 2018, Load Cell with Tunable Stiffness Dedicated to Force Measurement in the Nano-Newton Range, Patent Pending.

13. **Zanaty, M.**, Hussein, M., 2018, Electromagnetic Stamp for Micro-LED Manufacturing, Patent Pending.

- **Contributions to International Conferences – Posters**

14. **Zanaty, M.**, and Henein, S., 2016, Numerical Simulation of Multistable Mechanisms, COMSOL Day, Zurich, Switzerland.

15. **Zanaty, M.**, While, P. and Korvink, J. 2014, Magnetic Metamaterials for Magnetic Resonance Imaging, European Metamaterial Congress, Rome, Italy.

- **Invited Talks**

16. **Zanaty, M.**, 2016, Programmable Multistable Mechanisms and their Applications, ICube, University of Strasbourg, France.

17. **Zanaty, M.**, 2016, Programmable Multistable Mechanisms and their Applications, American University in Cairo, Egypt.

18. **Zanaty, M.**, 2013, Metamaterial Based Bulk Acoustic Wave Resonators, Buskerud and Vestfold University College, Norway.

19. **Zanaty, M.**, 2012, Modeling of nano-forces for NEM cantilevers, King AbdulAllah City of Science and Technology (KACST), Saudi Arabia.

- **Submitted but not yet Accepted**

20. **Zanaty, M.**, Rogg, A., Fussinger, T., Lovera A., Vardi, I., Baur, C., Wolfensberger, T. and Henein, S., Programmable Multistable Mechanisms for Safe Surgical Puncturing. Submitted to the ASME Journal of Medical Devices.

21. **Zanaty, M.**, Rubbert, L. and Henein, S., Programmable Master Slave Multistable Mechanisms. Submitted to the ASME Journal of Mechanical Design.

- **Media Coverage**

22. From an inert material to a highly-performant micro 3D printed medical device.
International Commercial Micro Manufacturing Magazine, June 2018.